論文 / 著書情報
Article / Book Information

題目(和文)	液体金属MHD 発電機の性能と乱流流れに関する数値的研究
Title(English)	Numerical Study of Performance and Turbulent Flows in a Liquid Metal MHD Generator
著者(和文)	胡蓮成
Author(English)	Liancheng Hu
出典(和文)	学位:博士（工学）, 学位授与機関:東京工業大学, 報告番号:甲第9851号, 授与年月日:2015年3月26日, 学位の種別:課程博士, 審査員:奥野　喜裕,岡村　哲至,末包　哲也,長崎　孝夫,肖　鋒,小林　宏充
Citation(English)	Degree:, Conferring organization: Tokyo Institute of Technology, Report number:甲第9851号, Conferred date:2015/3/26, Degree Type:Course doctor, Examiner:,,,,,
学位種別(和文)	博士論文
Type(English)	Doctoral Thesis

Numerical Study of Performance and Turbulent Flows in a Liquid Metal MHD Generator

Liancheng HU

Supervisor: Prof. Yoshihiro OKUNO

Department of Energy Sciences

Tokyo Institute of Technology

February, 2015

Table of Contents

List of Figures

List of Tables

Nomenclature

Abbreviations

CFD	computational fluid dynamics
CSM	coherent structure Smagorinsky model
DNS	direct numerical simulation
LES	large eddy simulation
LMMHD	liquid metal magnetohydrodynamic
MHD	magnetohydrodynamic
OWC	oscillating water column
Q2D	quasi-two-dimensional
RANS	Reynolds averaged Navier-Stokes
SM	Smagorinsky model

Symbols

$\vec{A}$	vector potential
$\vec{B}$	magnetic flux density vector
B_z	externally applied magnetic flux density (in the z direction)
D	characteristic length (equals to duct width L in this thesis)
$\vec{E}$	electric field vector
E	magnitude of the velocity gradient tensor
$\vec{F}$	external force vector
F^*	dimensionless external force
Ha	Hartmann number
$\vec{j}$	current density vector
j^*	dimensionless current density
K	load factor
L	duct width
L_x	length of duct
L_y, L_z	width, height of duct
N	interaction parameter
P	pressure
P^*	dimensionless pressure
Q	second invariant of the velocity gradient tensor
Re	Reynolds number
Re_τ	friction Reynolds number
U_b	the characteristic velocity (bulk velocity)
$\vec{u}$	flow velocity vector
u^*	dimensionless flow velocity
u_τ	friction velocity, also called shear velocity

Greek symbols

ϕ, φ	electric potential
μ	dynamic viscosity of the fluid
μ_0	permeability constant
ν	kinematic viscosity
ν_e	turbulent eddy viscosity
ν_m	molecular viscosity
ρ	mass density
σ	electrical conductivity
σ_e	electrical conductivity of electrode
σ_f	electrical conductivity of fluid
σ_R	electrical conductivity of load resistance
τ	subgrid-scale stress tensor
τ_ω	wall shear stress
Δx	space grid in x direction
Δy	space grid in y direction
Δz	space grid in z direction

Chapter 1 - **Introduction**

Natural resources such as coal, crude oil, and natural gas take thousands of years to naturally form, but being consumed every second by human beings. These resources are on the verge of exhausted. Not to mention the continual use of fossil fuels at the current rate is believed to increase global warming and cause more severe climate change [1][2]. Humanity need to shift its reliance on fossil fuel to other sources of energy.

The needs induce a change in the renewable energies scenario and raised the interest in energy production from the waves [3]. In this chapter, a brief review of wave energy utilization and the basic concepts of liquid metal magnetohydrodynamic (LMMHD) technologies are outlined. Subsequently, motivations and objectives of this thesis are described. At the end, the whole thesis organization is presented.

1.1 Wave energy utilization

1.1.1 The Wave Energy Resource

The ocean probably stores enough energy to meet total worldwide demand for electricity and even many times over [4]. As a branch of ocean engineering, sea wave energy is being increasingly regarded as a major and promising resource in several countries [5] ~ [8]. The worldwide wave energy resource has been estimated to be greater than 2 TW, which is the same order of magnitude as the world's electricity consumption (year around 2000) [6].

The main mechanism of common wave is not complex. As wind rushes across water surface, it generates waves. In open water, waves are generated whenever the wind speed is greater than about 0.5m/s [9][10]. Generally, wind speed and the duration time determine the wave scale, which consequently holds kinetic and potential energy.

The features of wave energy resource are distinct. Not only the energy resource is titanic, but also it is more dependable than most renewable energy resources. Wave power is available up to 90 % of the time, while solar and wind availabilities tend to be available just 20 ~ 30 % of the time [11]. “Waves have long memory and will keep going in the same direction for days after the wind stopped blowing, until they bump into something” [10]. Additionally, long period (7 ~ 10 s), large amplitude (2 ~ 3 m) waves have energy fluxes commonly averaging between 20 and 70 kW per meter width, which is a high energy density among renewable energy sources [7].

On the other hand, the variability of wave power, “from wave to wave and from month to month with sea states” [3], induces difficulties for utilization. Besides, extreme weather conditions, such as hurricanes and tsunami, should not be ignored.

1.1.2 Various Approaches

The concept of converting wave energy into usable energy has inspired numerous inventors. It is claimed that more than one thousand patents had been registered by 1980 and the number is still markedly increasing up until now [8]. In this thesis, only lists three typical systems (classify according to working principle) for instance.

Oscillating water column (OWC) type

The OWC system comprises a partly submerged concrete structure (capture chamber) and a turbine. The oscillating motion of the internal free surface produced by the waves makes the air to flow through the turbine which drives an electrical generator.

Various OWC type systems were built and examined around the world [12] ~ [14]. Figure 1.1 shows the Land Installed Marine Powered Energy Transformer (LIMPET-500) plant (total water surface area of 169 m^2) of UK [14]. It is the achievement of a ten-year research

project where a demonstration plant was built capable of generating 75 kW (in 1991) of power (in 2001 generating 500 kW) to supply to the grid on the island of Islay.

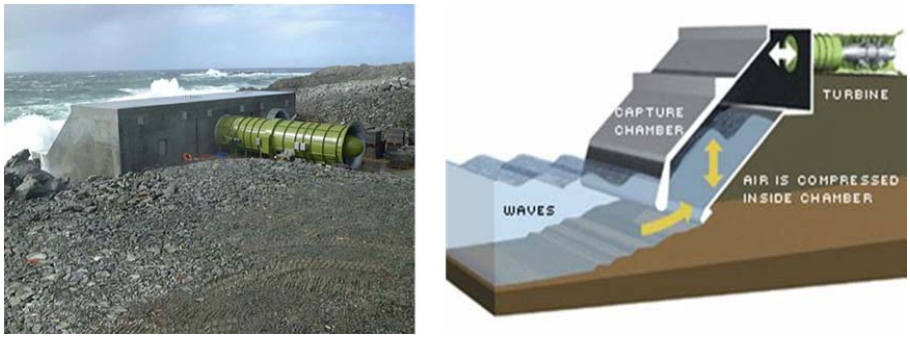

Fig. 1.1 An oscillating water column system: Land Installed Marine Powered Energy Transformer (LIMPET-500) on the island of Islay (courtesy of Wavegen and Queen's University Belfast [14]).

Overtopping type

Through capturing the overtopping water into a reservoir, the potential energy is stored at a level higher than the average free-surface surrounding sea. Then the stored potential energy can be converted into electricity by flowing through the conventional low-head hydraulic turbines.

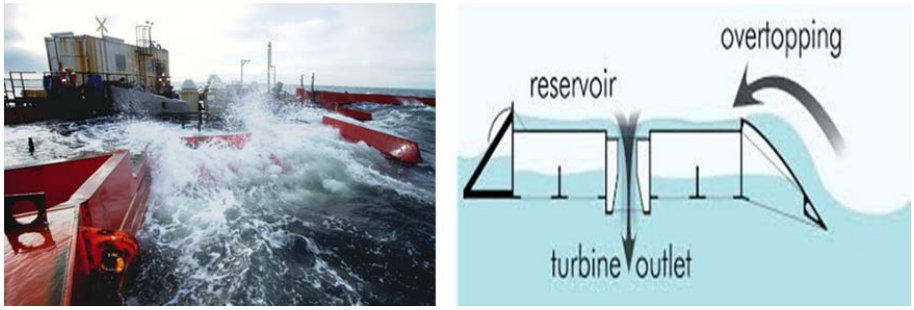

Fig. 1.2 An overtopping type system: Wave Dragon in Nissum Bredning, Denmark (courtesy of Wave Dragon ApS, Denmark [15]).

Figure 1.2 illustrates the overtopping type system of Wave Dragon in Nissum Bredning, Denmark, which conducts energy conversion based on the principle above. It is a 57 × 27 m^2

wide, 237 tons (including ballast) full-sized prototype, which successfully connected to national grid (4~10 MW) in May 2003 and has been tested for several years [15].

Moving body type

Moving body type sometimes classified as third generation systems, which is suitable for offshore devices, but much more complex compared with OWC and overtopping type [3]. It includes either floating or fully submerged oscillating bodies, mostly on the stage of research or coming close to full-scale demonstration.

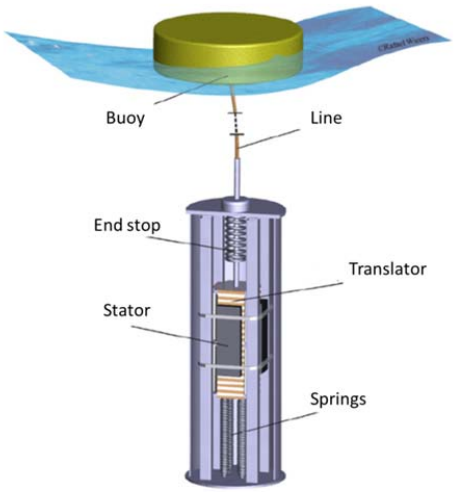

Fig. 1.3 A moving body type system: Swedish heaving buoy with linear electrical generator (courtesy of Uppsala University [16]).

A concept of taut-moored buoy was researched at Uppsala University, Sweden. The prototype uses a linear electrical generator placed on the ocean floor, with a line from the top of the generator connected to a buoy float at the ocean surface, as shown in Fig. 1.3 [16]. Springs attached to the translator of the generator store energy during half a wave cycle and simultaneously restore force in another half wave. Sea tests results of a 3 m diameter cylindrical buoy are also reported [16].

In this moving body type, Y. Peng *et al.* examined the wave energy conversion with an LMMHD power generator. A performance analysis for an LMMHD generator (electrode length: 100 cm; cross section: 30 cm × 5 cm) suggests that the maximum output power of 3.35 kW should be obtained when wave amplitude is 1.0 m with a period of 6 s under a magnetic flux density of 0.5 T [17].

1.1.3 A Comparison on Electrical Equipment

Whatever the system type or the working principle is, the final part is an electrical equipment to supply electricity to a grid. In this section, the main features of conventional rotating generator and direct drive linear generator (limited to LMMHD in this thesis) are compared. Note that the comparison here is mainly concerned with technological aspects of energy conversion. Issues like policies, economics are left aside.

For rotating generators, the coupling of the irregular, slow motion (frequency around 0.1 Hz) of a wave to high-speed rotary requires typically 500 times greater frequency [18]. As a result, mechanical interface, which brings non-negligible losses, are required [8]. Additionally, as mentioned above, wave motions are chaotic and random that consists of wide frequency and magnitude [19]. Because of these irregularities, it is difficult to obtain maximum efficiency of a rotating generator over the entire range of excitation frequencies energy. It was reported that the maximum total electrical efficiency of the Oscillating Water Column (OWC) system "Mighty Whale" is 15% [20]. On the other hand, mechanical machines such as air or hydraulic turbines are relatively mature technology that had been devised and developed for a long time, which can shorten development time and are still the competitive approaches.

Linear generators have the advantage of avoiding a mechanical interface and eliminating the non-negligible losses that take place in the mechanical machines. Besides, the reciprocating

motion of piston, which drives the liquid metal to correspondingly move in the generator, matches the motion of the actual wave oscillation, at speeds two orders of magnitude lower than the need of rotary generators. An analytical report asserted that the conversion efficiency of an LMMHD system may reach more than 60% [17]. In light of the discussion above, the electrical efficiency of wave energy based LMMHD systems should be much higher than the traditional rotating generators in general. However, as is different from the traditional two-phase flow (a thermodynamic fluid such as gas or stream acts as the working medium that can expand with temperature) LMMHD power generation systems, wave motion based LMMHD power generation systems are still at the prototype development stage and the real sea-test are still under examined [21] ~ [23].

1.2 Liquid Metal Magnetohydrodynamic Technologies

1.2.1 Concepts of LMMHD Generators

Since the systematic experimental study of an MHD flow had been performed with mercury and a relevant theory developed by J. Hartmann [24][25] even a short time before the breakout of World War II, the research on Liquid Metal MHD has a history as long as the plasma MHD [26].

The basic principles of MHD energy conversion are the same regardless of what the working fluids are. The major element of an LMMHD energy conversion system is also the MHD channel shown in Fig. 1.4 [27]. It consists of a duct which allows the working fluids flow through driven by an applied external force, an arrangement of coils which produce a magnetic field across the duct, and a pair of electrodes on each side to carry off the current. When an electrically conductive working fluid flows through the duct, electric power can be extracted in

the presence of a perpendicular magnetic field. The liquid metal is referred to as the working fluid or electromagnetic fluid.

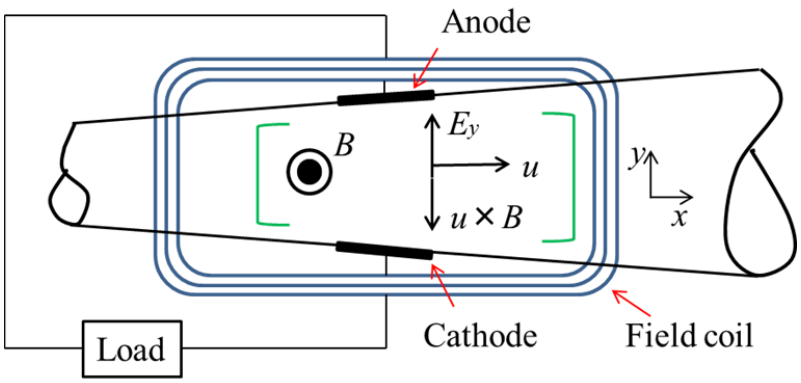

Fig. 1.4 Schematic diagram of a dc magnetohydrodynamic generator.

To introduce the basic concepts by formulas, a simplified mathematical description is given as follow. If the liquid metal has a velocity u, and an electrical conductivity σ, then the current density induced by the motion through a magnetic density flux of B is

$$j = \sigma(uB - E_y), \tag{1.1}$$

where E_y is the internal electric field due to the load. After defining a load factor K under customary:

$$K = \frac{E_y}{uB}, \tag{1.2}$$

the output power P_o delivered to the load, per unit volume of the generator, is

$$P_o = jE_y = K(1-K)\sigma u^2 B^2. \tag{1.3}$$

On the other hand, the Lorentz force against the motion is given by

$$F = jB = (1-K)\sigma uB^2, \tag{1.4}$$

which does the input push work as

$$P_i = Fu = (1-K)\sigma u^2 B^2, \tag{1.5}$$

then the ratio of the output power to the input work is the electrical efficiency,

$$\eta_e = \frac{P_o}{P_i} = K. \tag{1.6}$$

1.2.2 A Review of Related Works

In general, liquid metal MHD studies were conducted among theoretical, experimental and numerical works over the past decades. The major contents can be divided into two main areas, the electrical performance and the MHD flow phenomena. The former one refers to researches on LMMHD power generators or accelerators. The latter one is to understand the MHD turbulent flows in the fields of metal casting, fusion, crystal growth of silicon, as well as LMMHD power generators and accelerators. This thesis only describes a few of them as examples to show the substantial development on LMMHD since 1960s.

Theoretical and experimental studies

Sutton and Carlson theoretically inspected the end effects for small magnetic Reynolds number and small magnetic interaction parameter in an MHD channel [28]. It is found that the fluid velocity is retarded at the center of the channel while accelerated at the walls. The end electrical and pressure losses are calculated successively for MHD generators. For an MHD generator, the maximum electrical efficiency is limited to 29% owing to the losses, while an ideal efficiency of 90% were expected by increasing the generator length, extending the magnetic field, and inserting an insulating vane of zero thickness placed in the center of the channel [29].

Then, Elliott claimed that the theoretical efficiency of LMMHD generators could reach 58%, in considering fluid friction, boundary-layer shunting, ohmic heating and end effects, and

the theoretical ultimate efficiency could range from 60 to 70%. The corresponding experiments tested with liquid metal NaK were conducted at inlet velocities up to 300 feet per second. The maximum output power was about 10 kW and the efficiency reached 48% [30].

Almost simultaneously, Lykoudis and Brouillette presented their results on the study of fully established turbulent channel flow of mercury in the presence of a transverse and uniform magnetic field. A semi-empirical theoretical analysis and related experiments were examined [31][32]. The speculation that a straightforward generalization of Prandtl's mixing length concept is sufficient in predicting skin friction coefficients and velocity profiles were verified by static pressure and traversing probe total head measurements along the channel.

A couple of years later, Reed and Lykoudis experimentally examined the effect of a transverse magnetic field on shear turbulence. An aspect ratio (of the channel width to the channel height) of 5.8 of the channel with electrically insulated walls was investigated by using mercury as the working fluid. The presence of M-shaped velocity profiles in the direction perpendicular to the magnetic field was observed [33].

Because of the opacity and corrosiveness of liquid metals, velocity measurements are notoriously difficult in experiments, especially for the observation of various scales of turbulence. The research below gives certain insight into it.

Andreev *et al.* conducted an experimental study of a liquid metal flow in a rectangular channel under the influence of an un-uniform magnetic field [34]. The cross-sectional view of the experimental apparatus and the test probes are shown in Fig. 1.5. Based on the electric potential measurements method, they identified the local velocity on three distinct flow regions. Namely (a) a turbulence suppression region, (b) a vertical region, and (c) a wall jet region. The results are reliable for the mean flow and for large scale (larger than the diameter of probes)

velocity fluctuations while the accuracy needs to be improved for small scale eddies comparable to the length scale of the probes.

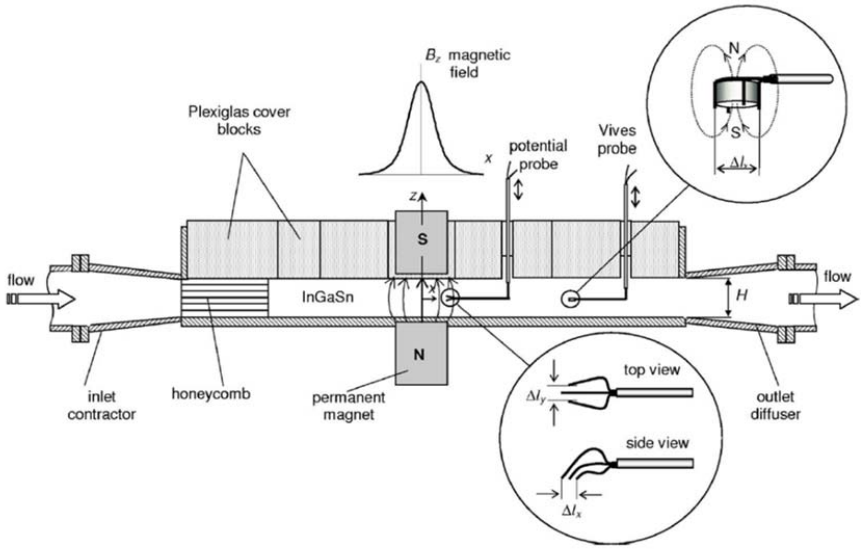

Fig. 1.5 Cross-sectional view of an experimental apparatus for measuring liquid metal MHD flows conducted by Andreev. (Channel length: 500 mm, height: H=20 mm, and width: 100 mm. The maximum of the magnetic flux density is $B_0 = 0.504$ T. Insets show the probes. [34])

Numerical studies

On the other hand, judging by the amount of papers published or presented at conferences, observing phenomena by numerical methods becomes increasingly popular recently. Instead of building a complete experimental platform or solving all equations analytically in the entire problem domain, numerical simulation is able to split problem into smaller pieces (discretization) and solve each with methods like “Finite difference” or “Finite Volumes”, and eventually merge the partial results into the solution for the whole problem. More importantly, along with the development of computer and software, numerical simulation has the advantage of observing the opaque liquid metal in a simple and safe way. Here, Fig. 1.6 shows the

instantaneous velocity of an MHD ducts flow with conducting walls as an example to illustrate the visualization of results by numerical methods [35].

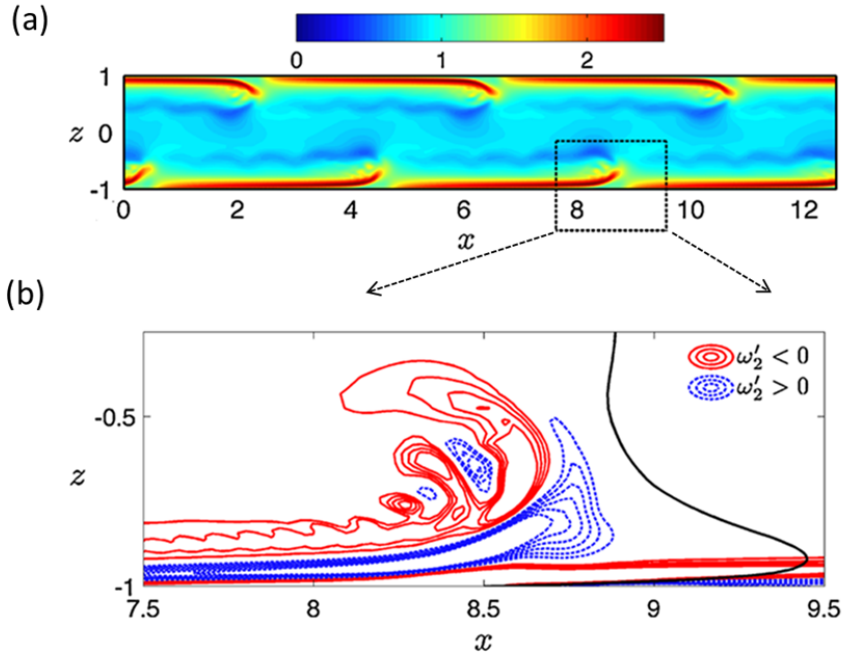

Fig. 1.6 Instantaneous contours of axial component of (a) the total axial velocity and (b) the velocity limited to the dashed box (courtesy of Maxime Kinet and Bernard Knaepen [35]).

A number of studies, including Reynolds Averaged Navier-Stokes (RANS) models [36] ~ [38], Large Eddy Simulation (LES) models [39] ~ [43], and Direct Numerical Simulation (DNS) [44] ~ [47], have been performed to address MHD turbulent flows in numerical calculation. Generally, an "exact" numerical approach would be the use of DNS, where resolve all scales of turbulences, assuring the very detailed observation on the flows. However, the computational cost restricts the problems to a limited scale. On the other hand, the RANS methods use various turbulence modeling assumptions to simulate problems. It does not require large CPU resources but to build appropriate models is complicate. Relatively, LES is an intermediate approach. After

a filtering operation applied to the Navier-Stokes equations, it explicitly resolves the dynamics of the unsteady large scales of turbulence while modeling the small scale ones.

The observations are conducted around various external conditions, channel or duct, insulated or perfect electrically conducting walls, uniform or non-uniform magnetic fields, to name a few. For instance, in MHD duct flows covered with insulated walls, H. Kobayashi discovered that turbulence are curbed asynchronously among different layers, from the Lorentz force acts against the direction of the flow [42]. Quasi-two-dimensional (Q2D) structures are observed along the orientation of the magnetic field in MHD turbulent duct flows surrounded with the electrically conducting walls [35]. And recently, the influence of the non-uniform magnetic field on turbulent flows in a liquid metal MHD power generator at its optimal load resistance was examined [48].

Applications

Many concepts or approaches on applications of LMMHD have been proposed. Here only lists a few which are close or associated to this thesis. Maeda *et al.* investigated the free piston internal combustion engine with an LMMHD generator by two-dimensional numerical simulation [49]. Figure 1.7 shows the schematic diagram of the engine system.

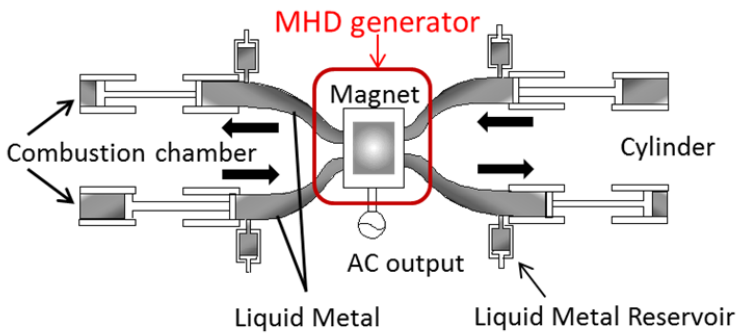

Fig. 1.7 Configuration of a liquid metal MHD engine [50].

The LMMHD generator comprises double-duct which can suppress the influence of induced magnetic field. The length of the piston stroke is alterable by changing the amount of the liquid metal through four reservoirs. The research aimed to change the electrical power output according to need and to adapt to a partial load operation of distributed power supply. The results show the electrical efficiency in MHD channel can reach 90% using low melting point metal. Subsequently, Satake *et al.* experimentally demonstrated the system and obtained a maximum output of 10.3 W under a magnetic flux density of 1.0 T [51].

K. Yamada *et al.* investigated the effect of the electrode width on the performance of a rectangular duct through both two-dimensional and three-dimensional numerical simulations with the induced magnetic field, taking account of the current flow in the electrodes [52][53]. An optimal electrode length and current lead position were revealed. The highest performance was found to be obtained when the width of the electrode along the direction of the magnetic field is equal to that of the generator. These results of the LMMHD generator are referred in this thesis (refer to Chapter 3).

In regard to utilization of wave energy sources, Y. Peng *et al.* examine the LMMHD systems in a couple of aspects including effects of liquid metal characteristics and end effect of LMMHD generator [17], [54] ~ [57], one of which has been referred at Section 1.1.2.

1.2.3 Parameters for Performance Evaluation

Typical parameters to predict flow situations and/or to assess the performance and of a liquid metal MHD generator are defined as follows.

Reynolds number:

$$\mathrm{Re} = \frac{\rho U_b L}{\mu} = \frac{U_b L}{\upsilon}, \tag{1.7}$$

is a dimensionless quantity that is used to help predict similar flow patterns in different fluid flow situations. ρ and μ are the mass density and dynamic viscosity of liquid metal. U_b is the bulk (mean) velocity. The characteristic length L equals to the width of the duct. It is defined as the ratio of inertial forces to viscous forces and consequently quantifies the relative importance of these two types of forces for given flow conditions.

Reynolds numbers are frequently used to characterize the fluid flow whether a laminar or turbulent flow (with the critical value of 2300 for pipes/ducts usually). The friction Reynolds number is to use the friction velocity (u_τ) and half of the duct width (L/2) to define the wall-bounded turbulent flows especially, shown as

$$\mathrm{Re}_\tau = \frac{\rho u_\tau L/2}{\mu} = \frac{u_\tau L}{2\upsilon}, \tag{1.8}$$

Magnetic Reynolds number:

$$\mathrm{Re}_m = \sigma_f \mu_0 U_b L, \tag{1.9}$$

is a dimensionless number which gives an estimate of the effects of magnetic advection to magnetic diffusion, where μ_0 is the permeability constant and σ_f is the electrical conductivity of liquid metal. Another useful interpretation is Re_m reflects the extent to which the working fluid motion can modify or deflect the magnetic field. In general, Re_m is large compared with unity in

fusion research and astrophysics, but equal to or less than unity in MHD energy conversion [27]. In this thesis, the maximum magnetic Reynolds number of 1.55×10^{-2} (for NaK with U_b = 0.06 m/s) is less than unity.

Interaction parameter:

$$N = \frac{\sigma_f B^2 L}{\rho U_b} = \frac{\sigma_f}{\mu}\frac{B^2 L^2}{\mathrm{Re}}, \tag{1.10}$$

gives the ratio of the Lorentz force to the inertial force. It illustrates the influence of the magnetic field B on the flow and is a significant parameter that can affect the electrical performance. As it will be described in details in chapter 3, the value of the interaction parameter strongly affects the efficiency and modifies the distribution of the mean velocity profiles.

Hartmann number:

$$Ha = BL\sqrt{\frac{\sigma_f}{\mu}}. \tag{1.11}$$

is a dimensionless number which gives a measure (ratio) of the relative importance of electromagnetic forces resulting from magnetic induction and the viscous forces in Hartmann flow. It determines the velocity profile for MHD flows and affects the width of boundary layers (be discussed in details at chapter 3). The Hartmann numbers used in this thesis are 69.5, 279, and 557 of Ualloy for three magnetic flux density of B = 0.03 T, 0.12 T and 0.24 T respectively.

1.3 Motivations and Objectives

Based on the review presented above, the following motivations are caused and relative studies to achieve the consequent objectives are considered necessary.

Considering the irregularity of wave motions, which encompass wide frequency and magnitude, it is predictable that the power take off system is not stable if it linked to the wave directly. From the aspect of electrical equipment, the external forces working on the liquid metals changes randomly. As a result, the response of an LMMHD power generation system to various external forces, including different magnitudes and frequencies are considered a significant issue for applications. B. Liu *et al.* examined the performance of an LMMHD power generation system in response to sinusoidal wave and irregular Pierson-Moskowitz (to simulate a real random wave) type wave [57]. The research focuses on the interaction between the float and the incident wave while the Lorentz force is simplified as the damping force acting against the flow with a constant damping coefficient. Therefore, the effects of various external input forces on the generator performance are not understood in detail. In this thesis, the responses to constant (step), square, sinusoidal and Pierson-Moskowitz type (to simulate a real random wave) external input forces are going to be examined with exact calculation of the Lorentz force, in hope of drawing universal characteristics of the LMMHD system and to provide a prospect for the utilization of a real ocean wave.

When it comes to the selection of working fluids, the choice depends on the melting point, electrical conductivity and viscosity of the various liquid metals (Factors such as price or toxicity of liquid metals are surely significant or even decisive at the commercial stage, but here only focus on their physical properties to restrict the problem from a scientific perspective.). This study tries to find the properties that affect the performance on electrical efficiency of an LMMHD generator most, and to clarify the relationship between the electrical performance and

the fluid distribution. L. Zhao *et al.* had examined the performance of a wave energy conversion system by using three kinds of liquid metals [54], which is the most similar related work to this one. Through a lumped parameter (zero-dimensional) model, the research revealed that for a fixed external force and input energy, NaK has the largest output power and highest efficiency of the three working fluids mentioned above. Note that those results strongly depend on the system components and configurations. A three dimensional simulation in this thesis is expected to be much more accurate, and the additional observation on fluid phenomena can strengthen the conclusion further.

Furthermore, turbulent flows are expected to affect the performance of MHD power generation and MHD accelerators much, and vice versa that different conditions from various applications bring influence to the MHD flows. As mentioned above, numerical simulation is suitable to observe the turbulences where experiments are almost next to impossible. As a previous study, H. Kobayashi *et al.* had discussed the typical turbulence structures at an optimal load resistance (to obtain a maximum electrical efficiency) [48]. Since various load conditions change the distribution of electrical potential and current, phenomena on fluid dynamics such as velocity and turbulent vortices, are predicted to vary correspondingly. In this thesis, the turbulent phenomena in liquid metal MHD flows under three extreme load conditions, the open-circuit, the short-circuit, and a case of externally applied current in opposite to the power generation will be examined. The use of coherent structure Smagorinsky model (CSM) is able to observe the turbulence transition among various conditions. As will be described in Appendix E, the validity of using the CSM for MHD flows under non-uniform magnetic field has already been verified by a couple of previous studies [34][47][48].

1.4 Organization of this Thesis

The thesis is organized as follows.

Chapter 1 Introductions. Introductions of both the background and objectives of this thesis are contained. Mainly, the potential of wave energy resource, along with the status quo of utilization are described with a comparison on different electrical equipment. The basic concepts of LMMHD as well as a review of related previous work are described briefly.

Chapter 2 Response of a Liquid Metal MHD Power Generation System. The responses of an LMMHD power generation system to various external inputs (constant, square, sinusoidal and Pierson-Moskowitz type) will be discussed.

Chapter 3 Influence of Working Fluid Characteristics on the MHD Generator Performance. The electrical performances of an LMMHD power generator using four different working fluids: mercury, NaK78, Galinstan and U-alloy47 are going to be examined.

Chapter 4 Turbulent Phenomena in a Liquid Metal MHD Flows. It describes the turbulent phenomena of liquid metal MHD flows under various load conditions (open-circuit, short-circuit, and with externally applied current source) with non-uniform magnetic flux densities.

Chapter 5 Conclusions. Conclusions of the entire thesis, along with some tentative thoughts on learning and further research will be expressed.

The **Appendix** contains the basic numerical methods and the critical model that be used in this thesis. The derivations of some key equations are illustrated in details.

Chapter 2 - **Response of a liquid metal MHD power generation system**

In this chapter, the responses of an LMMHD power generation system to various external inputs (constant (step), square, sinusoidal and Pierson-Moskowitz (P-M for short) type) are discussed.

Section 2.1 gives a short introduction and expresses the objectives. In Section 2.2, governing equations and assumptions are presented, and the electrical efficiency in the presence of the shape loess is derived. In Section 2.3, the response without and with the shape loss, the frequency response, and the response to P-M waves as a model of real ocean waves are discussed successively. Eventually, the results and discussion are summarized in Section 2.4.

2.1 Introduction and objectives

The liquid metal itself cannot accomplish a thermodynamic cycle. Therefore, similar to the plasma MHD power generation system, the electromagnetic fluid (liquid metal) of an LMMHD power conversion must be mixed with the thermodynamic fluid (gas or steam) to form a two-phase flow before the expansion/compression process in the MHD channel [26]. The principle of the operation of a two-phase flow LMMHD channel is that the thermodynamic fluid acts as a working medium which can expand and contract with temperature, and then drives the liquid metal forward against the electromagnetic force. Many theoretical and experimental studies of two-phase MHD have been made for a variety of systems [58] ~ [60].

However, it is difficult for the ocean wave to serve as a heat source to complete the two-phase flow operation. Instead, the “slow-moving, high-magnitude” [17] force is suitable for a single-phase flow LMMHD power conversion, where the wave force drives the electromagnetic fluid directly against the electromagnetic force to perform the conversion cycle. A lot of single-

phase LMMHD researches have been conducted for a number of years [28] ~ [34]. To the best of my knowledge, most of the studies deal with the performance of LMMHD power generators as well as the phenomena inside of that. These topics will be examined in Chapters 3 and 4 of this thesis.

In contrast, to study the response of a liquid metal MHD power generation system to various external input forces is considered a significant issue for the utilization of ocean waves. As mentioned in Chapter 1, B. Liu *et al.* had examined a wave energy conversion system and revealed the response of an LMMHD power generation system to sinusoidal and Pierson-Moskowitz type waves [57], which is similar to the topic of this chapter. However, the paper focused on a couple of parameters such as spring constant, floater radius as well as the interaction between the floater and the incident wave, while using a damping coefficient to substitute the Lorentz force produced in the LMMHD power generator. It should be much more accurate if the Lorentz force is calculated directly. In this thesis, correspondingly, the response to constant (step), square, sinusoidal and Pierson-Moskowitz (P-M for short) type external input forces is examined, and the Lorentz force is estimated exactly, in order to draw universal characteristics of the LMMHD power generation system and to provide a prospect for the utilization of a real ocean wave. Besides, as a fundamental step for designing a high efficient LMMHD power generation system, it is considered necessary to investigate the effects of

a) the physical properties of liquid metals (density and electrical conductivity),

b) the strength of magnetic flux density,

c) the shape loss due to different cross section areas,

d) the various external forces and

e) the periods of input waves on generator performance.

In this chapter, three kinds of liquid metals (NaK78 (NaK for short), U-alloy47 (Ualloy for short), and mercury) are considered. The influences of strengthened magnetic flux densities from 0.5 T to 2 T are examined. And both regular (constant (step), square, sinusoidal) and irregular (P-M type) external forces are tested. Especially, the shape loss arises from different cross section between piston driver part and generator are also considered and discussed as a preparation work for experiments in the future.

2.2 Governing equations and numerical procedure

2.2.1 An LMMHD power generation system model

An LMMHD power generation system model is proposed in this thesis as shown in Fig. 2.1. The whole power generation system housing, which includes two vertical cylinders (tanks) connected underneath by an LMMHD power generator filled up with a liquid metal as shown in Fig. 2.1(a), is assumed to be stationary under water. The LMMHD power generator consists of an MHD duct and a pair of electrodes under a dipolar magnet, which is assumed to generate a uniform magnetic flux density here. A liquid metal inside the system moves correspondingly with pistons driven by a float, which pushes piston up and down by periodical external forces. As the liquid metal flows through the LMMHD generator, electromotive force is generated in the MHD duct obeying the Faraday's law of induction, and then the kinetic energy is converted to the electric energy.

Figure 2.1(b) shows the schematic diagram, where F is an external force working on the piston; P_1 is a pressure from liquid metal produced by the Lorentz force and friction in the reverse direction; D is the diameter of tanks; The length, height and width of the MHD duct are L, a and a, respectively. The height difference between two pistons is $2z$, which is set to zero when

there is no wave working on pistons or at the initial situation. Velocity v and u are the speed of liquid metal inside the MHD duct and tanks, respectively.

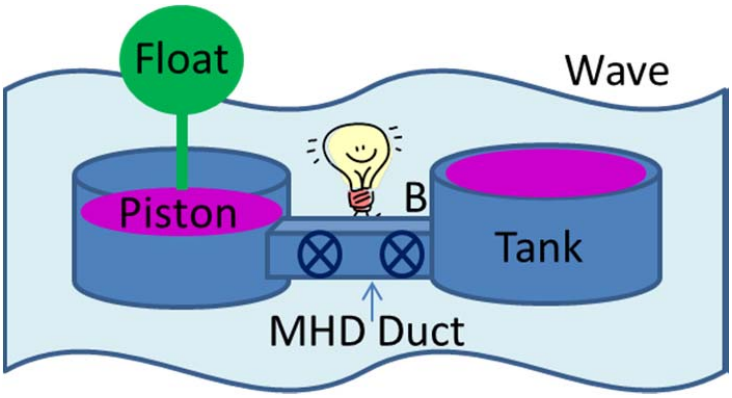

(a) Wave energy LMMHD power generation system model

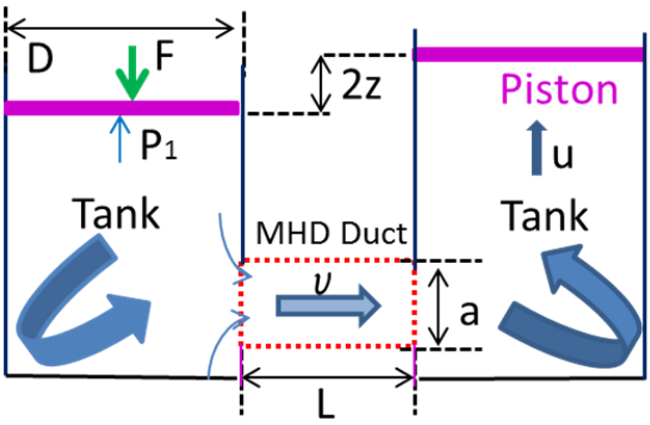

(b) Cross-sectional view

Fig. 2.1 Schematic of a wave energy LMMHD power generation system.

2.2.2 Governing equations

The governing equations of the proposed LMMHD power generation system are deduced in this section.

First, the conservation equation of mass is

$$A_{MHD}v = A_{Tank}u = A_{Tank}(dz/dt), \tag{2.1}$$

where A_{MHD} and A_{Tank} are the cross section area of MHD duct and tanks respectively.

Second, the Newton's law of the piston is

$$m(d^2z/dt^2) = F - P_1A_{Tank} - f_{loss}, \tag{2.2}$$

where m is the mass of the piston; f_{loss} is the friction between the piston and the surface of tank. Third, the energy equation, that is, the Bernoulli's equation for unsteady flows in the present system is shown as,

$$\frac{L}{g}\frac{dv}{dt} + \frac{(j\times B)L}{\rho g} + 2z - \frac{P_1}{\rho g} + \frac{P_{loss}}{\rho g} = 0, \tag{2.3}$$

where j is the current density and B is the magnetic flux density; ρ is the density of liquid metal and g is the acceleration of gravity; $2z$ results from the gravity effects; P_{loss} consists of the friction loss P_{loss1} between liquid metal and walls, and the shape loss P_{loss2} as shown below.

$$P_{loss1} = \frac{\lambda}{2}\rho\frac{L}{D}|v|v, \tag{2.4}$$

$$P_{loss2} = \frac{\lambda'}{2}\rho|v|v. \tag{2.5}$$

where λ is the coefficient of friction between fluid and surface; λ' is the coefficient of shape loss including bend loss, sudden expansion and reduction loss. Putting them all together, the equation of motion is reduced as follows.

$$\frac{dv}{dt} = \frac{F}{M} - k_av - k_bz - k_c|v|v - \frac{f_{loss}}{M}, \tag{2.6}$$

$$M = \rho LA_{Tank} + m\frac{A_{Duct}}{A_{Tank}}, \tag{2.7}$$

$$k_a = \frac{\sigma(1-K)B^2LA_{Tank}}{M}, \tag{2.8}$$

$$k_b = \frac{2\rho g A_{Tank}}{M}, \tag{2.9}$$

$$k_c = \frac{(\frac{\lambda L}{2D} + \frac{\lambda'}{2})\rho A_{Tank}}{M}. \tag{2.10}$$

where $j \times B$ in Eq. (2.3) is converted to $\sigma v B^2$ (1-K) with the electrical conductivity of liquid metal σ and the load factor K ($K = E / vB$, where E is the electric field strength in the MHD duct).

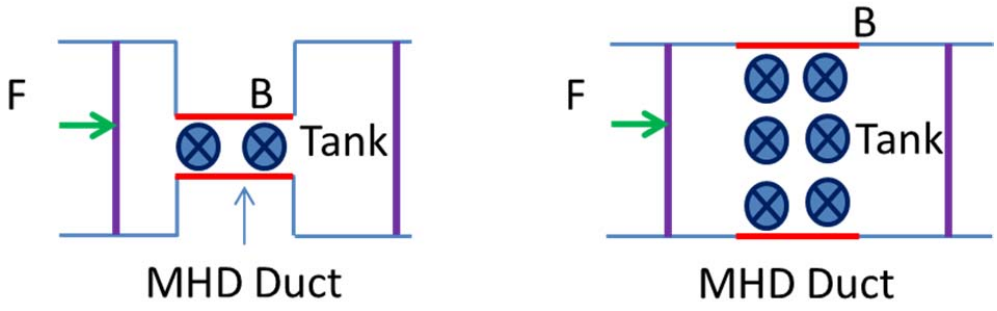

(a) $0<A_{MHD}/A_{Tank}<1$ (b) $A_{MHD}/A_{Tank} = 1$

Fig. 2.2 Simplified models with different area ratios.

To focus on problems more clearly, first the system is simplified as shown in Fig. 2.2, thus, the gravity effect in Fig. 2.1 is eliminated ($k_b z = 0$ in Eq. (2.6)). Besides, the shape loss is considered in the case of Fig. 2.2(a) when the cross section area of the tank is different from the MHD duct. The coefficients for sudden expansion and contraction losses, which are given as a function of the area ratio of the cross section for circular pipes [62], are adopted in the present work. Since smooth expansion and contraction ducts including bend ducts should be used in the practical generation system, the shape loss here can be regarded as the comprehensive influence. Because a rectangular duct is used instead of a pipe here, the following hydraulic diameter D_{MHD} and hydraulic area A^*_{MHD} are adopted.

$$D_{MHD} = 2(a * a)/(a + a) = a, \tag{2.11}$$

$$A^*_{MHD} = \pi * (D_{MHD}/2)^2. \tag{2.12}$$

Second, the friction (f_{loss} and P_{loss1}) is discarded in order to clearly understand the effect of the shape loss on the performance.

Third, the end effect [29][55], i.e., the deterioration of performance due to eddy currents in the region of non-zero gradient in the external magnetic flux density is not considered for simplification. Under the assumptions mentioned above, Eq. (2.6) is simplified to

$$\frac{dv}{dt} = \frac{F}{M} - k_a v - k_c |v| v. \tag{2.13}$$

The electrical efficiency η which is defined here as the ratio of the electrical output energy to the input energy from the external force is derived from Eq. (2.13) as

$$\eta = \frac{\int_0^t KMk_a v^2 dt}{\frac{1}{2}Mv^2 + \int_0^t Mk_a v^2 dt + \int_0^t Mk_c |v| v^2 dt}. \tag{2.14}$$

where the numerator shows the electrical output energy from the LMMHD generator; the first, second, and third terms in the denominator represent the kinetic energy of the piston and working fluids, the energy input by Lorentz force, and the energy dissipation owing to shape loss, respectively. Note that under the initial velocity of zero the kinetic energy term indicates an instantaneous value at time t, and can be dominant during the rise time. Equation (2.13) is solved using the fourth-order Runge-Kutta method with $v = 0$ as the initial conditions at $t = 0$. Various external forces F are examined as the boundary condition. At present, the external force worked on the piston (float) is assumed completely in proportion to the profile of wave. In reality, the exact force transmitted to the piston is determined by a couple of parameters such as spring constant, floater radius as well as the interaction between the float and the incident wave. For instance, B. Liu *et al.* discussed the power capture ratio for different damping coefficients of

regular/irregular waves and found that the power capture ratio in regular waves is much larger than in irregular waves [57].

2.2.3 Physical conditions

As the working fluid, NaK, Ualloy and mercury are considered. Mercury is one of the most common liquid metals, while NaK and Ualloy are fusible alloys with melting points below 50 °C. The physical properties of these metals are listed in Table 2.1, where the dimensions of the system are as D = 0.11 m, L = 0.26 m [54], with variable 'a'. The piston mass m is 6 kg. The external force is supposed at F = 5000 N. The load factor is fixed to be 0.7 throughout the present study. Almost all the conditions mentioned here are kept the same to Ref. [54] specifically, where the researches there were conducted by both numerical simulation and experiments for a couple of years. Through using the same conditions, the feasibility and correctness of this thesis can be confirmed in advance.

Table 2.1 Physical property [54].

Fluids	Density(ρ)	Electrical Conductivity(σ)
Mercury	1.35×10^{4} kg/m^3	1.04×10^{6} S/m
NaK	8.66×10^{2} kg/m^3	2.46×10^{6} S/m
Ualloy	8.85×10^{3} kg/m^3	2.30×10^{6} S/m

Under the magnetic field, the turbulence is damped by the Lorentz force that the characteristic time of the flow is computable by the ratio of the inertial force to the Lorentz force [61]. With the physical conditions of Table 2.1, the suppression of turbulence motion from magnetic damping is examined. Since the turbulence in the power generation area is immediately suppressed (less than 0.1 s for all liquid metals at B = 0.5 T), the impacts from the turbulence to

the power generation performance are considered small. Therefore, this chapter examines the MHD flow without considering the influences of turbulence.

The sudden expansion and reduction loss coefficients are shown in Table 2.2 [62].

Table 2.2 Sudden expansion and reduction loss coefficients [62].

d_1/d_2	0	0.1	0.2	0.3	0.4	0.5	0.6	0.7	0.8	0.9	1.0
f_{se}	1.00	0.98	0.92	0.82	0.70	0.56	0.41	0.26	0.13	0.04	0
f_{sc}	0.50	0.50	0.49	0.49	0.46	0.43	0.38	0.29	0.18	0.07	0

2.3 Results and discussion

2.3.1 Response without Shape Loss

As the most ideal case, when the area ratio between the tank and the MHD duct is unity, λ' (k_c, shape loss factor) becomes zero. Then, Eq. (2.13) is simplified further as

$$\frac{dv}{dt} = \frac{F}{M} - k_a v, \tag{2.15}$$

which is solved analytically for a constant force F (as a step function) as follows,

$$v = \frac{F}{Mk_a}(1 - e^{-k_a t}), \tag{2.16}$$

$$\eta = \frac{\int_0^t KMk_a v^2 dt}{\frac{1}{2}Mv^2 + \int_0^t Mk_a v^2 dt}. \tag{2.17}$$

It can be seen from Eq. (2.16) that F/Mk_a corresponds to the terminal velocity after a transition process. Figure 2.3 shows the transition processes of mercury, Ualloy, and NaK under magnetic flux density of 0.5 T and three magnetic flux densities of 0.5 T, 1 T, and 2 T in mercury at the very initial time.

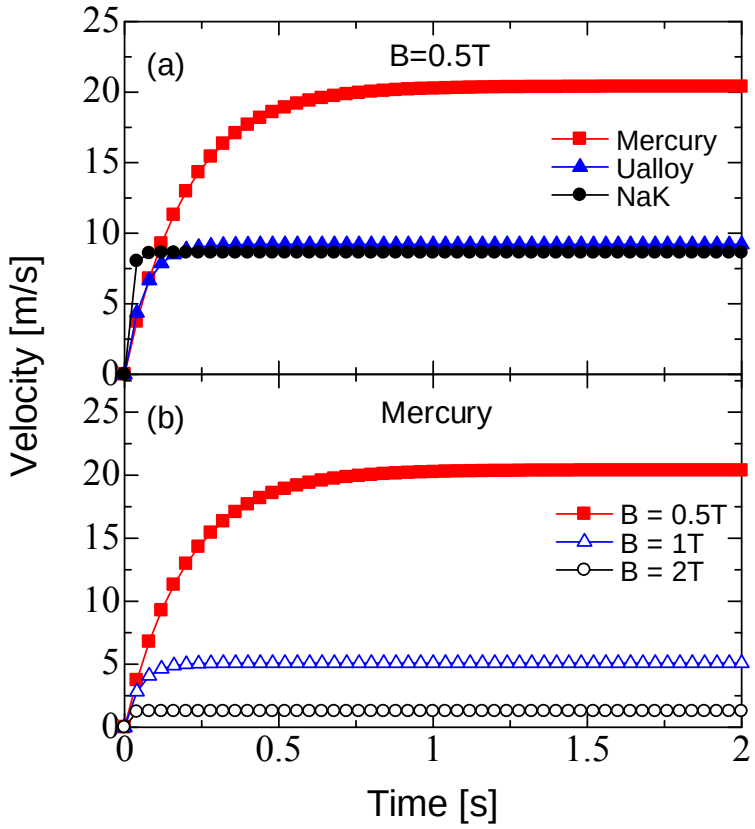

Fig. 2.3 Velocity transition processes of (a) mercury, Ualloy, and NaK under magnetic flux density of 0.5 T, and (b) magnetic flux densities of 0.5 T, 1 T, and 2 T in mercury.

Figure 2.3(a) shows all of velocity climb sharply from 0 to constant values and then level off there with time goes on, where NaK reaches the stable value first while mercury has a largest stable velocity among the three liquid metals. Figure 2.3(b) illustrates the stable velocity of mercury decreases as the magnetic flux density is strengthened, but the larger the magnetic flux density, the shorter the rise up time.

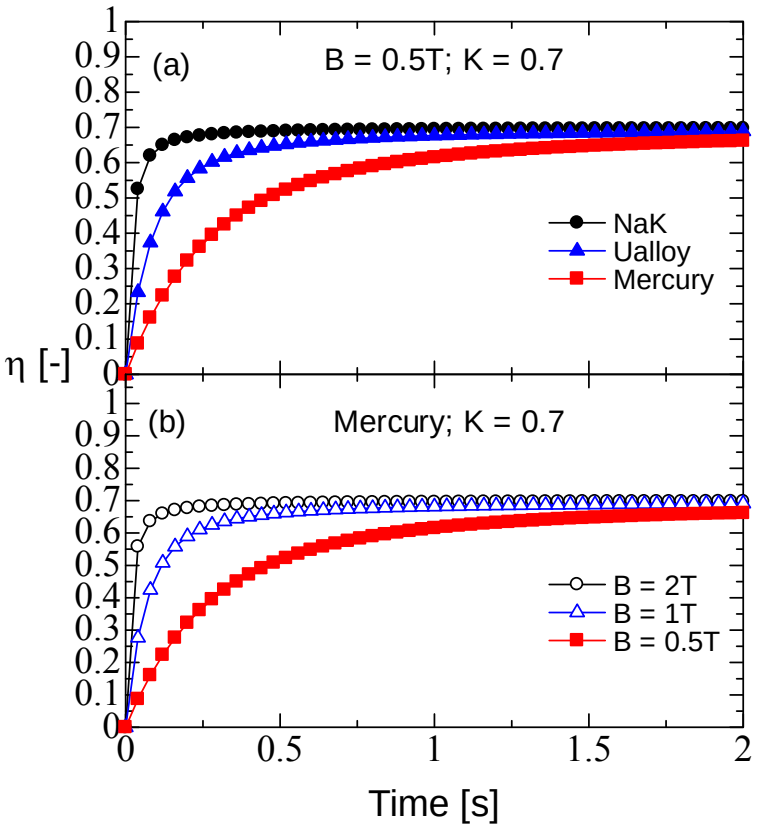

Fig. 2.4 Electrical efficiency transition processes of (a) NaK, Ualloy, and mercury under magnetic flux density of 0.5 T, and (b) magnetic flux densities of 2 T, 1 T, and 0.5 T in mercury. The load factor is 0.7.

Since the power is in proportional to v^2, $1/\sigma B^2$ in F/Mk_a plays a critical role if other parameters such as F, K, L and A_{Tank} are constant (refer to Eqs. (2.6) ~ (2.10) for details). On the other hand, the characteristic time ($1/k_a$) can be affected by fluid's density ρ additionally as $\rho/\sigma B^2$ with neglecting the piston mass. In Eq. (2.15), as time advances, $1/2Mv^2$ becomes negligibly small compared to the integral terms, and then the electrical efficiency finally approaches the value of load factor K shown in Fig. 2.4, which illustrates the electrical efficiency transition processes of NaK, Ualloy, and mercury under magnetic flux density of 0.5 T, and three magnetic flux densities of 2 T, 1 T, and 0.5 T in mercury, where the load factor is set to 0.7.

Figure 2.5 shows the velocity, the output power, and the electrical efficiency in the steady state as a function of magnetic flux density. The electrical efficiency obviously approaches 0.7 (the load factor K) for all fluids, which is independent of working fluids and magnetic flux density. Under the constant F, however, since the terminal velocity is proportional to $1/\sigma B^2$, a liquid metal with low electrical conductivity (mercury here) working under lower magnetic flux density provides higher terminal velocity, consequently larger output power.

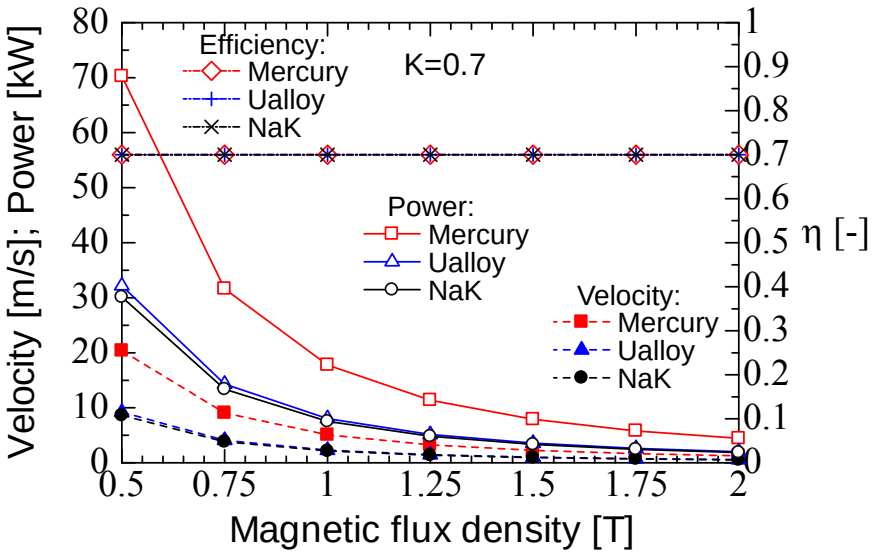

Fig. 2.5 Velocity, power, and electrical efficiency as a function of magnetic flux density.

2.3.2 Response with Shape Loss

Equation (2.13) with shape loss can be analytically solved for a constant force F. In the steady state, the electrical efficiency including the shape loss is expressed with K as follows (with 1-K be offset at both the denominator and the numerator),

$$\eta = \frac{K}{1+\frac{1}{2}\left(\sqrt{1+\frac{1}{S(1-K)^2}}-1\right)}, \qquad S = \frac{\sigma^2 B^4 L^2 A_{Tank}}{2F\lambda'\rho}. \tag{2.18}$$

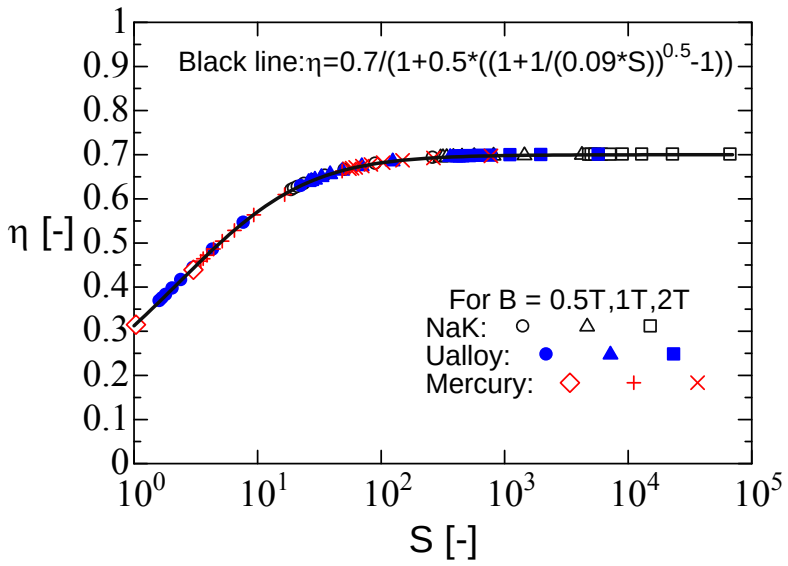

Fig. 2.6 Electrical efficiency as a function of coefficient *S*.

It is found from the above relation that the electrical efficiency is characterized by a parameter *S* with the coefficient of shape loss λ' as well as ρ, σ and *B*. Using the exact physical properties of each liquid metal (Table 2.1) and the sudden expansion and reduction loss coefficients of different area ratios (Table 2.2), the electrical efficiency are able to be calculated. Figure 2.6 shows the electrical efficiencies of NaK, Ualloy, and mercury as a function of coefficient *S*. It means through increasing the coefficient *S* the electrical efficiency would be improved, where if *S* is larger than 100 the efficiency would get close to its stable value. Besides, coefficient S itself shows that magnetic flux density has an influence (quartic) that is much bigger than electrical conductivity (quadratic) and the shape loss as well as density (linear).

Besides, a small *F*, which means a weaker external force, will not deteriorate the electrical efficiency. These are considered useful information for references.

Figure 2.7 shows the output power and the electrical efficiency in the steady state for a sinusoidal force with a period of 10 s and amplitude of 5000 N as a function of the area ratio. Obviously, the power and the electrical efficiency deteriorate for all the fluids with decreasing

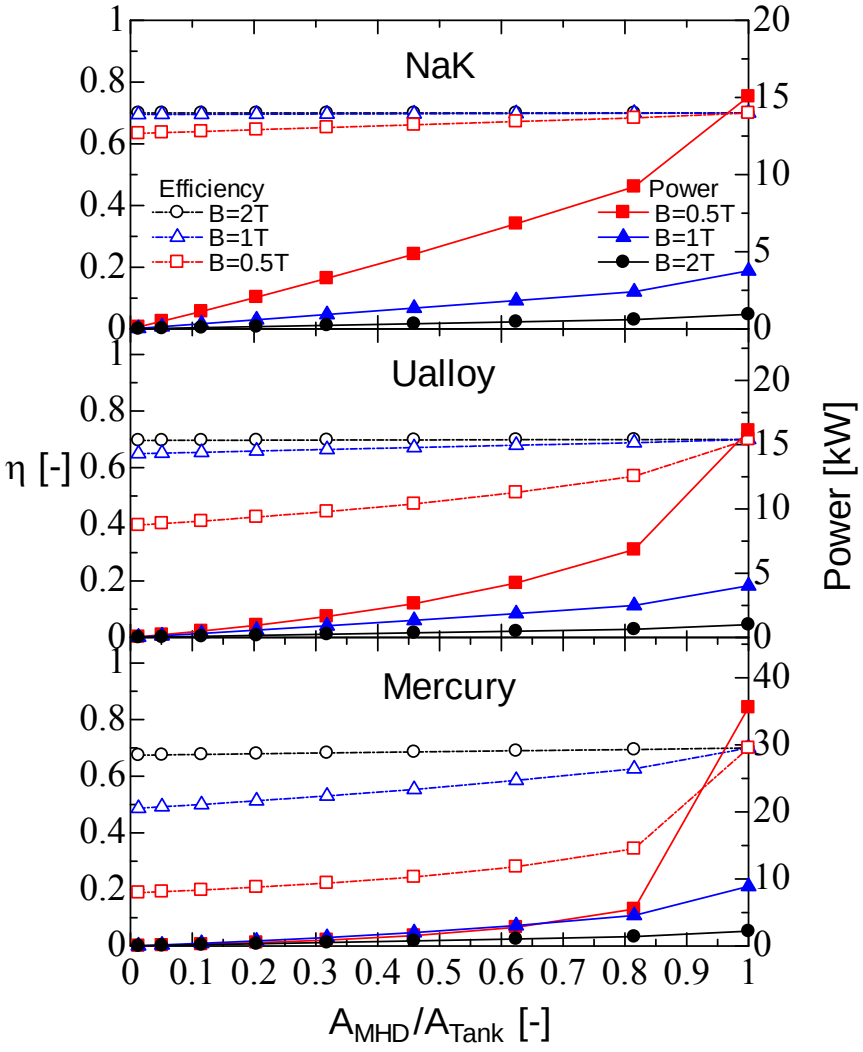

Fig. 2.7 Power and electrical efficiency as a function of area ratio.

the area ratio, which leads to the increase in the shape loss. It is shown that mercury among three fluids presents abrupt decline in the power and the efficiency relatively, while the deterioration for NaK is moderate. These results can be explained from Eq. (2.18), although it is derived for a constant force. Thus, the deterioration can be mitigated by using NaK with low density and high electrical conductivity, that is, with large S. Furthermore, the other important suggestion is that the deterioration can be compensated by the increase in the applied magnetic flux density. In fact, as clearly observed in this figure, all of the fluids present an electrical efficiency near 0.7 (assumed K) for a high magnetic flux density of 2 T even when the area ratio is small. Thus, the parameter S derived here is quite useful for the estimate of the electrical efficiency in the presence of the shape loss.

2.3.3 Frequency Response with Shape Loss

To clarify the influence of frequency (or period) in a regular wave for various working fluids with the shape loss, the power and the electrical efficiency for a sinusoidal force at the area ratio 0.62 and magnetic flux density 0.5 T are examined as shown in Fig. 2.8(a) as a function of the period. It can be seen roughly that with shortening the period, the output power is decreased, whereas the electrical efficiency seems to recover toward the ideal value of 0.7. Since liquid metal never reaches the terminal velocity for short period, the output power becomes low, whereas the efficiency becomes high because the shape loss term in Eq. (2.14) shrinks owing to the small velocity. On the other hand, with elongating the period, the electrical efficiency decreases and approaches the value with the shape loss for a constant force. Obviously, NaK is superior to other liquid metals because of its small ρ/σ, that is, quick response and effectively small shape loss.

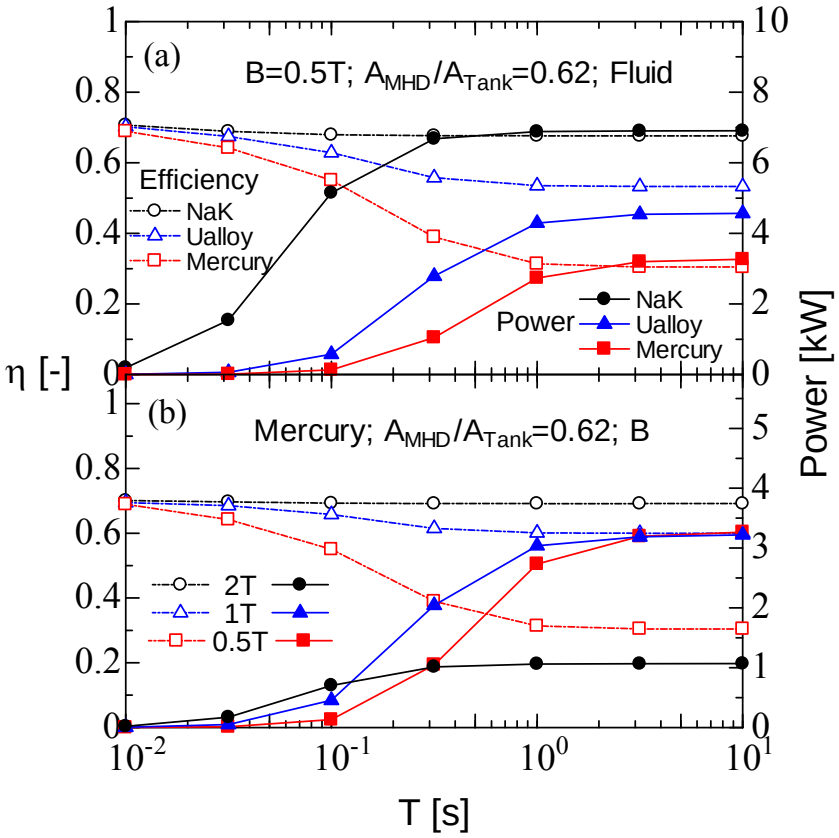

Fig. 2.8 Power and electrical efficiency as a function of period.

As seen from the discussion about the parameter *S* in the previous section, the increase in the magnetic flux density is helpful to obtain high electrical efficiency for liquid metal with relatively large ρ/σ such as Ualloy and mercury. Figure 2.8(b) illustrates the output power and the electrical efficiency of mercury under three different magnetic flux densities for the area ratio of 0.62. Even for long period, the electrical efficiency does not deteriorate in the case of B = 2 T, although the output power is reduced as can be predicted from Fig. 2.3.

In order to clarify the oscillation of the piston under a periodic force, the amplitude and displacement of the piston under two different area ratios are illustrated as a function of period in Fig. 2.9. Here the displacement means the deviation of the center-position, originating from the

initial assumptions of $z = 0$ and $v = 0$ at $t = 0$, which can be one of the points of attention for designing MHD generator system. In the case of no shape loss (Fig. 2.9(a)), for $F = F_0 sin\omega t$ with angular velocity ω, the amplitude and the displacement are analytically derived as $F_0/[M\omega(k_a^2+\omega^2)^{0.5}]$ and $F_0/(Mk_a\omega)$, respectively. The critical derivation based on Eq. (2.15) is shown as follows.

$$\frac{dv}{dt} + k_a v = \frac{F_0 sin\omega t}{M}, \tag{2.19}$$

$$\frac{dz}{dt} = u = v. \tag{2.20}$$

with the assumed initial conditions, the solutions are

$$v = \frac{F_0}{M(k_a^{\,2} + \omega^2)}\left(\omega e^{-k_a t} + k_a sin\omega t - \omega cos\omega t\right), \tag{2.21}$$

$$z = \frac{F_0}{Mk_a\omega} - \frac{F_0}{M\left(k_a^{\,2} + \omega^2\right)}\left(\frac{\omega}{k_a}e^{-k_a t} + \frac{k_a}{\omega}cos\omega t + sin\omega t\right). \tag{2.22}$$

After the transient process passed, which means the exponential term in Eq. (2.22) disappeared, the position z of piston would become as

$$\begin{gathered} z = \frac{F_0}{Mk_a\omega} - \frac{F_0}{M\omega\sqrt{k_a^{\,2} + \omega^2}}\sin\left(\omega t + \varphi\right), \\ where\, \varphi = \arctan\left(\frac{k_a}{\omega}\right). \end{gathered} \tag{2.23}$$

The equation above shows the piston oscillates sinusoidally around the displacement (the deviation of the center-position) of $F_0/(Mk_a\omega)$ as the final state.

Figure 2.9(a) indicates that the displacement of the piston is always larger than the amplitude, and for a longer period, the amplitude and the displacement become large and equal, then those are roughly proportional to $1/\sigma$. As shown in Fig. 2.9(b), on the other hand, the shape loss can suppress the increase in the amplitude and the displacement with shrinking the

difference among liquid metals. It can be seen generally from Fig. 2.8 and Fig. 2.9 that the period of several seconds is suitable from a viewpoint of response of liquid metal and piston (float) motion, which can meet the real ocean wave with the period of the order of seconds and the amplitude of the order of meters.

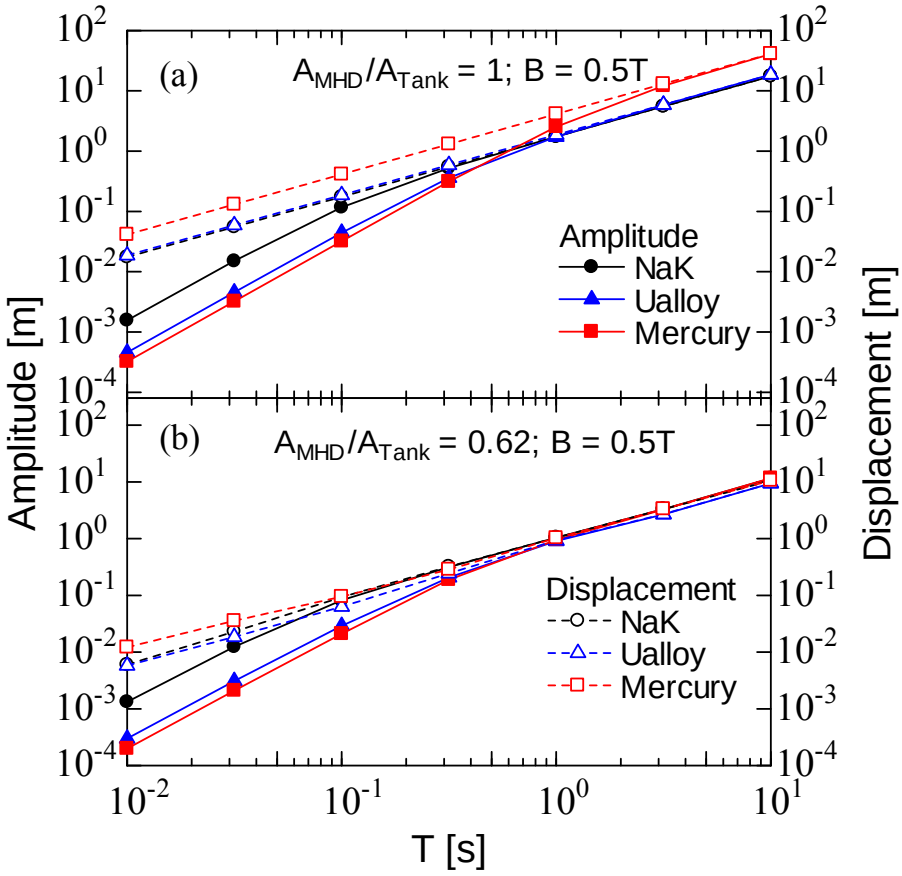

Fig. 2.9 Amplitude and displacement of the piston as a function of period.

2.3.4 Response to P-M wave force

In the final session, the response to irregular waves with the P-M spectrum, which was developed by Pierson and Moskowitz from measurements in the North Atlantic during 1964 [63] is examined.

It assumes that if the wind blows steadily for a long time over a large area, then the waves will eventually reach a point of equilibrium with the wind. The P-M spectrum is one of the simplest descriptions for the energy distribution [64].

The frequency distribution of ocean wave energy is defined with a significant wave height H_s and energy period T_e. The P-M spectrum is expressed as Eq. (2.24) and examples of generated waves in time zone are shown in Fig. 2.10(a).

$$S(\omega) = 131.5 H_s^2 T_e^{-4} \omega^{-5} \exp(-1054 T_e^{-4} \omega^{-4}), \tag{2.24}$$

$$\begin{aligned} x(t) &= \sum_{i=1}^{N} x_i(t) \\ &= \sum_{i=1}^{N} 2\sqrt{S(f_i)\Delta f}\, \cos(2\pi f_i t + \delta_i), \end{aligned} \tag{2.25}$$

$$\begin{aligned} \Delta f &= \frac{1}{\Delta t}, \quad \omega_i = 2\pi f_i, \\ 0 &\le \delta_i \le 2\pi, \quad i = 1, 2, \cdots, N. \end{aligned} \tag{2.26}$$

Equation (2.24) ~ (2.26) are used to produce the P-M wave in time zone by an inverse Fourier transform numerically (refer to Appendix A), where Δt is the time step which is set to $T_e/1000$; a random number between 0 and 2π is assigned to δ_i; and N is 5000 here. It means that the generated P-M wave is a combination of thousands of simple sinusoidal waves with different frequencies [65] ~ [67]. The generated waves for H_s = 1 m and T_e = 1 s, 5 s, 10 s are shown in Fig. 2.10(b), where X_{wave} is a dimensionless number giving the ratio of amplitude $x(t)$ to half of the significant wave height H_s. As mentioned above, the interaction between the float and the incident wave in reality is quiet complex and still under research, the external force is considered as in proportion to X_{wave} for simplification in this thesis.

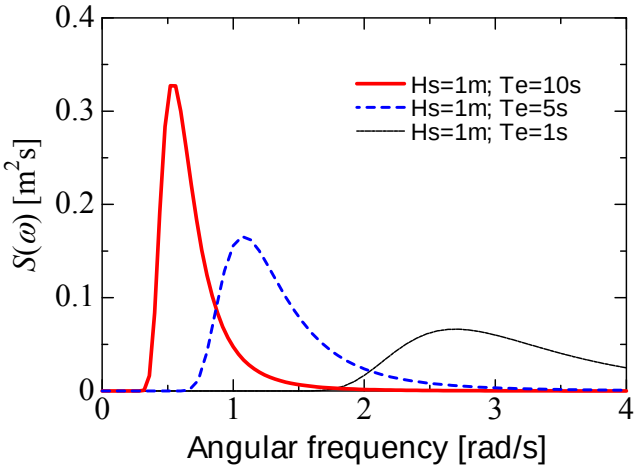

(a) P-M spectra

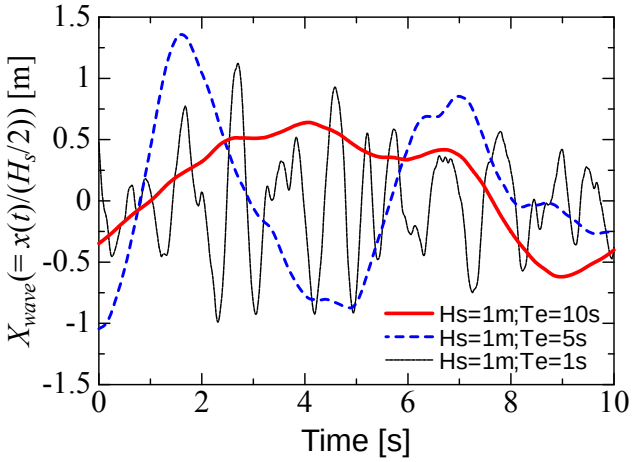

(b) P-M waves in time zone

Fig. 2.10 Pierson-Moskowitz spectra and the generated waves in time zone.

To compare the response to various inputs, the effective value is equalized, that is, the root mean square (RMS) F_{rms} of the input forces from regular and irregular waves are set to be the same. Here, the effective value F_{rms} is defined as

$$F_{rms} = \sqrt{\langle F^2 \rangle} = \sqrt{\frac{1}{N}\sum_{i=1}^{N}(F_{wave}X_{wave,i})^2} = F_{wave}\sqrt{\langle X_{wave}{}^2 \rangle}, \tag{2.27}$$

where <A> indicates the time average of A (F^2 or X_{wave}^2), X_{wave} for a square wave only takes two values, -1 and 1; for a sinusoidal one from -1 to 1; for a P-M wave generally from -1 to 1 with a random distribution as shown in Fig. 2.10(b). For instance, if F_{rms} = 5000 N is set, so that F_{wave} = 5000 N for the square wave. For the sinusoidal wave, F_{wave} = 7070 N, because $(<X_{wave}^2>)^{0.5}$ becomes $1/2^{0.5}$. For the P-M wave, F_{wave} is calculated at around 20000 N. Note that these specific values are not actually measured in real ocean waves, but evaluated for a fair comparison among different external forces, which would not affect the conclusion essentially.

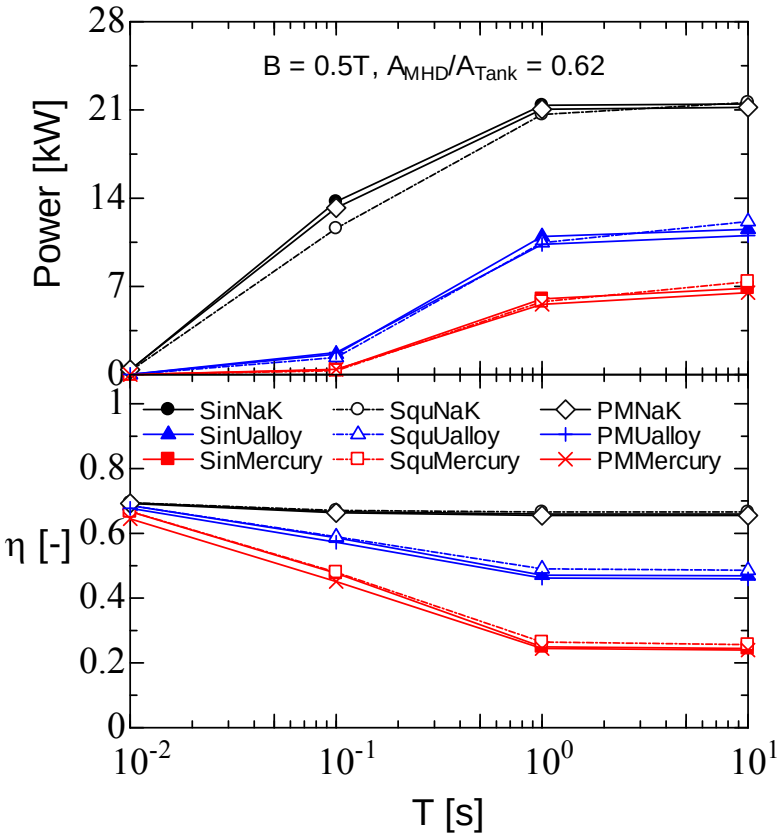

Fig. 2.11 Power and electrical efficiency as a function of period.

The power and the electrical efficiency for three working fluids and three waveforms are shown as a function of the period in Fig. 2.11. As elongating the period, the output power

increases and saturates, in contrast, the electrical efficiency presents an inverse trend. These profiles seem to be the same as Fig. 2.8(a). It is noted that there is little difference among different types of input waves. Although the P-M wave has various components of frequency, the wave is produced as a linear combination of sinusoidal wave adding random phases. Therefore, if the effective value of the P-M wave input is the same as that of the regular one, the performance (the output power and the electrical efficiency) becomes almost the same. Thus, it is reasonable that P-M wave force leads the similar performance to regular wave forces. This feature can provide a prospect for the utilization of a real ocean wave, although the transfer from wave motion to piston motion should be examined precisely [57].

2.4 Summary

The analyses on the response of a liquid metal MHD generation system to various external inputs of piston force (constant (step), square, sinusoidal, P-M waves) with three different working fluids (NaK, Ualloy, and mercury) have been conducted. The following conclusions can be drawn.

(1) The electrical efficiency in the presence of the shape loss can be expressed as Eq. (2.16) for a constant force, and is characterized by a parameter S with the coefficient of shape loss λ' as well as ρ, σ and B. Although the electrical efficiency is reduced owing to the shape loss, the deterioration can be mitigated by using NaK with low density and high electrical conductivity and compensated by the increase in the applied magnetic flux density.

(2) From the examination about the frequency response, the period of several seconds is suitable from a viewpoint of response of liquid metal and piston (float) motion, which can meet the real ocean wave with the period of the order of seconds and the amplitude of the order of meters.

(3) The irregular force input based on the P-M wave gives no big difference with the regular forces when the effective value of the input is the same, which can provide a prospect for the utilization of a real ocean wave.

In the present study, the electrical efficiency has been mainly examined in the presence of the shape loss for various manners of external piston force with different working fluids. Although some fundamental and universal aspects in the response of LMMHD power generation system have been clarified in the present study, the coefficient of shape loss λ' which is one of the most important parameters was treated as an apparent parameter in order to examine the influence on the electrical efficiency comprehensively. Obviously, more quantitative and adequate treatment is needed for designing and evaluating a practical power generation system. Furthermore, the size of each component, and the configuration in the LMMHD power generation system should be optimized individually in accordance with the real situations in the installation site.

Chapter 3 - **Influence of Working Fluid Characteristics on the MHD Generator Performance**

In this chapter, the electrical performances of a liquid metal magnetohydrodynamic (LMMHD) power generator using four different working fluids (mercury, NaK78 (NaK for short), Galinstan and U-alloy47 (Ualloy for short)) are discussed.

In Section 3.2, governing equations and numerical conditions are presented. In Section 3.3, numerical results are discussed. First the electrical efficiency is assessed, and then the influence of interaction parameter on the MHD flows and the electrical efficiency are investigated successively. In Section 3.4, the results and discussion are summarized and the conclusions are drawn.

3.1 Introduction and Objectives

In fluid mechanics, the Reynolds number (Re) is generally used to help predict similar flow patterns in different fluid flow situations. As the saying goes, “Turbulence is not a feature of fluids but of fluid flows” [77]. Many fundamental experiments on LMMHD generators have been carried out with one kind of liquid metal, either mercury or NaK [30][49][56], as well as the related numerical simulations have been conducted to understand typical MHD duct flows [42][68][69]. As mentioned in chapter 1, a non-uniform magnetic field distribution in the stream-wise direction [68] and electrically conducting walls [69] are well-known to produce M-shaped stream-wise velocity profiles, or the so-called wall jet flows.

On the other hand, to discuss the electrical performance of an LMMHD generator, the features of various working fluids (liquid metals in this thesis) must be considered additionally. When it comes to the selection of liquid metals, the choice depends on physical properties, such as the melting point, electrical conductivity and viscosity of the liquid metal. For applications

involving the ocean, liquid metals with low melting points, such as mercury, NaK and Ualloy, are candidates. Y. Peng *et al.* describe a wave energy conversion system [17]. It consists of two vertical cylinders connected underneath by an LMMHD generator and the whole system is filled with a liquid metal. A lumped parameter (zero-dimensional) model of the system revealed that for a fixed external force and input energy, NaK has the largest output power and the highest efficiency of the three working fluids mentioned above. The maximum output power of NaK is about three times that of Ualloy and eight times that of mercury. While the average efficiency of NaK is about two times that of Ualloy and five times that of mercury. Note that those results strongly depend on the system components and configuration, and the flow rate or bulk velocity of the liquid metal changes in response to the piston motion.

In contrast, in the present thesis, the net performance of an LMMHD generator for a constant flow rate is examined through a three dimensional numerical calculation, in order to draw more universal and precise conclusions. The influence of working fluid characteristics on the performance of an LMMHD generator for constant Reynolds number is focused on. As the working fluid, mercury, NaK, Ualloy and Galinstan with low melting point are considered here.

Only the basic physical properties of liquid metal are considered to focus their effects on the performance of the LMMHD generator, especially, the influence of interaction parameter on the MHD flows and the electrical efficiency is mainly discussed, which depends on the Lorentz force and the difference in the electrical conductivity between the liquid metal and the electrodes (including the lead cable connected to the load). Note that the price, the causticity, and the possible toxicity of liquid metals are not considered at this stage.

3.2 Governing Equations and Numerical Methods

3.2.1 Governing Equations for Resolved-scale Fields

The governing equations are composed of a filtered continuity equation, filtered incompressible Navier–Stokes equations accompany with the Lorentz force, filtered Maxwell's equations, and the filtered Ohm's law as follows (Filtering in the context of LES means a mathematical operation to remove a range of small scales from the solution).

Continuity equation

$$\nabla \cdot \vec{u} = 0, \tag{3.1}$$

Navier-Stokes equations

$$\frac{\partial \vec{u}}{\partial t} + \nabla \cdot (\vec{u}\vec{u}) = -\frac{1}{\rho}\nabla \vec{P} + \nabla \cdot \tau + \frac{1}{\rho}(\vec{j} \times \vec{B}) + \vec{F}, \tag{3.2}$$

Maxwell's equations

$$\nabla \times \vec{E} = -\frac{\partial \vec{B}}{\partial t}, \tag{3.3}$$

$$\nabla \times \vec{B} = \mu_0 \vec{j}, \tag{3.4}$$

Ohm's law

$$\vec{j} = \sigma_f (\vec{E} + \vec{u} \times \vec{B}). \tag{3.5}$$

where $\vec{u}$ is the velocity vector with components u_i , the sub-grid scale stress tensor is $\tau = \tau_{ij} = (\nu_m + \nu_e)(\frac{\partial u_i}{\partial x_j} + \frac{\partial u_j}{\partial x_i})$, ν_m is the molecular viscosity, ν_e is the turbulent eddy viscosity, $\vec{P}$ is the pressure, $\vec{j}$ is the current density vector, $\vec{F}$ is the external force vector, $\vec{E}$ is the electric field vector, and μ_0 is the permeability constant. The magnetic flux density $\vec{B}$ is

composed of an external magnetic flux density (0, 0, B_z) and the induced magnetic field B_i, which was assumed to be small in comparison to the steady field B_z.

The so-called A-ϕ method [78][79] is referred for the solutions of the vector potential $\vec{A}$ and the electric potential ϕ to calculate the electric field $\vec{E}$ and the induced magnetic field B_i as follows. (Appendix B has further details about the numerical procedures)

Poisson equation for the vector potential

$$\nabla^2 \vec{A} = -\mu_0 \vec{j}, \tag{3.6}$$

where

$$\vec{E} = -\nabla\phi - \frac{\partial \vec{A}}{\partial t}, \tag{3.7}$$

$$\nabla \times \vec{A} = \vec{B}_i. \tag{3.8}$$

Poisson equation for the electric potential

$$\nabla^2 \phi = \nabla \cdot (\vec{u} \times \vec{B}). \tag{3.9}$$

The Coulomb gauge below is adopted.

$$\nabla \cdot \vec{A} = 0. \tag{3.10}$$

3.2.2 Computational Domain and Boundary Conditions

The sketch of the computational domain is shown in Fig. 3.1. It stands for a liquid metal MHD power generator with two opposing electrodes located in the middle region. A load resistance is connected to the centers (in the x-z plane) of the outer surfaces of the electrodes. A liquid metal flows toward the $+x$ direction. In reality, the reciprocating motion of wave oscillates the liquid metal that the MHD flows should be considered as oscillatory flow. The one direction flow here is a simplification for assuming a certain fragment of the oscillatory flow (a few seconds of period) in a half period.

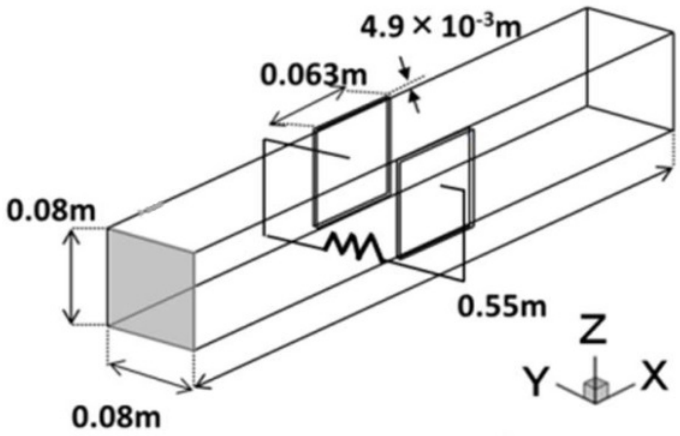

Fig. 3.1 Sketch of the computational domain.

The duct width is $L = 0.08$ m and its length in the stream-wise direction is 0.55 m. The size of the LMMHD generator here is to simulate the size of a generator (Height 0.01m, width 0.05m, length 0.1m) examined by experiments and numerical simulations [49] conducted by T. Maeda *et al*. An equally spaced grid is used in the x direction ($\Delta x = 1.57\times10^{-2}$ m), while a stretched grid is adopted in the y and z directions (Δy, $\Delta z = 2.48\times10^{-4}$~$2.41\times10^{-3}$ m). The numbers of grid points are 36, 64 and 64 for x, y and z directions, respectively. The grid dependency under various magnetic flux densities has been verified. It is considered that there is no apparent grid dependency problem by using the present grids number for a magnetic flux density up to 0.24 T. A staggered grid system is used for velocity. The region in between the electrodes ($x = 0.27$~0.33 m) is called the power generation region. The central positions in the y and z directions are $y = 0.04$ m and $z = 0.04$ m. Mean velocity profiles at these positions will be shown later. The electrodes are made of copper (5.90×10^{7} S/m) and have dimensions of 0.063 m, 4.87×10^{-3} m and 0.08 m in x, y and z directions, respectively.

An external non-uniform magnetic field is induced in the +z or vertical direction, and it has no distribution in the x and y directions as shown in Fig. 3.2. The maximum (B_{z0} = 0.12 T in the figure) is illustrated by dotted lines, whereas the value in both the inlet and outlet regions is 0. The profile of magnetic flux density is the same as that in a previous experiment [49].

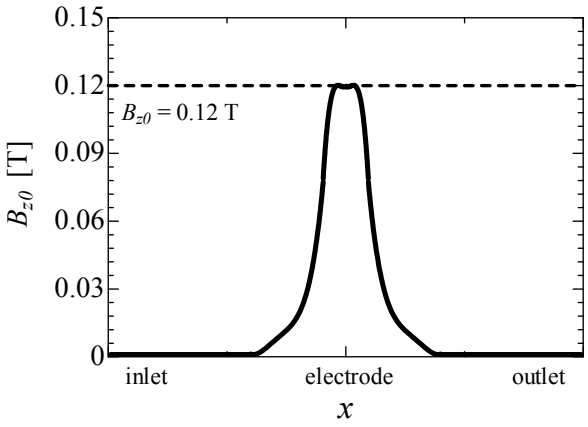

Fig. 3.2 Externally applied magnetic flux density.

Fully developed turbulent duct flow at friction Reynolds number Re_τ = 180 is introduced at the inlet. The offered database on Re_τ =180 of general turbulent flows [44] can be criteria of judgment for Non-MHD flows generated from the driver region. The friction Reynolds number 180 is about 4887 for Ualloy (4882, 4881, and 4877 for NaK, Galinstan, and mercury, respectively) in general Reynolds number. The time step for NaK is $\Delta t = 1.00\times10^{-3}$ s, for Galinstan it is $\Delta t = 2.56\times10^{-3}$ s, for Ualloy it is $\Delta t = 3.08\times10^{-3}$ s and for mercury it is $\Delta t = 8.36\times10^{-3}$ s, all of which correspond to the same dimensionless time. The convective outflow condition is adopted for the main region. A no-slip condition for velocity is imposed on the walls. A no-penetration condition of the electric current is applied to the insulated walls and the Dirichlet boundary condition for the vector potentials is given by

$$\overline{A}_S = \int_V \frac{\mu_0 \overline{j}}{r} dV, \tag{3.11}$$

where S represents the surface computational domain; V indicates the volume of entire domain; and r is the distance between surface element and a certain element in the computational domain for the electric current.

3.2.3 Physical Properties and Numerical Methods

As the working fluid, NaK, Galinstan, Ualloy and mercury are considered. Mercury is one of the most common liquid metals, while NaK, Galinstan and Ualloy are fusible alloys with melting points below 50 °C. The physical properties of the working fluids are listed in Table 3.1 [54].

Table 3.1 Physical property of working fluids [54].

Fluids	Density(ρ)	Viscosity(μ)	Electrical Conductivity(σ)
Mercury	1.35×10^{4} kg/m^3	0.16×10^{-2} Pa・s	1.04×10^{6} S/m
NaK	8.66×10^{2} kg/m^3	0.66×10^{-3} Pa・s	2.46×10^{6} S/m
Galinstan	6.44×10^{3} kg/m^3	0.24×10^{-2} Pa・s	2.30×10^{6} S/m
Ualloy	8.85×10^{3} kg/m^3	0.27×10^{-2} Pa・s	2.30×10^{6} S/m

To eliminate any potential redundancies among different working fluids, a kinetic energy equation derived from Eq. (3.2) in the steady state is normalized by the duct width D and the bulk velocity U_b as follows.

$$\begin{aligned} -N(j_y^{*2} + j_y^*\nabla_y^*\varphi^* + j_x^{*2} + j_x^*\nabla_x^*\varphi^*) \\ - u_x^* \frac{\partial P^*}{\partial x^*} + \frac{1}{\mathrm{Re}} u_x^*\nabla^{*2}u_x^* + u_x^*F_x^* = 0, \end{aligned} \tag{3.12}$$

where the asterisk denotes dimensionless variables. The Reynolds number Re and the interaction parameter N are defined by

$$\mathrm{Re} = \frac{U_b D}{\nu_m}, \tag{3.13}$$

$$N = \frac{\sigma B^2 D}{\rho U_b} = \frac{\sigma}{\mu}\frac{B^2 D^2}{\mathrm{Re}}. \tag{3.14}$$

Just like the Reynolds number, which is a dimensionless number giving the ratio of the inertial force to the viscous force; the interaction parameter is the ratio of the Lorentz force to the inertial force. The interaction parameter is one of the most important and critical parameters and its influence on the performance and the fluid flow will be discussed later in detail. The derivation of Eq. (3.12) is described in Appendix C.

Different from chapter 2, the input here is limited to the generator that is defined as the work done by the pressure difference. The Joule heating loss in the electrodes as well as the eddy current loss caused by the non-uniform magnetic field are calculated exactly by three dimensional simulations. Electrical efficiency, defined as the ratio of electrical power output to the work done by the pressure difference, is derived from Eq. (3.12) and is given by

$$\eta = \frac{K(1-K) - \dfrac{\sigma_f}{\sigma_e} G(1-K)^2 - k_x(k_x + a)}{K(1-K) + (1-K)^2 + a(k_x + a) - \dfrac{1}{\mathrm{Re}\, N}\dfrac{\int u_x^* \nabla^{*2} u_x^* dV}{\int u_x^{*2} B^{*2} dV}}, \tag{3.15}$$

$$K = \frac{-\nabla_y^* \varphi^*}{u_x^* B^*}, \tag{3.16}$$

$$k_x = \frac{-\nabla_x^* \varphi^*}{u_x^* B^*}, \tag{3.17}$$

$$a = \frac{u_y^*}{u_x^*}. \tag{3.18}$$

where K is the load factor defined by the ratio of the electric field to the open-circuit electric field; σ_e and σ_f are the conductivity of the electrodes and the working fluid respectively; k_x is the load factor in the x direction, which is related to electrical loss as shown in Ref. [28], and a is the velocity ratio (see Appendix D for the deduction). The second and third terms in numerator, and the fourth term in denominator in Eq. (3.15) represent the Joule heating loss in the electrodes, the eddy current loss due to M-shaped stream-wise velocity distributions and the wall friction loss, respectively. The parameter G is the ratio of the Joule heating in the liquid metal and the electrodes. Note that the fourth term in denominator is always positive, that is, always dissipative.

For the spatial discretization and time marching scheme, the second-order central finite difference method and the second-order Adams–Bashforth method are used, respectively. The simplified marker-and-cell (SMAC) scheme is adopted for the coupling between velocity and pressure. Poisson equations for pressure, electric potential and vector potentials are solved using the so-called Bi-CGSTAB method (refer to Appendix B for details). For the LES, the coherent structure Smagorinsky model (CSM) is selected.

3.3 Results and discussion

3.3.1 Typical MHD Flow Behaviors

To begin with, the typical MHD flows in this research is presented. Figure 3.3 shows the instantaneous distributions of (a) the electric current density and (b) the velocity in the x-y plane (z = 0.04 m) of the duct. The instantaneous distribution of electric current density, Lorentz force, and the velocity in the Hartmann layer (x-z plane) were also examined in this research. Generally, compared to the sidewall layer, the Hartmann layer (x-z plane) has a uniform distribution and considering the direction of the arrows, it is much easier to explain the phenomenon by using the distribution from the sidewall layer.

In Fig. 3.3 (a), arrows with a same length show the directions of current density, while the strengths shown by the multi-coloring scale represent the values of current density. Judging by these arrows, the electric currents mainly flow from above (anode) to below (cathode) and a pair of eddy currents is visible in the upstream and downstream regions of the electrodes. This is the so-called "end effect from a finite magnet" due to the change (gradient) of vertical magnetic flux density along the stream-wise direction (Fig. 3.2). A similar phenomenon was observed in Ref. [55].

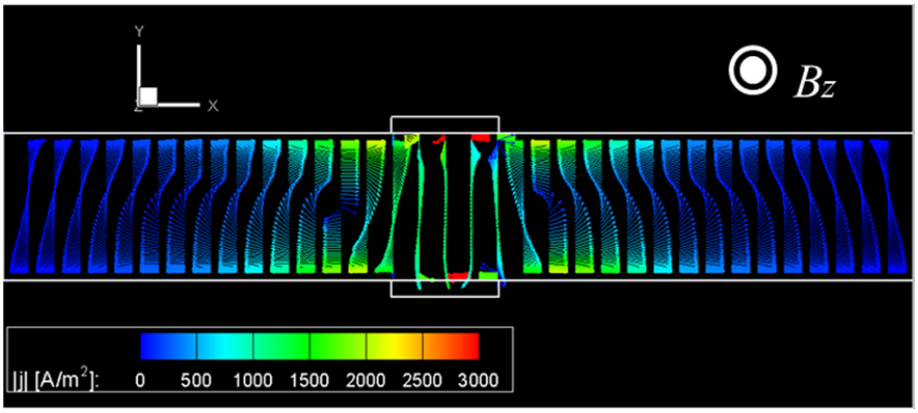

(a) Electric current density vector

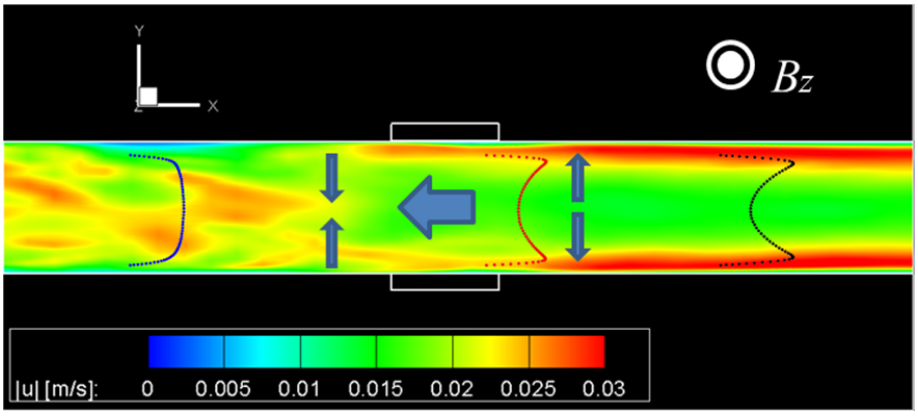

(b) Velocity

Fig. 3.3 Instantaneous distributions of the electric current density vector and the velocity in the *x*-*y* plane (z = 0.04 m).

The two eddy currents generate an additional Lorentz force towards the y direction which is added to the strongest one that acts against the flow in the $-x$ direction, as shown in Fig. 3.3 (b) with five superimposed arrows. The global Lorentz force compresses the flow upstream and expands it downstream. As a result, M-shaped velocity profiles emerge in the plane perpendicular to the magnetic field. The mean velocity profiles in the y direction are shown for three x locations in Fig. 3.3 (b). In other words, the liquid metal seems to flow as if bypassing the so-called "magnetic obstacle" produced by the Lorentz force and behave like a flow around a cylinder, as observed in Refs. [70][71].

3.3.2 Electrical Efficiency and Mean Velocity Profiles

For the LMMHD generator at present conditions, an input power of 1.61×10^{-2} W, output power of 0.7×10^{-2} W, and the electrical efficiency of 43.6% are typical values for NaK. The quite small output power is attributed to a slow mean velocity of 0.06 m/s that is about 100 times slower than that in the Ref. [17], as well as a small cross section area, a short electrode length, a low magnetic flux density, and a finite σ_e. Although the output power could be small unrealistically, the argument about the electrical efficiency can be valid widely. Judging from Eq. (3.15), a higher electrical efficiency can be expected by reducing the conductivity ratio between liquid metal and the electrodes, suppressing the electrical loss due to eddy current, and enlarging the interaction parameter simultaneously. For instance, to replace the copper electrodes by a much better electrical conductive material (such as silver) is a proper approach. Inserting a board (vane) in the middle of duct to cut the influence of eddy current was reported as another method [29]. Additionally, increasing the applied magnetic flux density can improve the interaction parameter that a better electrical efficiency should be attainable.

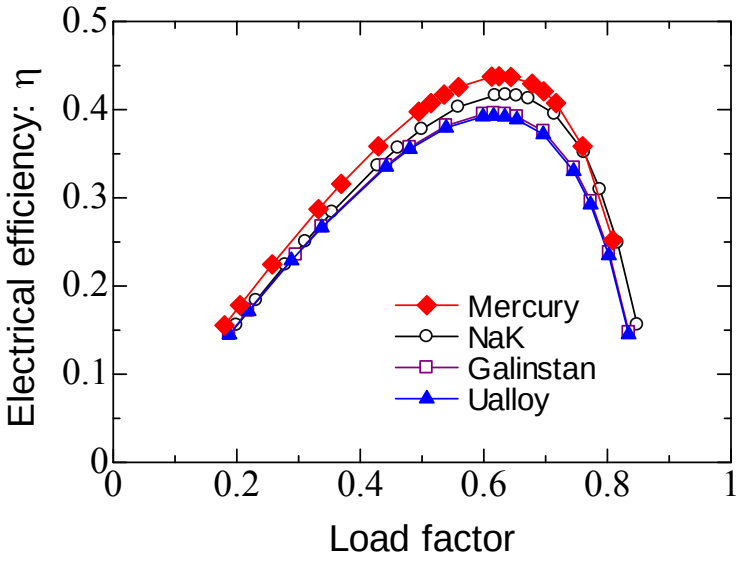

Fig. 3.4 Dependence of electrical efficiency on load factor.

First, the electrical efficiency under the same conditions of Reynolds number and maximum magnetic flux density for the four liquid metals is discussed. Figure 3.4 shows the electrical efficiency as a function of the load factor. It can be seen that the electrical efficiency reaches a peak when the load factor gets to about 0.64 for all four fluids. Efficiency is highest for mercury, then NaK followed by Galinstan and Ualloy. Under the present conditions, the ratios for the interaction parameter N are NaK/Galinstan/Ualloy/Mercury = 5.5/1.4/1.3/1. From Eq. (3.15) it is not surprise that NaK outperforms Galinstan and Ualloy, since NaK has a much higher interaction parameter which produces the greatest reduction in the loss due to wall friction (the third term in Eq. (3.15)). Meanwhile, the performances of Galinstan and Ualloy are similar due to their similar physical properties (refer to Table 3.1), which result in close interaction parameters. In spite of having the lowest interaction parameter, mercury attains the highest

electrical efficiency, even much higher than NaK. Therefore, there must be another factor that determines the electrical efficiency.

Figure 3.5 shows the mean velocity profiles at the downstream edge of the electrodes (x = 0.33 m) (a) in the y direction (z = 0.04 m) and (b) in the z direction (y = 0.04 m). The superscript "+" indicates wall units; u^+ is normalized by wall friction velocity $u_\tau = (\tau_w/\rho)^{1/2}$ where τ_w is the shear stress of the wall, y^+ is $2y\mathrm{Re}_\tau/L$, z^+ is $2z\mathrm{Re}_\tau/L$.

In Fig. 3.5(a), the central velocity reduction by the Lorentz force enhances the velocity near the side walls because the mass flow rate is conserved for incompressible flows. As a result, the velocity profile looks like an M-shaped wall jet flow.

In Fig. 3.5(b), the profiles of the so-called Hartmann flow can be seen in the downstream power generation region. In the z direction, the electric current flows in the $-y$ direction around the center, so that the Lorentz force decelerates the flow. In contrast, the electric current flows in the opposite direction near the walls, such that the Lorentz force accelerates the flow. This is the flattening effect of the Lorentz force which creates the Hartmann flows. The sidewall layer width of the M-shaped profiles and the width of the Hartmann layers are inversely proportional to the square root of Hartmann number ($Ha = \sqrt{N\,\mathrm{Re}}$) and the Hartmann number, respectively. Mercury has the thickest boundary layer of the four fluids as shown in Fig. 3.5. Thus, the largest wall friction loss occurs for mercury. However, the electrical efficiency of mercury is the highest. In the present case, the electrical efficiency cannot be explained being due only to the influence of the boundary layers discussed above.

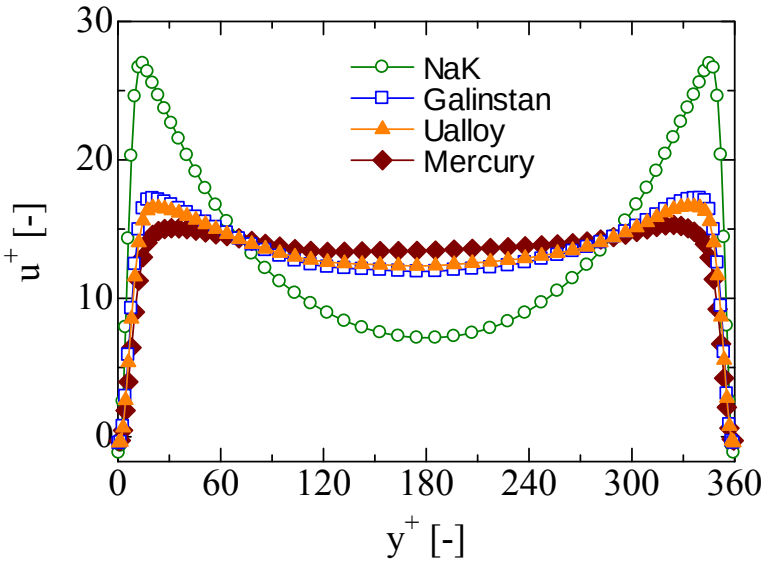

(a) Mean velocity in y direction (x = 0.33m, z = 0.04m).

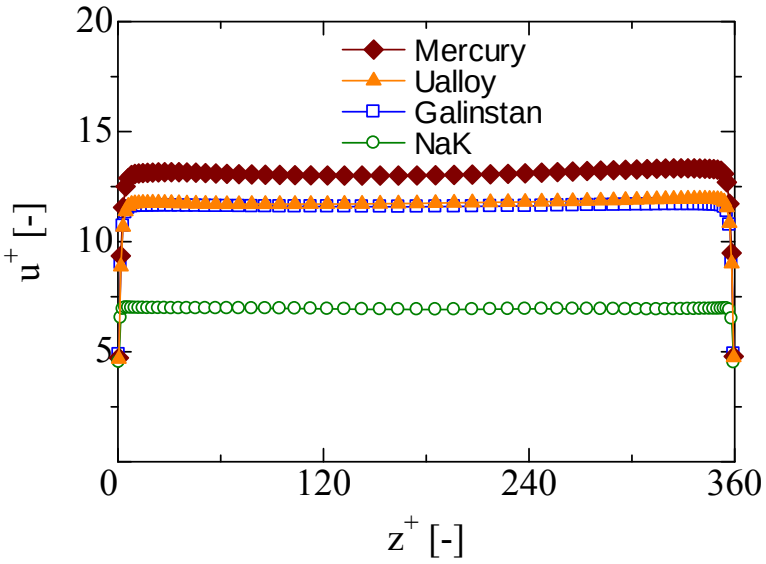

(b) Mean velocity in z direction (x = 0.33m, y = 0.04m).

Fig. 3.5 Profiles of mean velocity u^+ in y and z directions under same copper electrodes but different interaction parameters.

3.3.3 Influence of Interaction Parameter

In order to investigate the relationship between the interaction parameter and M-shaped profiles further, the maximum magnetic flux density for all four fluids is changed to produce the same interaction parameter under the same Reynolds number (see Eq. (3.14)), that is, for Galinstan $B = 0.219$ T, for Ualloy $B = 0.233$ T and for mercury $B = 0.262$ T, while the flux density for NaK was kept at 0.120 T as it was before.

Figure 3.6 illustrates the M-shaped mean stream-wise velocity profiles, which clearly look similar to those of NaK shown in Fig. 3.5 (a). The velocity profiles of Galinstan, Ualloy and mercury are consistent with the magnitude of the interaction parameter and nearly coincide with each other. This suggests a strong influence of the interaction parameter on the shape of the mean velocity profile, including the boundary layers.

Table 3.2 Electrical efficiency under same interaction parameter.

	NaK	Galinstan	Ualloy	Mercury
η	0.430	0.372	0.372	0.482

However, as shown in Table 3.2, the electrical efficiency is still different for the four fluids. The efficiency of mercury (0.482) exceeds that of NaK (0.430), while Galinstan and Ualloy both have a much lower efficiency of 0.372. Thus, the electrical efficiency cannot be adequately explained using only the interaction parameter.

The clue to solving this discrepancy is that the electrical efficiencies of Galinstan and Ualloy, which have the same electrical conductivity, are the same. Mercury's electrical conductivity is much smaller than those of the other three metals but it produces the best performance.

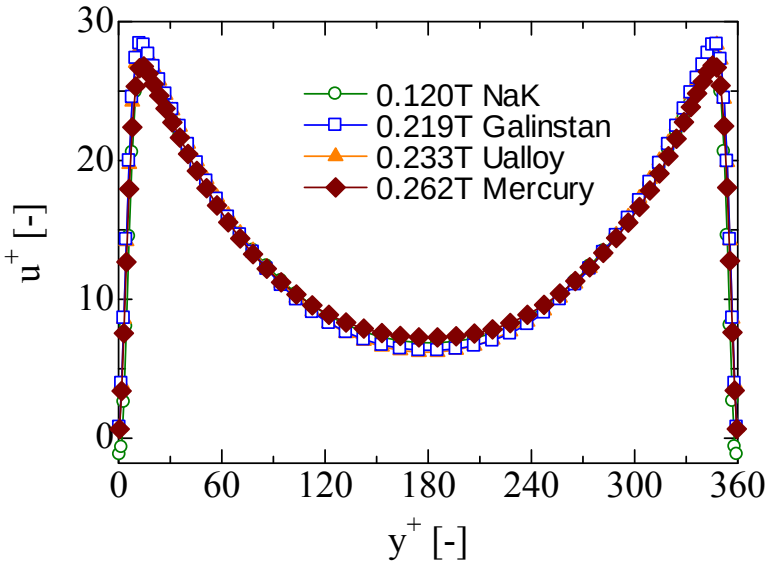

(a) Mean velocity in y direction (x = 0.33m, z = 0.04m).

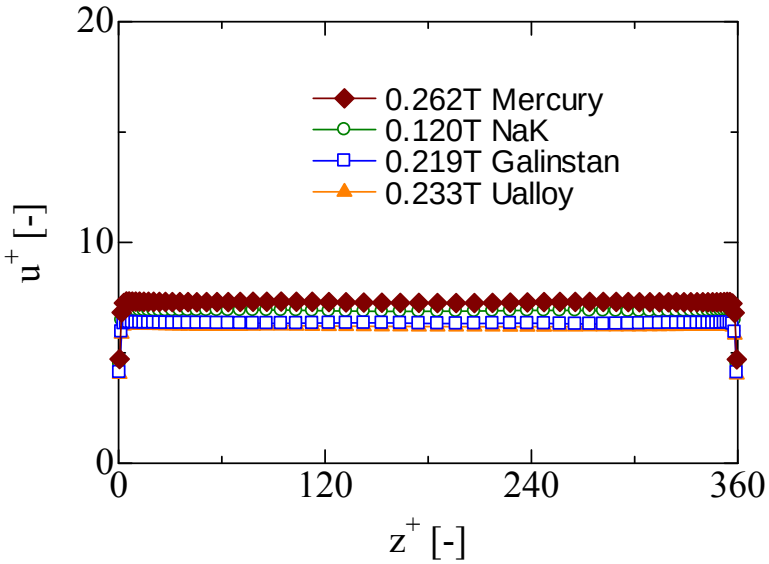

(b) Mean velocity in z direction (x = 0.33m, y = 0.04m).

Fig. 3.6 Profiles of mean velocity u^+ in y and z directions under same copper electrodes and same interaction parameters.

It is reasonable to infer that electric current easily flows from the working fluid to the load through the electrodes when the working fluid has a lower conductivity than the electrodes, which possess high but finite electrical conductivity. Since copper (of finite electrical

conductivity) is used for the electrodes here, the electrical efficiency has been examined for different ratios of the electrical conductivity between the fluid and the electrodes, although the same interaction parameter was given.

3.3.4 Influence of Electrodes

In the previous section it was shown that, although the same interaction parameter gave similar mean velocity profiles for all four working fluids, the electrical efficiencies still differed. This difference can be attributed to the ratio of electrical conductivity between a liquid metal and the electrodes. Thus, the responsible factor is the Joule heating loss in the electrodes shown in Eq. (3.15). If the electrical conductivity of the electrode were infinite, the impact of that term would be eliminated. In that case, the electrical efficiency has to be the same value for the same interaction parameter and Reynolds number.

To verify the influence of the finite electrical conductivity of the electrodes on the electrical efficiency, the electrical conductivity of the electrodes is changed hypothetically. Thus, the artificial conductivities are considered as $\sigma_{e\text{-}a}$ of 2.95×10^{7} S/m, 1.18×10^{8} S/m, 5.90×10^{8} S/m, 5.90×10^{9} S/m, and 5.90×10^{10} S/m, which are half, twice, 10 times, 100 times, and 1000 times larger than the real conductivity of copper ($\sigma_{Cu} = 5.90\times10^{7}$ S/m). Here, other conditions are kept the same as those of Section 3.3.2. Namely, $B = 0.12$ T is applied for all fluids, and the interaction parameter for each fluid is restored to its original value.

Figure 3.7 shows that as the conductivity of the electrodes increases, the electrical efficiency improves gradually for all four fluids. However, the superiority of mercury, whose conductivity is the lowest of the four fluids, diminishes. Thus, these results indicate the electrical efficiency is reduced for small $\sigma_{e\text{-}a}$ / σ_{Cu}, especially less than 10 and a relatively lower

conductive liquid metal ensures better electrical efficiency for electrode with a finite conductivity, such as the copper electrode here.

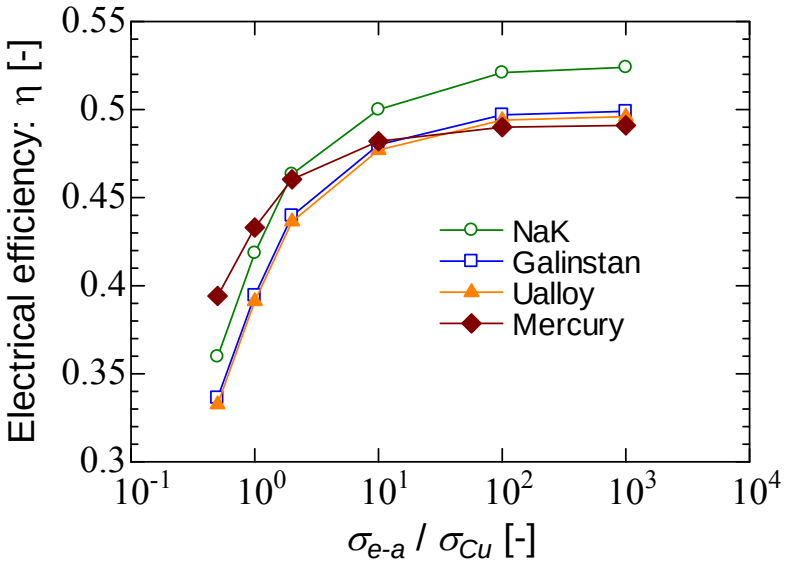

Fig. 3.7 Electrical efficiency against a ratio of conductivity of an artificial electrode $\sigma_{e\text{-}a}$ to that of copper σ_{Cu}.

Finally, the mean velocity profiles and electrical efficiency with constant interaction parameter are examined for an artificial electrode, where the conductivity of the electrodes was chosen to keep σ_f/σ_e the same for all fluids. This means that $\sigma_{e\text{-}a} = 2.49\times10^7$ S/m is used for Mercury and $\sigma_{e\text{-}a} = 5.52\times10^7$ S/m is used for Galinstan and Ualloy. In addition, the conductivity of load resistance σ_R was modified to get the same load factor, which should be the value near at 0.64 as already discussed above. Thus, $\sigma_R = 9.00\times10^5$ S/m is set for NaK, $\sigma_R = 3.56\times10^5$ S/m for mercury, and $\sigma_R = 7.90\times10^5$ S/m for Galinstan and Ualloy. Consequently, the same value of the ratio σ_f/σ_R for four liquid metals is aligned.

Figure 3.8 shows better agreement between profiles than Fig. 3.6. Moreover, it is confirmed that the electrical efficiency for different fluids under different magnetic flux densities

reaches almost the same value of 0.43, shown in Table 3.3. Note that the electrical efficiency of 0.43 is not the best performance of an LMNHD generator; it is merely the electrical efficiency obtained under the present working conditions. A higher electrical efficiency will be achieved for conditions of (*i*) high Reynolds number and high interaction parameter to reduce the wall friction loss, (*ii*) a liquid metal with a relatively low electrical conductivity for decreasing σ_f/σ_e and (*iii*) an optimal load factor.

Table 3.3 Electrical efficiency at same σ_f/σ_e, σ_f/σ_R and interaction parameter.

	NaK	Galinstan	Ualloy	Mercury
η	0.430	0.429	0.429	0.429

So far the influence of the MHD flows including laminar and turbulent flows on the generator performance has been investigated by means of the LES. A quantitative evaluation under the different turbulent models, and the validation based on the experimental observation are considered as the important future issues.

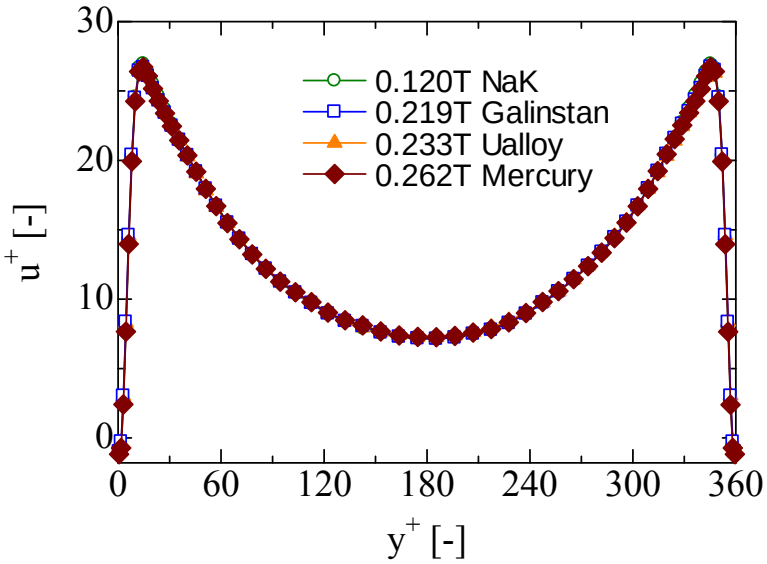

(a) Mean velocity in y direction (x = 0.33m, z = 0.04m).

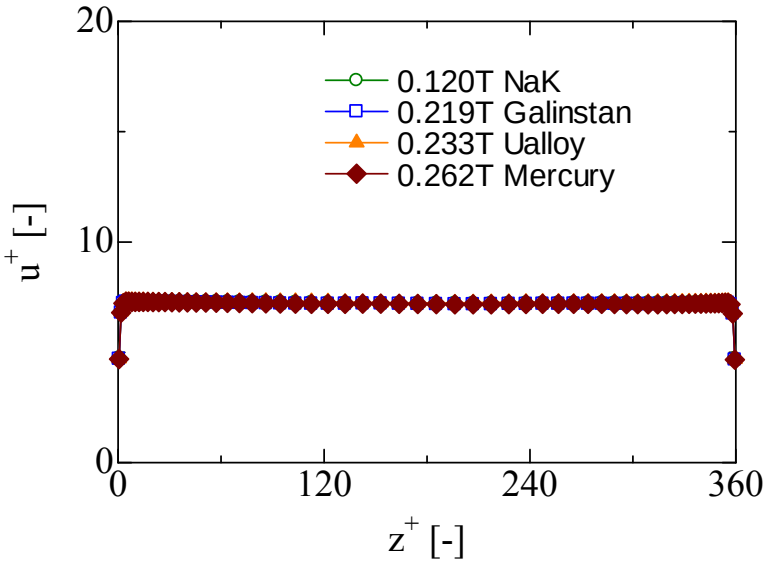

(b) Mean velocity in z direction (x = 0.33m, y = 0.04m).

Fig. 3.8 Profiles of mean velocity u^+ in y and z directions with same σ_f/σ_e, σ_f/σ_R and same interaction parameters.

3.4 Summary

The influence of working fluid characteristics on the performance of an LMMHD generator has been investigated numerically for fixed flow conditions. The fluid characteristic, that is the mean velocity profile, is determined by the interaction parameter when Re, B and σ_e are fixed. However, the electrical efficiency differs even with the same interaction parameter owing to the finite conductivity of the electrodes. This discrepancy will be eliminated if the ratio of the electrical conductivities of the liquid metal and the electrode is fixed. As a result, in real situations in which electrodes have finite electrical conductivity, working conditions with a large interaction parameter and a liquid metal with a relatively low electrical conductivity for decreasing σ_f / σ_e are expected to provide better performance.

Until now, the influence of the electrical conductivity of electrodes, which may include lead wires, on the electrical performance of an LMMHD generator has never been considered, as far as I know. It has been found in this study that the finite electrical conductivity affects not only the electrical efficiency, but also the choice of working fluid. This is one of the novel aspects of the present work.

The similarities of both fluid phenomena and electrical performance among different fluids have been revealed by using a large eddy simulation, which is an unsteady three-dimensional numerical simulation including turbulence and distributions of the electric potential in electrodes, to obtain more realistic and reliable estimations of performance than those not taking account of turbulent models and finite electrical conductivity of electrodes. The present findings should be useful for material selection and design optimization in the research and development of LMMHD power generators.

Chapter 4 - **Turbulent Phenomena in a Liquid Metal MHD Flows**

In this chapter, the influence of various load conditions (open-circuit, short-circuit, and externally applied current source (hereafter called “pump” condition for short)) as well as non-uniform magnetic flux densities on the turbulent phenomena in an LMMHD flows are observed and discussed.

In Section 4.1, a brief introduction and main objectives are described. Section 4.2 expresses the governing equations and numerical methods. In Section 4.3, numerical results among three types of load conditions are mainly discussed. In Section 4.4, a summary and the conclusions are drawn.

4.1 Introduction and objectives

Liquid metal magnetohydrodynamic (MHD) turbulent flows are of great importance for applications of MHD power generation and MHD accelerators (pumps). Researches in hope of understanding the MHD influences on the turbulence have lasted for decades [72].

As early as the World War II, Hartmann theoretically studied the MHD laminar channel flow in a homogeneous magnetic field [24]. After that, a couple of experiments in various aspect ratios of rectangular duct and different Reynolds numbers were conducted to reveal the MHD effects as well as the suppression of turbulence [31] ~ [33]. For instance, Brouillette and Lykoudis examined the MHD turbulent flows in a rectangular duct (at aspect ratio of 5:1) with insulated walls and illustrated that a laminarization occurs under a uniform and strong magnetic field [31].

However, as mentioned in chapter 1, the measurement of an opaque liquid metal (even poisonous in some cases) is complicate work. Besides, the size (length scale) of the probe (for measuring) restricts its accuracy for measurements of small scale turbulence. The development

of Computational Fluid Dynamics (CFD) has offered considerable approaches. In hope of revealing the effect of a magnetic field on turbulent flows, researches through DNS, RANS modeling, and LES are conducted worldwide.

Recently, H. Kobayashi *et al.* carried out the LES to examine the turbulence structures and the transition of sidewall jets in the optimal load condition of an LMMHD generator with non-uniform transverse magnetic field at constant Reynolds number [48]. It shows that the Lorentz force would decelerate the flow and suppress the turbulence simultaneously. However, owing to the eddy currents produced by the gradient of magnetic flux density in the stream-wise direction, an M-shape velocity profile appears and for high magnetic flux density, moreover the turbulent transition is promoted again in the downstream region.

Since various load conditions change the distribution of electrical potential and current, phenomena on fluid dynamics such as velocity and turbulent vortices are predicted to vary correspondingly. In this chapter, the turbulent phenomena in liquid metal MHD flows under three extreme load conditions that the open-circuit, the short-circuit, and the pump which is a case by adding externally applied current opposite to the power generation case, are going to be examined. Three strength incremented non-uniform magnetic flux densities are applied successively, and the influences of various load conditions and magnetic flux densities on the velocity profile and three dimensional turbulence structures are assessed. To illustrate the critical problem more clearly, fully developed turbulent flows, which are introduced into the duct in a constant flow rate, are produced in advance. Three-dimensional MHD flows are examined by means of LES with the coherent structure Smagorinsky model (CSM), which can provide more realistic estimations of unsteady turbulent phenomena than RANS.

4.2 Numerical conditions

4.2.1 Computational Domain

To illustrate the influence of MHD effects more clearly, fully developed turbulent flows should be introduced into the duct before flowing through the magnetic region in advance. Accordingly, the computational domain is divided into two parts, a main region and a driver region as shown in Fig. 4.1. The driver region serves as a general duct (no magnetic flux density apply) for circularly producing fully developed turbulence, while a liquid metal MHD duct with two opposing electrodes is located in the main region. It is same to chapter 3 (refer to Fig. 3.1). A load resistance connected at the center (in the *x*-*z* plane) of the opposing electrodes by the lead cables shows the typical image of an MHD power generation. However, the resistance can be replaced by an ideal switch to realize short (with resistance of 0.31 nΩ in computation) and open circuits, or by an external current source to achieve the pump condition. In all cases liquid metal flows toward the +*x* (stream-wise) direction, where a constant Reynolds number (Re_τ = 180) based on friction velocity is used.

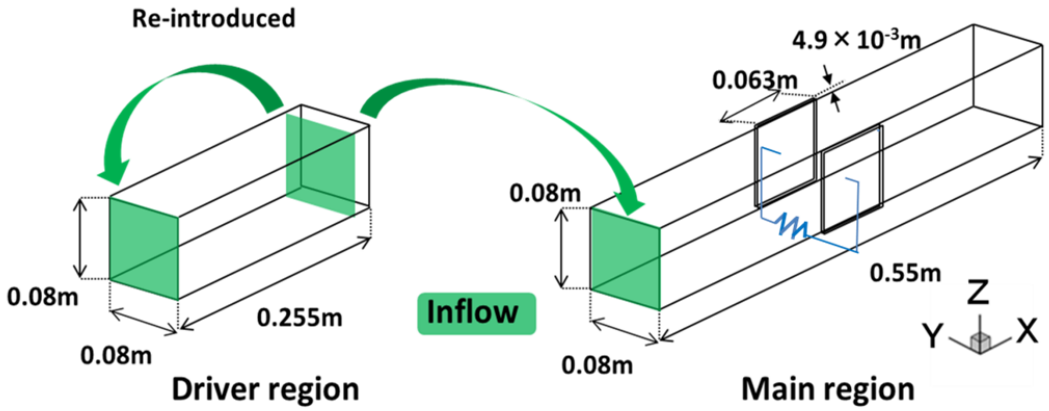

Fig. 4.1 Schematic view of the computational domain.

For the main region, the length L_x of the duct in the stream-wise direction is 0.55 m with same width and height at $L_y = L_z = 0.08$ m. An equally spaced grid is used in the x direction ($\Delta x = 1.5\times10^{-2}$ m), while a stretched grid is adopted in the y and z directions (Δy, $\Delta z = 2.48\times10^{-4} \sim 2.41\times10^{-3}$ m). The numbers of grid points are 36, 64 and 64 for x, y and z directions, respectively. In this resolution, it is confirmed that the mean velocity profile agree well with an experimental result [48]. The region between the electrodes ($x/L_x = -0.12 \sim 0.12$ m) is called the electrodes area in this chapter. The electrodes have dimensions of 6.3×10^{-2} m, 4.87×10^{-3} m and 8×10^{-2} m in x, y and z directions, respectively. Here a finite conductivity of copper (5.90×10^{7} S/m) is adopted for the pump condition, while an insulated wall (0 S/m) and a hypothesis conductivity (5.90×10^{10} S/m) are supposed for the open and short circuit conditions, respectively. The rest of the walls are set to be insulated.

4.2.2 Non-uniform Magnetic flux densities

An external non-uniform magnetic field is induced in the $+z$ or vertical direction as shown in Fig. 4.2, with no distribution in the x and y directions. The maximum magnetic flux density B_{z0} is changed among 0.03 T, 0.12 T, and 0.24 T in the electrodes region, whereas the value in both the inlet and outlet regions is decayed to zero to avoid any influence on the boundary conditions. It is a symmetrical distribution and the right half profile for $x > 0$ is described by Eq. (4.1). Considering the eddy current influence from the non-uniform distribution, the present magnetic field is not the best one. An ideal magnetic field is supposed to be uniform in distribution which will eliminate the end losses caused by eddy current. However, to make a uniform magnetic field is next to impossible in reality. It had found that an exponential distribution with long magnetic field extension can raise the performance [29].

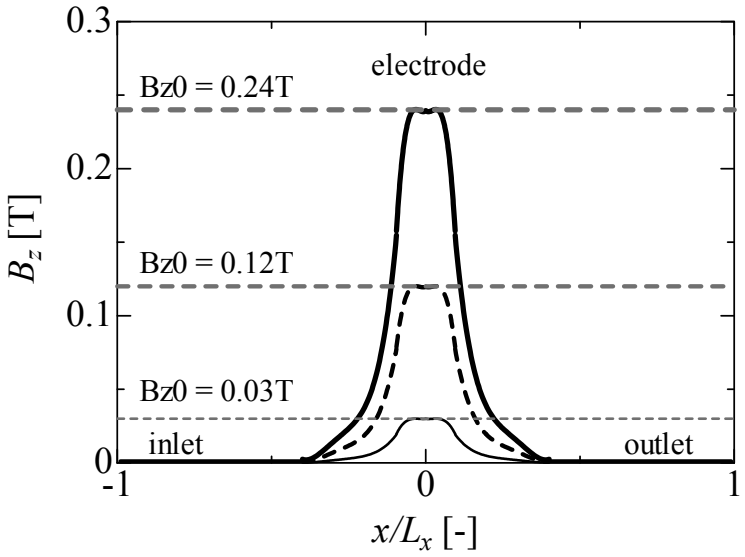

Fig. 4.2 Externally applied magnetic flux density.

$$
\begin{aligned}
B_z &= B_{z0}[1 - 0.72\frac{x}{L_x} + 54.53(\frac{x}{L_x})^2 - 891.56(\frac{x}{L_x})^3], \\
&\qquad (0 < \frac{x}{L_x} < 0.095) \\
&= B_{z0}[2.35 - 28.77\frac{x}{L_x} + 142.4(\frac{x}{L_x})^2 - 320.78(\frac{x}{L_x})^3 + 270.21(\frac{x}{L_x})^4], \\
&\qquad (0.095 < \frac{x}{L_x} < 0.4) \\
&= 0 \\
&\qquad (\frac{x}{L_x} > 0.4)
\end{aligned}
\tag{4.1}
$$

4.2.3 Governing Equations and Numerical Methods

The governing equations and numerical methods are almost same to those in chapter 3, except that for the driver region, where the general incompressible Navier–Stokes equations without the influence of Lorentz force are used.

To focus on the transition of turbulent phenomena, the liquid metal of Ualloy is selected, in consistence with the previous studies [48] for comparing, as well as for saving calculation cost (much shorter to reach stable state than NaK). The time step is set to $\Delta t = 1.00\times10^{-3}$ s, and time steps of 5.2×10^{6}, 3.2×10^{6}, 2.2×10^{6} for 0.03 T, 0.12 T, 0.24 T are cost to obtain the statistics of turbulent flows, respectively.

4.3 Results and discussion

4.3.1 Non-MHD turbulent flows

At the very beginning, fully developed Non-MHD turbulent flows generated by the driver region are verified by removing the externally applied magnetic flux density (B_{z0} = 0 T) at the main region. The phenomena can be the criteria of judgment for the various MHD turbulent flows with different load conditions followed up.

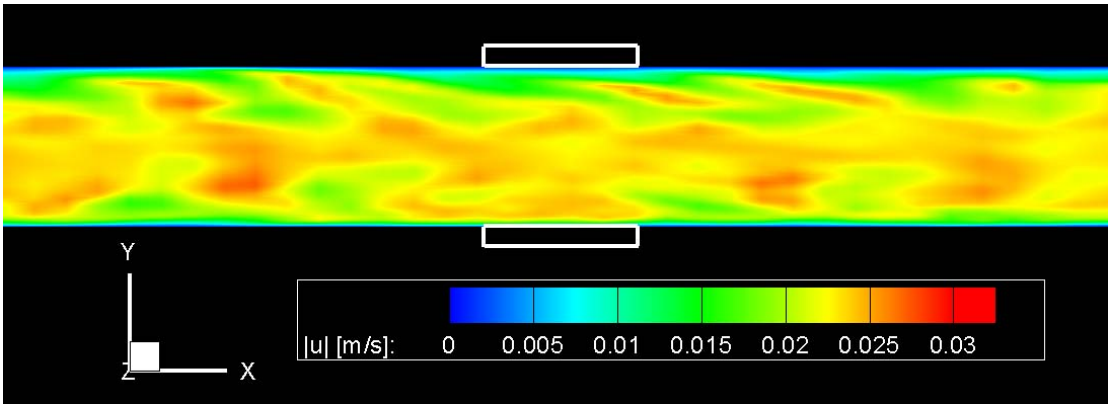

Fig. 4.3 Instantaneous distribution of the velocity in the central *x*-*y* plane without externally applied magnetic flux density.

Figure 4.3 shows the instantaneous distribution of the velocity in the central *x*-*y* plane (z/L_z = 0.5) of the main region. The two white rectangle boxes in the middle represent the electrodes. The orientation axis and the contour legend are shown in the below.

The displayed velocity is calculated by

$$|u| = \sqrt{|u_x|^2 + |u_y|^2 + |u_z|^2} \tag{4.2}$$

where the strengths are illustrated by the multi-coloring details of contour legend in Fig. 4.3. Since no magnetic flux density is applied, the overall flow sees no apparent change from the upstream to the downstream.

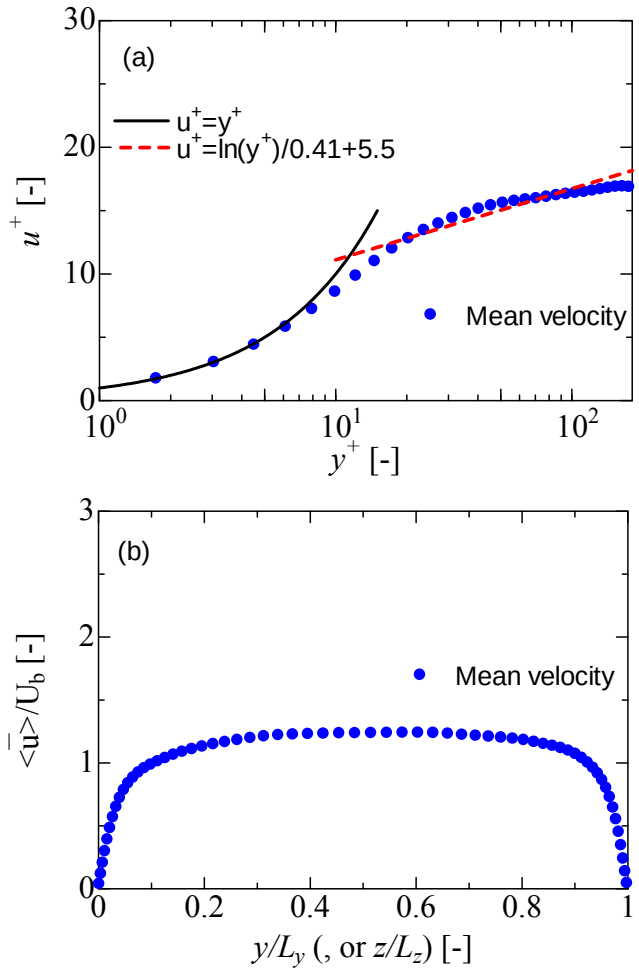

Fig. 4.4 Distributions of the mean velocity at $x/L_x = 0$ without externally applied magnetic flux density.

To analyze the quantified average distribution, the mean velocity is examined with much more details. Figure 4.4 describes the distributions of mean velocity calculated by ensemble average at the $x/L_x = 0$, where is the middle region of the duct.

Figure 4.4(a) uses a logarithmic scale to verify the mean velocity profile from the log law. The velocity and the length scales are normalized by the friction velocity and the viscous lengths.

$$u_\tau = \sqrt{\frac{\tau_\omega}{\rho}}, \qquad u^+ = \frac{\bar{u}}{u_\tau}, \tag{4.3}$$

$$y^+ = \frac{u_\tau y}{\nu}. \tag{4.4}$$

where τ_ω is the wall shear stress and ρ is the density of liquid metal. The distance (y^+) from the wall measured in viscous lengths is same to the friction Reynolds number. Thus, the rightmost point is $y^+ = \mathrm{Re}_\tau$. Since the distribution is symmetrical, only half of it is shown.

Figure 4.4(a) clearly shows the viscous sub-layer ($y^+ < 5$) of a linear relation $u^+ = y^+$. And the log layer ($y^+ > 30$) comply with the log law of $u^+ = \ln(y^+)/0.41 + 5.5$. The region between the viscous sub-layer and the log layer is the transition region, or the so called buffer layer ($5 < y^+ < 30$). As a result, the mean velocity profile conforms to a general uncompressible duct flow. Figure 4.4(b) illustrates the same mean velocity profiles in conventional Coordinates normalized by the bulk (averaged) velocity U_b and the duct width L. The symmetrical distributions are only drawn in the y direction, while almost same in the z direction. This distribution is much more intuitive, and will be referred frequently in other conditions below.

Figure 4.5 illustrates the overall isosurfaces of the second invariant $Q = 0.04$ normalized by the magnitude of a velocity gradient tensor (refer to Appendix E), where (b) is the top view of (a). Generally, the positive second invariant represents the eddy and $Q = 0.04$ is a convenient value for observation throughout this thesis.

This figure indicates that for a non-MHD flow, the stretched eddies in the stream-wise direction appear in the whole duct. It is a common phenomenon for one direction stream-wise flows and the change of these eddies will be used as a method to observe the turbulent transition later on.

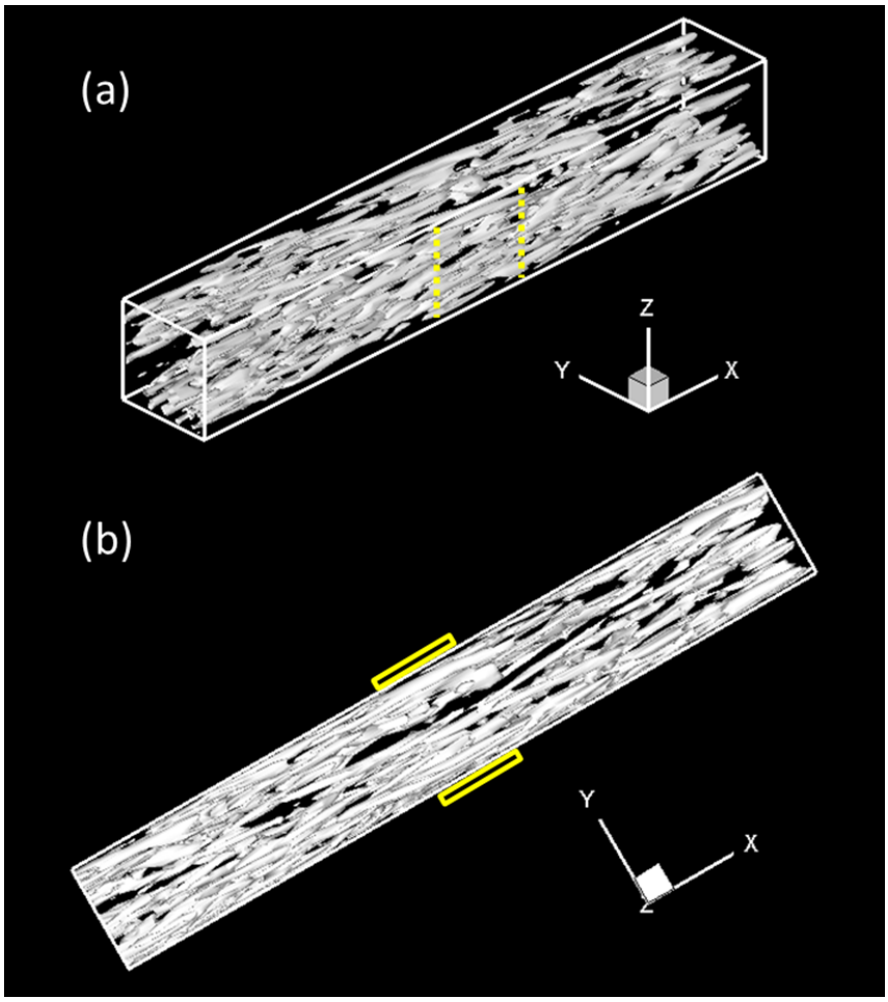

Fig. 4.5 Isosurfaces of the second invariant $Q = 0.04$ of the velocity gradient tensor without externally applied magnetic flux density.

4.3.2 Open circuit

In this section, the open circuit is considered, where the electrical conductivity of the electrodes is set to be 0, that is, the whole duct walls become insulated.

Figure 4.6 illustrates the distribution of the electric current density in the central plane (z/L_z = 0.5) at magnetic flux densities of (a) 0.03 T, (b) 0.12 T, and (c) 0.24 T. The arrow shows the direction, while the color represents the strength. The orientation axis and the contour legend to show the strength scale are placed at the bottom of the figure.

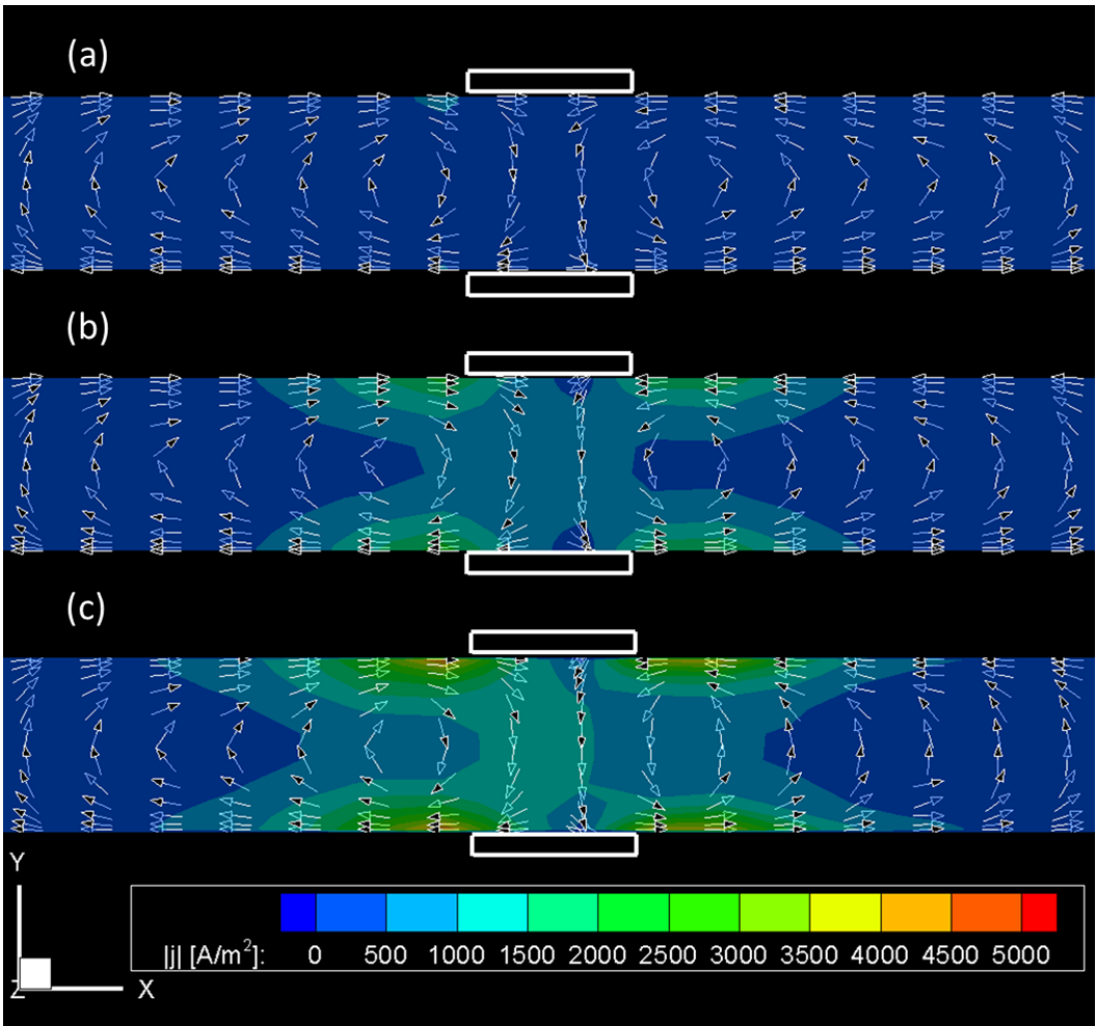

Fig. 4.6 Instantaneous distribution of the electric current density in the central *x*-*y* plane under open circuit at (a) B_{z0} = 0.03 T, (b) B_{z0} = 0.12 T, (c) B_{z0} = 0.24 T.

As similar to the distribution of velocity, the displayed electric current density is calculated

$$|j| = \sqrt{|j_x|^2 + |j_y|^2 + |j_z|^2} \tag{4.5}$$

It is shown in Fig. 4.6 that in each case of magnetic flux density, even though no electric current flows from anode to cathode, a pair of eddy currents exists in the upstream and downstream regions of the electrodes. Attributed to the gradient (refer to Fig. 4.2) of the magnetic flux density in the stream-wise direction, the eddy current flows clockwise upstream and anticlockwise downstream with obeying the Lenz law. This special distribution of eddy currents generates Lorentz force that compresses the flow upstream and expands it downstream in the y direction.

Figure 4.7 shows the instantaneous distribution of the Lorentz force in the central x-y plane (z/L_z = 0.5) under open circuit at (a) B_{z0} = 0.03 T, (b) B_{z0} = 0.12 T, (c) B_{z0} = 0.24 T. Similarly, the orientation axis and the contour legend to show the strength scale are placed at the bottom of the figure. The Lorentz force is calculated as follow.

$$|F| = \sqrt{|F_x|^2 + |F_y|^2 + |F_z|^2} \tag{4.6}$$

Under open circuit, the small electric current densities generate less Lorentz force, which is shown in Fig 4.7 that the Lorentz force are next to zero in both the upstream and downstream regions. Therefore, the relatively strong influence of eddy currents are shown in the middle region of Fig 4.7 (the electrodes region) at (b) B_{z0} = 0.12 T and (c) B_{z0} = 0.24 T.

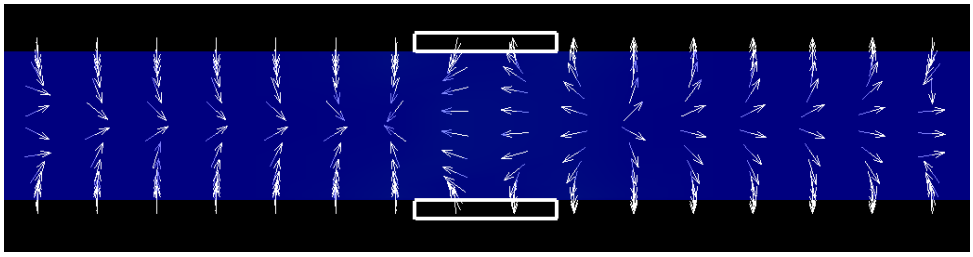

(a) B_{z0} = 0.03 T

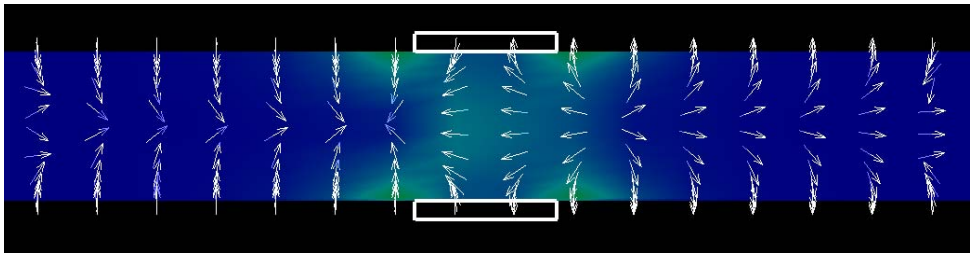

(b) B_{z0} = 0.12 T

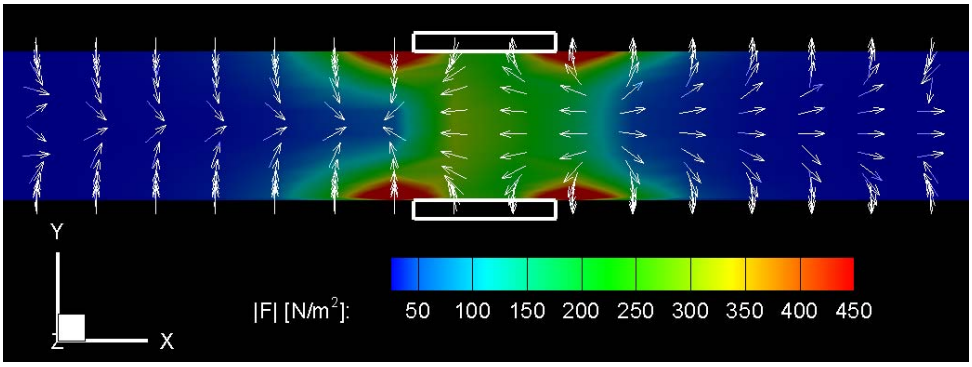

(c) B_{z0} = 0.24 T

Fig. 4.7 Instantaneous distribution of the Lorentz force in the central *x*-*y* plane under open circuit at (a) B_{z0} = 0.03 T, (b) B_{z0} = 0.12 T, (c) B_{z0} = 0.24 T.

Then the influence of the magnetic flux density on the MHD duct flows is discussed. Figure 4.8 presents the instantaneous distribution of the velocity in the central *x*-*y* plane under open circuit at (a) B_{z0} = 0.03 T, (b) B_{z0} = 0.12 T, (c) B_{z0} = 0.24 T. Judging by the color in Fig. 4.8(a), the velocity fluctuation is restrained in the downstream by the Lorentz force (compare with Fig. 4.3). In Fig. 4.8(b), the turbulent flow is relaminarized and an M-shaped velocity

distribution (retarded at the center of the channel and accelerated at the walls) is shown from the electrodes region to the downstream. When the magnetic flux density is increased further to 0.24 T, the M-shaped velocity profiles are strengthened and fluctuations appear in the sidewall layers eventually.

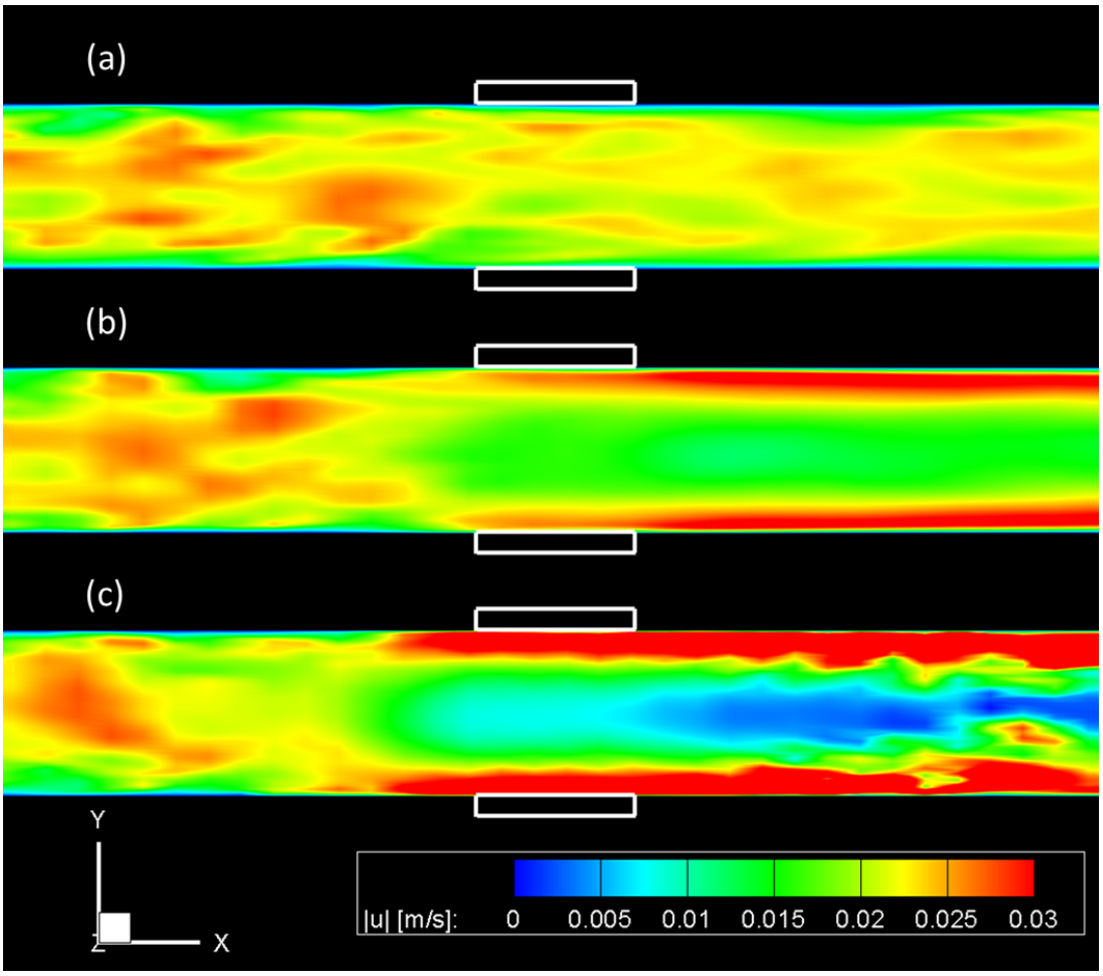

Fig. 4.8 Instantaneous distribution of the velocity in the central *x*-*y* plane under open circuit at (a) B_{z0} = 0.03 T, (b) B_{z0} = 0.12 T, (c) B_{z0} = 0.24 T.

Figure 4.9 shows the mean velocity profiles of three different magnetic flux densities along the (a) horizontal and (b) vertical bisectors at the middle position (x/L_x = 0) of the duct. All

of these velocities are calculated by 20000 steps of ensemble average and normalized by the bulk (averaged) velocity U_b.

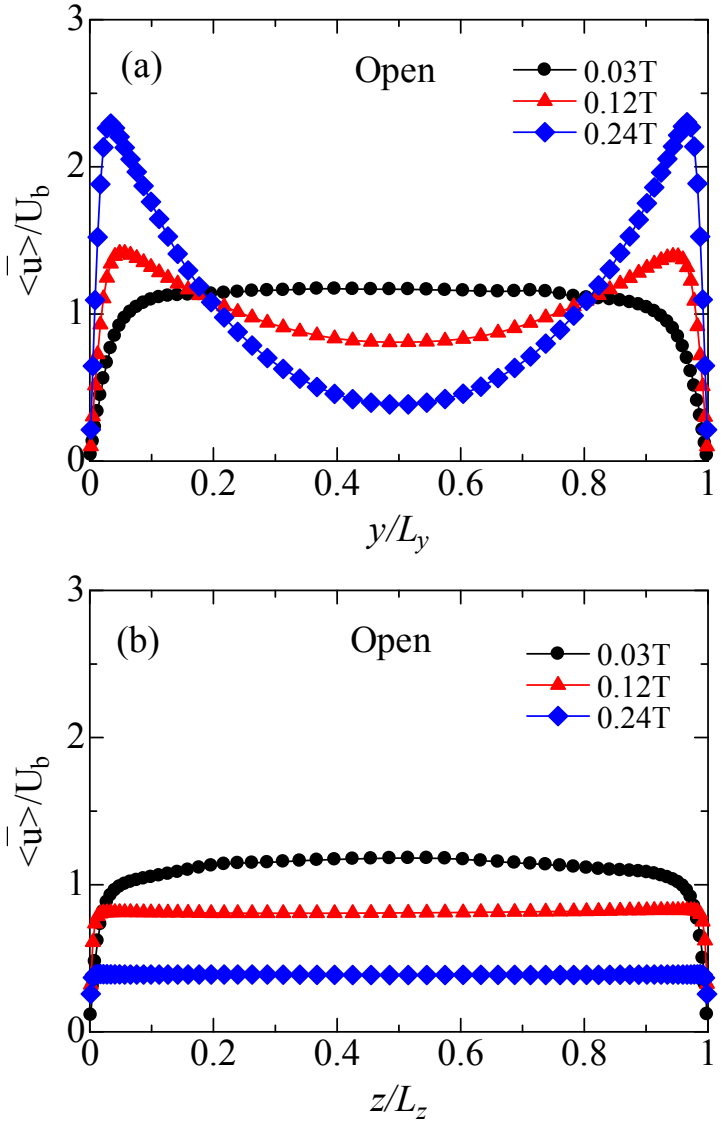

Fig. 4.9 Mean velocity of open circuit at x/L_x = 0 along the (a) horizontal y bisector and (b) vertical z bisector.

In Fig. 4.9(a), as the magnetic flux density increase from 0.03 T to 0.24 T, a reduction of mass flow rate appears at the center of duct flows, which meanwhile leads to an increase of the

mass flow rate in the sidewall layer. Thus, a so called M-shaped profile appears at 0.24 T eventually. In Fig. 4.9(b), the flattening profiles or the so called Hartmann flow, whose width of the layer is proportional to 1/Ha, are shown.

In general, the mean velocity profiles shown in Fig. 4.9 look familiar to the results observed at the power generation region (same to $x/L_x = 0$ here) for the optimum condition of power generation [48], where the average loading parameter is around 0.65, rather being close to unity of the open circuit condition.

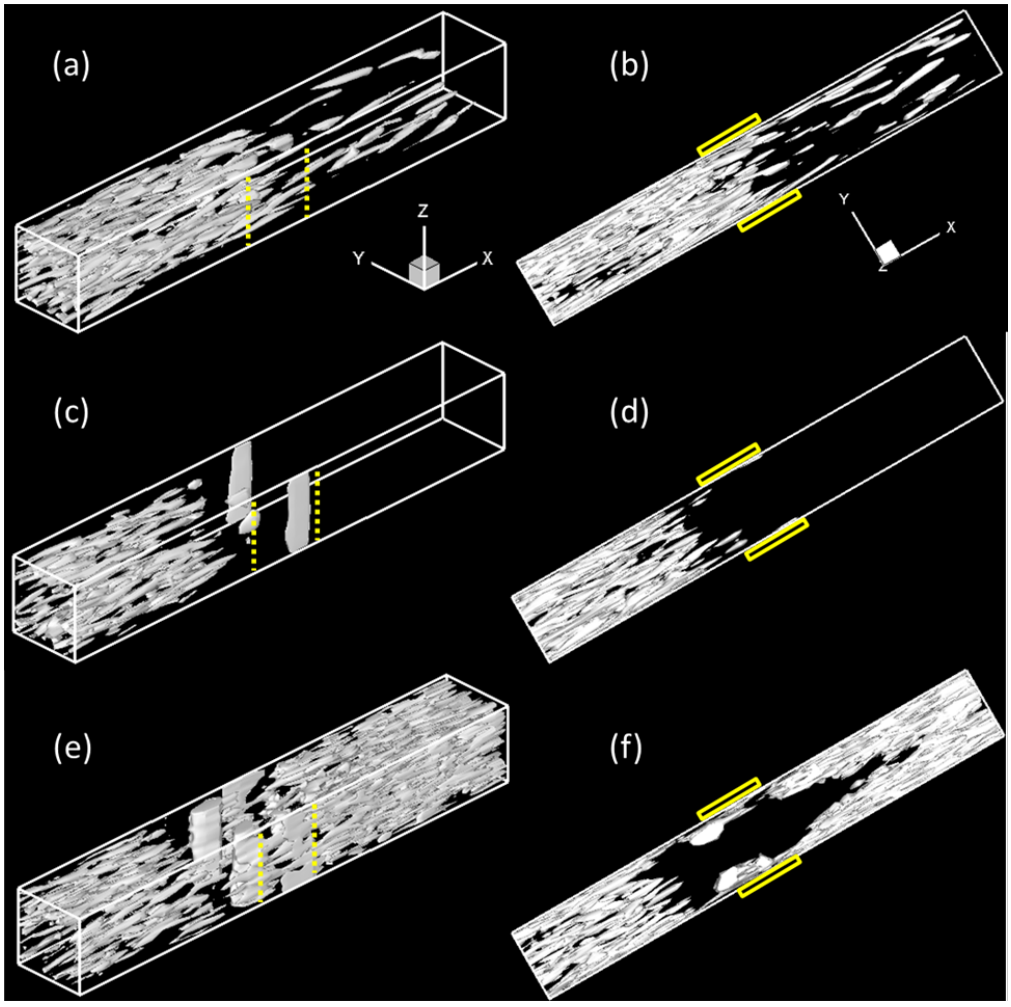

Fig. 4.10 Isosurfaces of the second invariant $Q = 0.04$ of the velocity gradient tensor under open circuit.

Figure 4.10 illustrates the overall isosurfaces of the second invariant Q = 0.04 of the velocity gradient tensor under (a, b) B_{z0} = 0.03T, (c, d) B_{z0} = 0.12T, and (e, f) B_{z0} = 0.24T, where (b), (d), (f) are the top view of (a), (c), (e) respectively. For all cases, similar stretched eddies in the stream-wise direction are observed in the inlet area, where little magnetic flux density is applied (refer to Figs. 4.2 and 4.5). As the magnetic flux density increase, eddies are curbed gradually. The mechanism of the curbing process is considered as follow. In general, the stretched eddy has a rotation axis parallel to the flow direction (x direction here) with four velocity fields around to form the vortex. When these stretched eddies enter the magnetic field, the damping effects of Lorentz force curb the velocity in all directions except the one parallel to the magnetic field. In the present research, the velocities in the y direction are suppressed that eliminates two velocity fields as well as the formation of the vortex. Consequently, the disappearance of stretched eddies can be observed. This assumption has been verified by probing the exact values around the eddy. For 0.03 T, much less eddies are observed while for B_{z0} = 0.12 T almost disappear in the downstream region. However, for B_{z0} = 0.24 T the sidewall jets promote recurrence of turbulence on the sidewalls in the downstream region. The reason is considered that the strong sidewall jets increasing the wall-shear stress in the sidewall layer contributes to the transformation of turbulence. To verify it quantitatively, the friction Reynolds numbers along the whole ducts (seven locations uniformity) are calculated.

Figure 4.11 illustrates the Reynolds number based on the friction velocity at seven locations (x/L_x = -0.88, -0.62, -0.12, 0, 0.12, 0.62, 0.88, which are uniformly distributed along the duct) under open-circuit for the three magnetic flux densities. The middle area (shown by the two green lines) shows the electrodes region. The value of Re_τ is defined by

$$\mathrm{Re}_\tau = \frac{u_{\tau w} L/2}{\nu}, \qquad u_{\tau w} = \sqrt{\nu \left| \frac{\partial \langle \bar{u} \rangle}{\partial y} \right|_{y=0}}. \tag{4.7}$$

The equation is same to Eq. (1.8) while $y = 0$ means the place nearest to the walls (adding the subscript w is to emphasize the place).

From Fig. 4.11, the abrupt increase of Reynolds number under $B_{z0} = 0.24$ T is clearly displayed, where the values are kept high (larger than 200) even in the downstream region. These data confirm the influences of the sidewall jets discussed above. Nevertheless, the Reynolds numbers decrease in the electrodes region for all the magnetic flux densities. It reflects the laminarization effects of Lorentz force under open circuit.

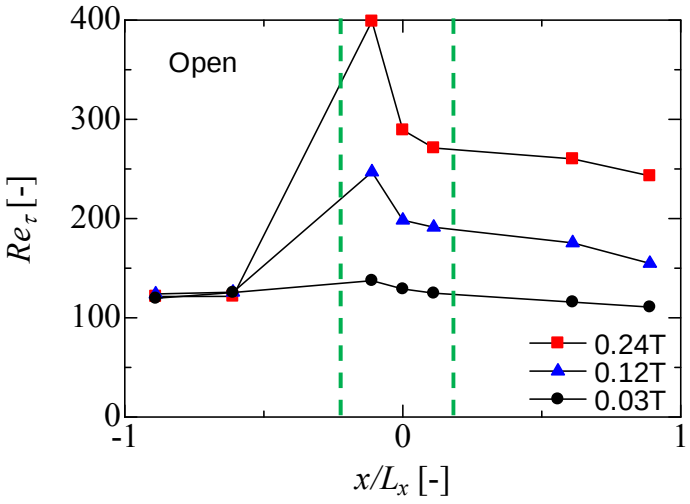

Fig. 4.11 Reynolds number based on the friction velocity at seven locations under open-circuit for three magnetic flux densities.

4.3.3 Short circuit

In this section, the short circuit is examined. The distributions of the electric current density in the central plane (z/L_z = 0.5) at (a) B_{z0} = 0.03 T, (b) B_{z0} = 0.12 T, (c) B_{z0} = 0.24 T are shown in Fig. 4.12. It can be seen from this figure that the high current density appears in the middle area, whereas current eddies still exists on both sides even though negligible to the short currents. Since the load circuit is shorted, the concentration of current is observed near and in the electrodes.

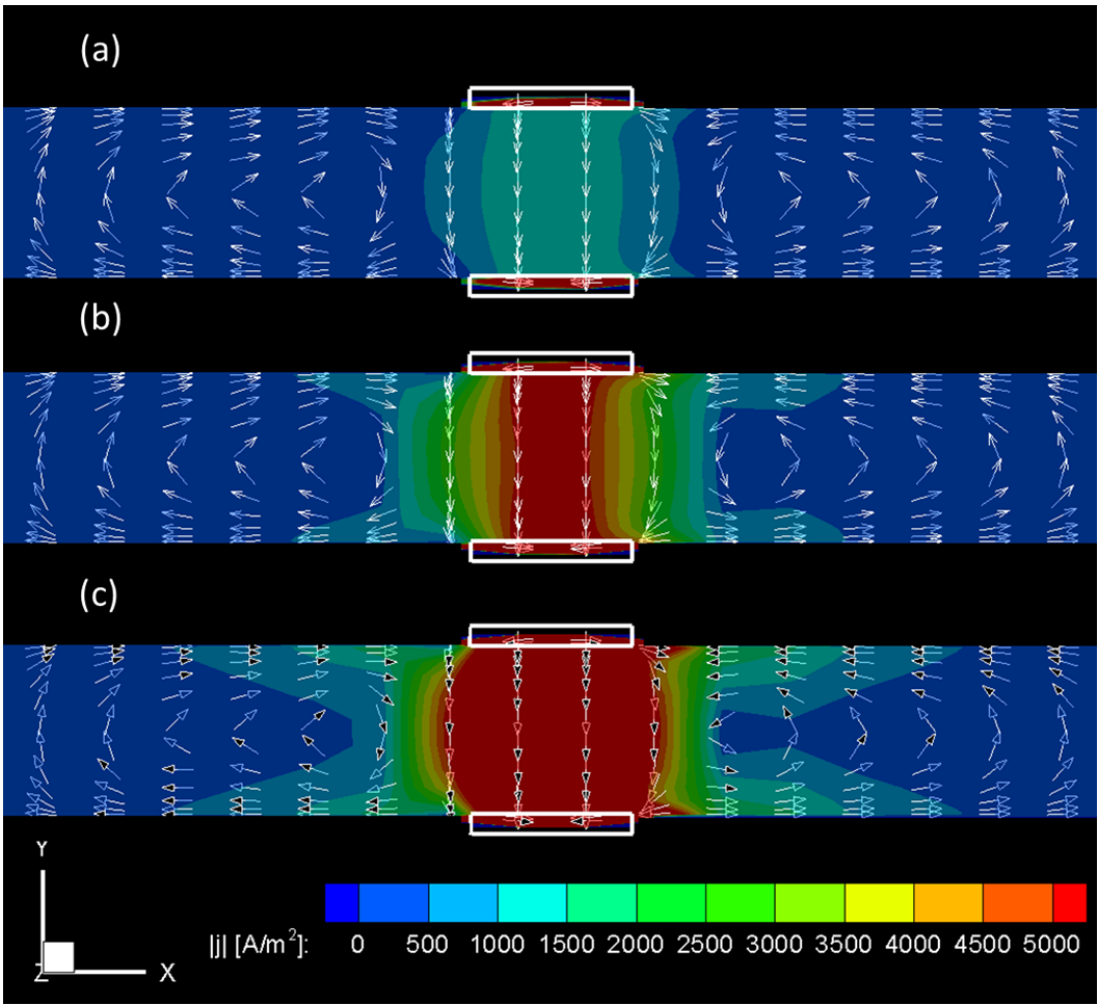

Fig. 4.12 Instantaneous distribution of the electric current density in the central *x*-*y* plane under short circuit at (a) B_{z0} = 0.03 T, (b) B_{z0} = 0.12 T, (c) B_{z0} = 0.24 T.

Figure 4.13 illustrates the instantaneous distribution of Lorentz force in the central *x*-*y* plane under short circuit at (a) B_{z0} = 0.03 T, (b) B_{z0} = 0.12 T, (c) B_{z0} = 0.24 T. Corresponding to the high current density in the electrodes region, strong Lorentz force (compared with open circuit) are produced.

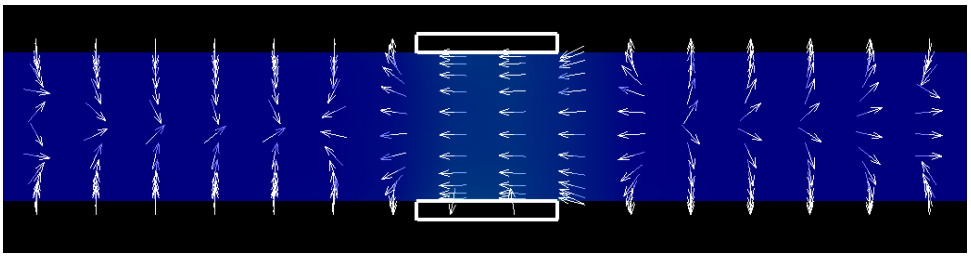

(a) B_{z0} = 0.03 T

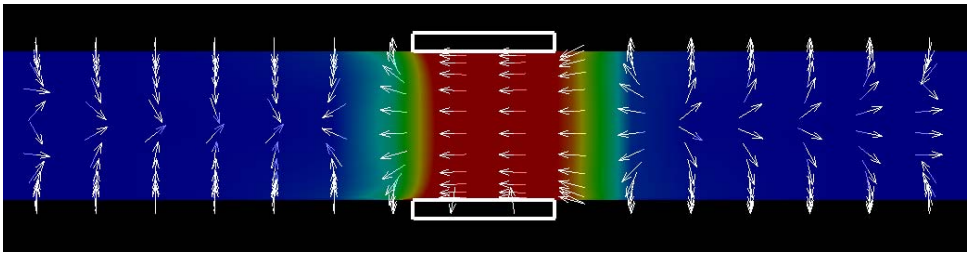

(b) B_{z0} = 0.12 T

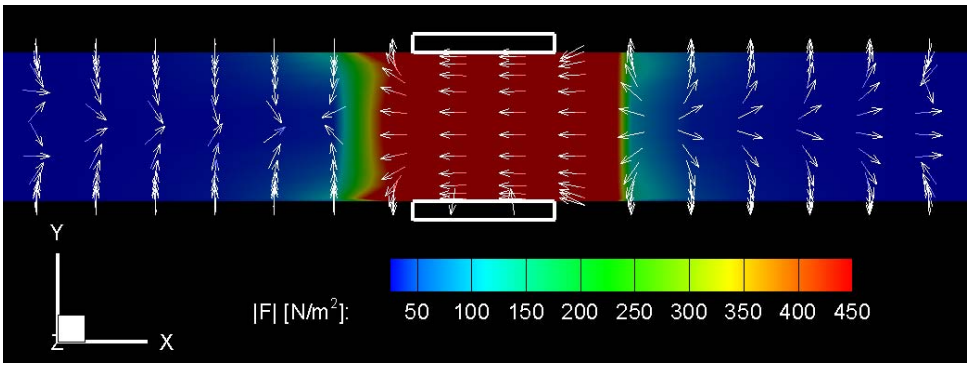

(c) B_{z0} = 0.24 T

Fig. 4.13 Instantaneous distribution of the Lorentz force in the central *x*-*y* plane under short circuit at (a) B_{z0} = 0.03 T, (b) B_{z0} = 0.12 T, (c) B_{z0} = 0.24 T.

Figure 4.14 illustrates the instantaneous distribution of the velocity u_x in the central x-y plane under short circuit at (a) B_{z0} = 0.03 T, (b) B_{z0} = 0.12 T, (c) B_{z0} = 0.24 T. Comparing with open circuit, the feature of short circuit is that the velocity is restrained in the region near the electrodes. It is considered that the short currents near the electrodes produce strong reverse Lorentz force that decelerates the instantaneous velocity, where even reverse (minus) velocity appears in Fig. 4.14(c). Note that in order to show these minus values, Fig. 4.13 illustrates the velocity u_x instead of $|u|$.

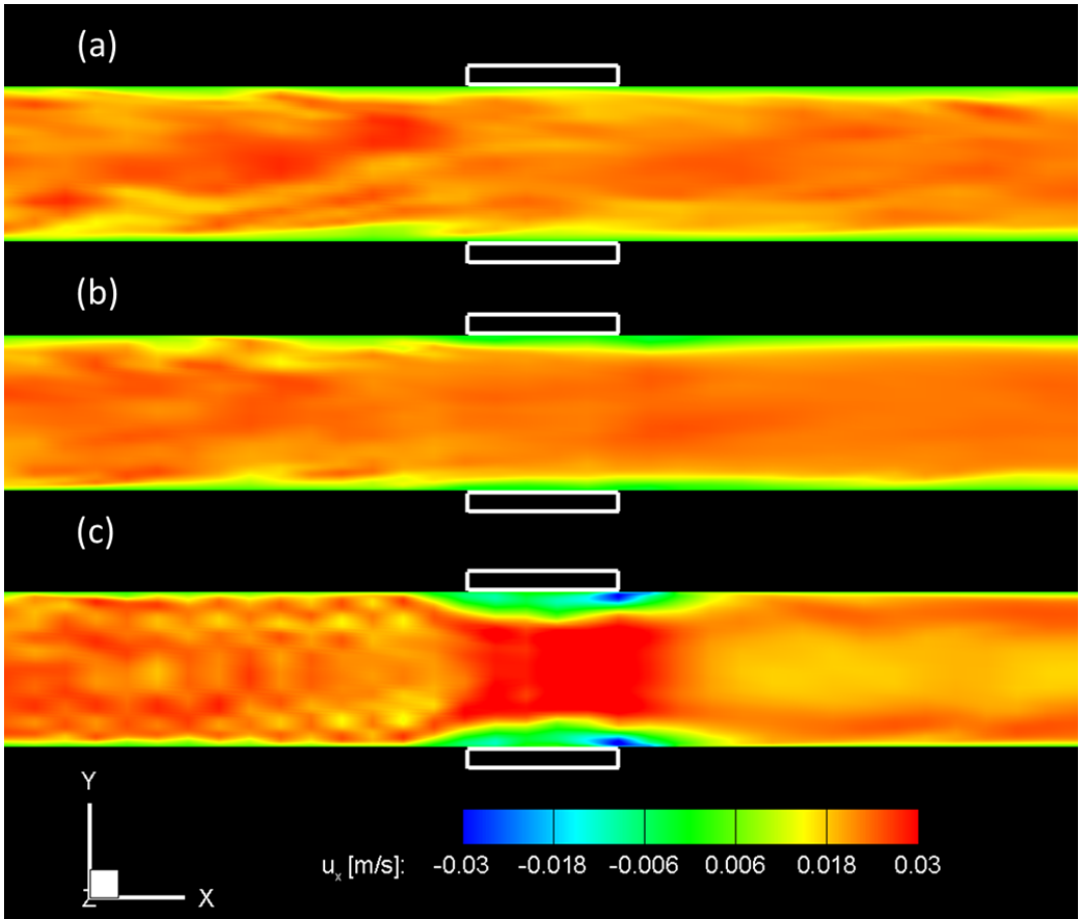

Fig. 4.14 Instantaneous distribution of the velocity u_x in the central x-y plane under short circuit at (a) B_{z0} = 0.03 T, (b) B_{z0} = 0.12 T, (c) B_{z0} = 0.24 T.

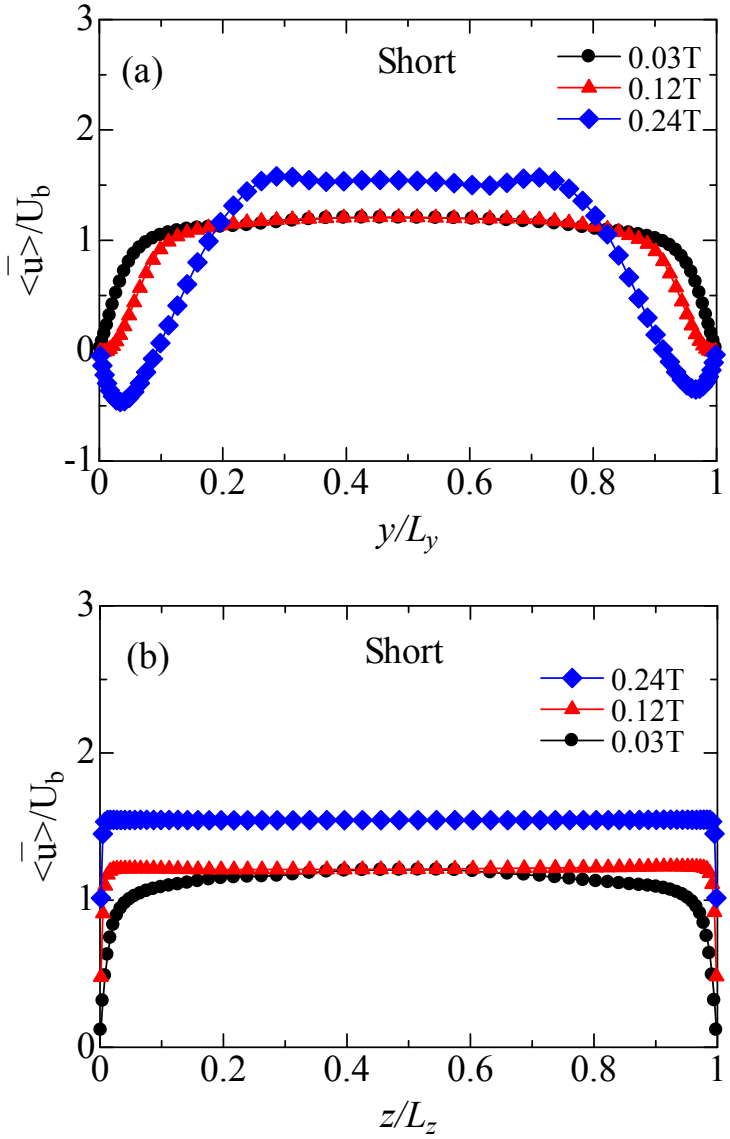

Fig. 4.15 Mean velocity of short circuit at x/L_x = 0 along the (a) horizontal y bisector and (b) vertical z bisector.

Figure 4.15 shows the mean velocity profiles under the short circuit. Comparing to the open circuit, the profile of Bz_0 = 0.12 T is apparently flattened on the horizontal plane. To maintain a same flow rate, the reduction of velocity by enhanced Lorentz force on the horizontal plane (Fig. 4.15(a)) is indirectly reflected by the growth on the vertical plane (Fig. 4.15(b)).

Additionally, the reverse flows on the sidewalls become noticeable with the increase in the magnetic flux density.

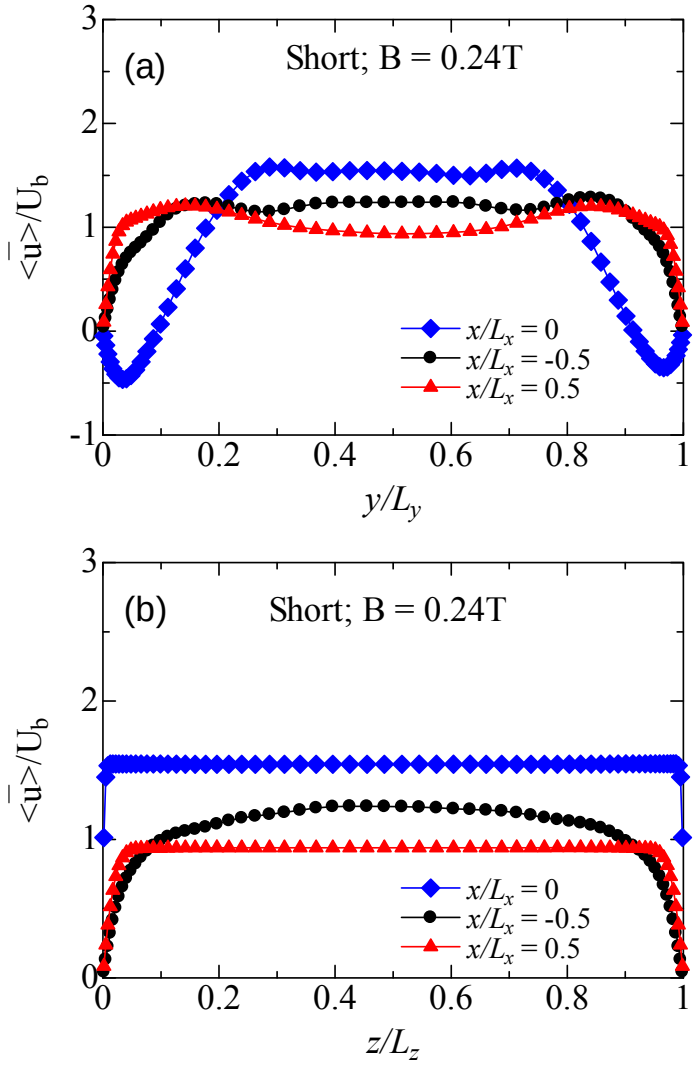

Fig. 4.16 Mean velocity of short circuit at x/L_x = -0.5, 0, 0.5 along the (a) horizontal y bisector and (b) vertical z bisector under Bz_0 = 0.24 T.

Figure 4.16 displays the mean velocity of short circuit at x/L_x = -0.5, 0, 0.5 along the (a) horizontal y bisector and (b) vertical z bisector under magnetic flux density of 0.24 T. From Fig. 4.16(a), the reverse flows only appear in the electrodes region (x/L_x = 0) and immediately

disappear at the downstream region of the duct (x/L_x = 0.5) after the electrodes. It is considered that the much strong Lorentz force caused by the concentration of current near the electrodes promotes the generation of these reverse flows.

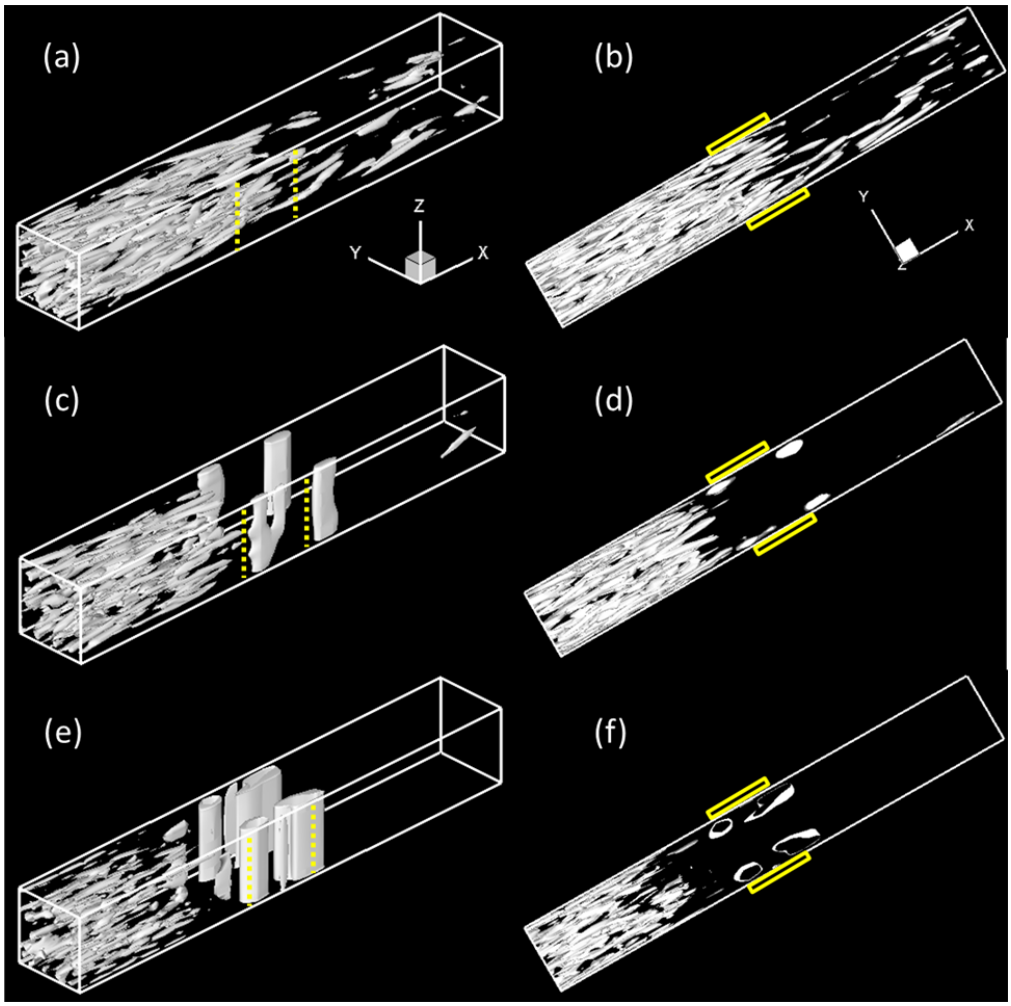

Fig. 4.17 Isosurfaces of the second invariant Q = 0.04 of the velocity gradient tensor under short circuit.

Figure 4.17 shows the transformation of turbulence under short circuit corresponding to Fig. 4.10 with (a, b) Bz_0 = 0.03T, (c, d) Bz_0 = 0.12T, and (e, f) Bz_0 = 0.24T, where (b), (d), (f) are the top view of (a), (c), (e) respectively. From this figure, the turbulent vortices are curbed overall as the magnetic flux density increases. It is considered that the strong Lorentz force

(upward on average) in the middle region limits the fluctuation component of velocity (indicated as $u_1' = u_1 - \langle u_1 \rangle$, where < > denotes the average), which suppresses the Reynolds shear stress ($u_1'u_2'$, $u_1'u_3'$). There are several eddies align along the orientation of the applied magnetic field nearby the electrodes. It is considered that Lorentz force acts like a cylinder with an axis along the z direction [48][71] and the concentration of current near the electrodes changes the directions of Lorentz force (in x-y plane) that can produce these eddies.

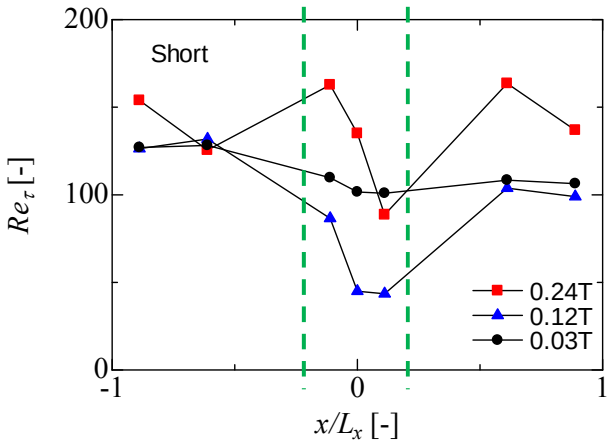

Fig. 4.18 Reynolds number based on the friction velocity at seven locations under short-circuit for three magnetic flux densities.

As similar to Fig. 4.11, Fig. 4.18 shows the friction Reynolds number at the same seven locations for three magnetic flux densities under the short-circuit. The fact that the strong Lorentz force under short circuit curbs the turbulence as shown in Fig. 4.17 is reflected by the small Reynolds numbers (all below 200) overall. Reynolds numbers decrease sharply in the electrodes region, especially for stronger magnetic flux density of 0.24 T. After the electrodes region, since the short currents no longer exist, the Reynolds number recovery for some extent in the downstream. This special distribution of Reynolds numbers complies with the reverse mean

velocity profiles under short circuit. As shown in Figs. 4.15 and 4.16, the reverse flows observed in the electrodes region disappear at the downstream region.

4.3.4 Pump

The results of pump case are discussed in this section. For the purpose of comparability, most of the conditions, such as the flow rate, the magnetic flux densities are kept the same. The unique feature is the change of the load as an ideal external current source that supplies current in the opposite direction to the power generation.

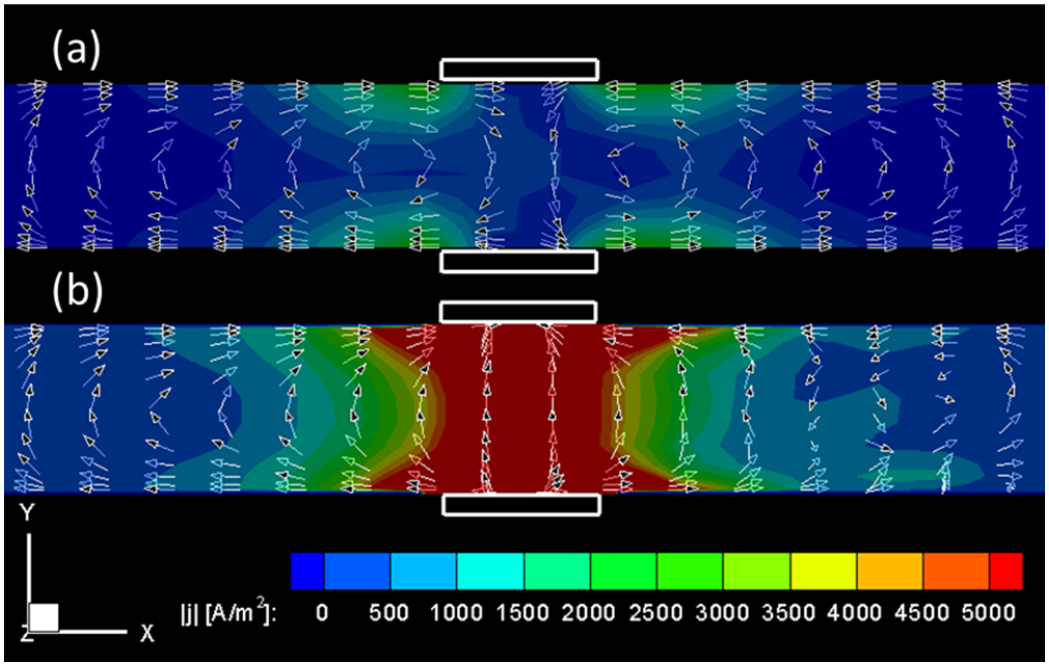

Fig. 4.19 Instantaneous distribution of the electric current density under (a) 3.6 A and (b) 72 A in the central *x*-*y* plane under pump circuit.

First, the mean velocity and the isosurfaces of the second invariant were examined for an external current of I = 3.6 A which is the same value produced under the optimum condition of power generation (at Bz_0 = 0.12 T) [48]. However, the profile is quite similar to those under the open circuit, as shown below. For comparison, therefore, a 20 times larger external current (I =

72 A) was examined. Figures 4.19 (a) and (b) illustrate the distributions of the electric current density in the *x*-*y* plane at Bz_0 = 0.24 T for I = 3.6 A and I = 72 A, respectively.

As mentioned above, Fig. 4.19(a) shows two large eddy currents which looks like the open circuit case (refer to Fig. 4.6). Besides, the arrows show that currents are still flow from the anode (top electrode) to cathode (foot electrode). However, Fig. 4.19(b) shows reverse/positive electric current in the middle area without two large eddy currents.

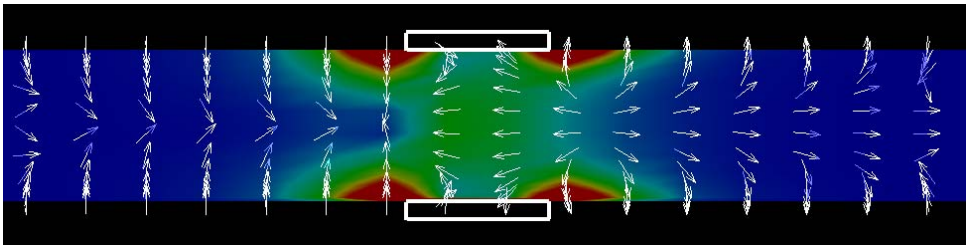

(a) I = 3.6 A

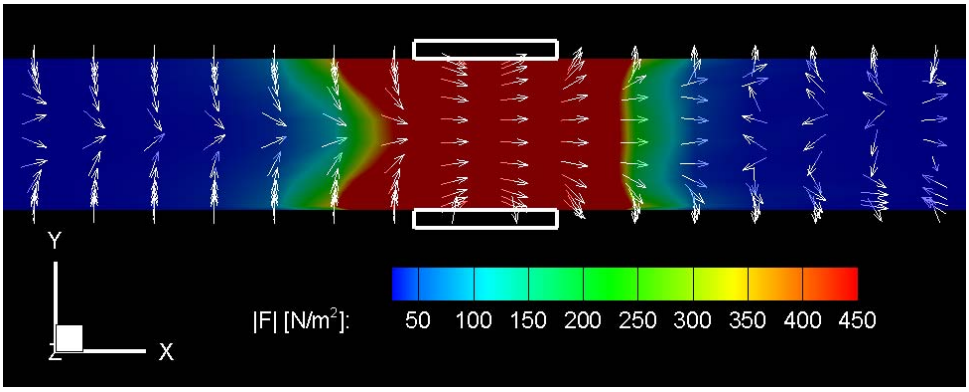

(b) I = 72 A

Fig. 4.20 Instantaneous distribution of the Lorentz force in the central *x*-*y* plane under pump (B_{z0} = 0.24 T) at (a) I = 3.6 A, (b) I = 72 A.

Correspondingly, Fig. 4.20 displays the instantaneous distribution of the Lorentz force. It clearly shows that the directions of the Lorentz force in the electrodes region are different, or

even opposite between (a) I = 3.6 A and (b) I = 72 A, although both of which are under pump case.

To clarify the phenomena, Figs 4.21(a) and (b) show the profiles of the electric current density j_y for I = 3.6 A and I = 72 A at x/L_x = 0, 0.12, 0.5 in the central x-y plane. These places locate at the middle area of the electrodes, downstream edge of the electrodes and downstream region of the duct in stream-wise direction. From Fig. 4.21(a), although positive electric current density can be observed in electrodes area (x/L_x = 0, 0.12) near the sidewalls (y/L_y = 0 ~ 0.1, 0.9 ~ 1), the values change to minus in the middle area (y/L_y = 0.1 ~ 0.9). It means the applied external current is offset by the electromotive force. From Fig. 4.21(b), on the other hand, even though the electromotive force can offset parts of the external current, the strong external electric current (I = 72 A) ensures positive current to flow on the whole.

Figure 4.21 (c) shows the mean velocity profiles at x/L_x = 0 of I = 3.6 A and I = 72 A. It shows the M-shaped profiles appear in the plane perpendicular to the magnetic field for both external current cases. The velocities are flattened correspondingly in the parallel plane, and the increase of external current from 3.6 A to 72 A enhances the flow acceleration near the sidewalls (electrode wall). Thus, as shown in Figs. 4.21 (a) and (b), the large positive electric current density j_y near the sidewalls provides strong downward Lorentz force on the flows, while j_y reduced by the electromotive force weakens (for I = 72 A) or reverses (for I = 3.6 A) the Lorentz force in the middle area (y/L_y = 0.1 ~ 0.9).

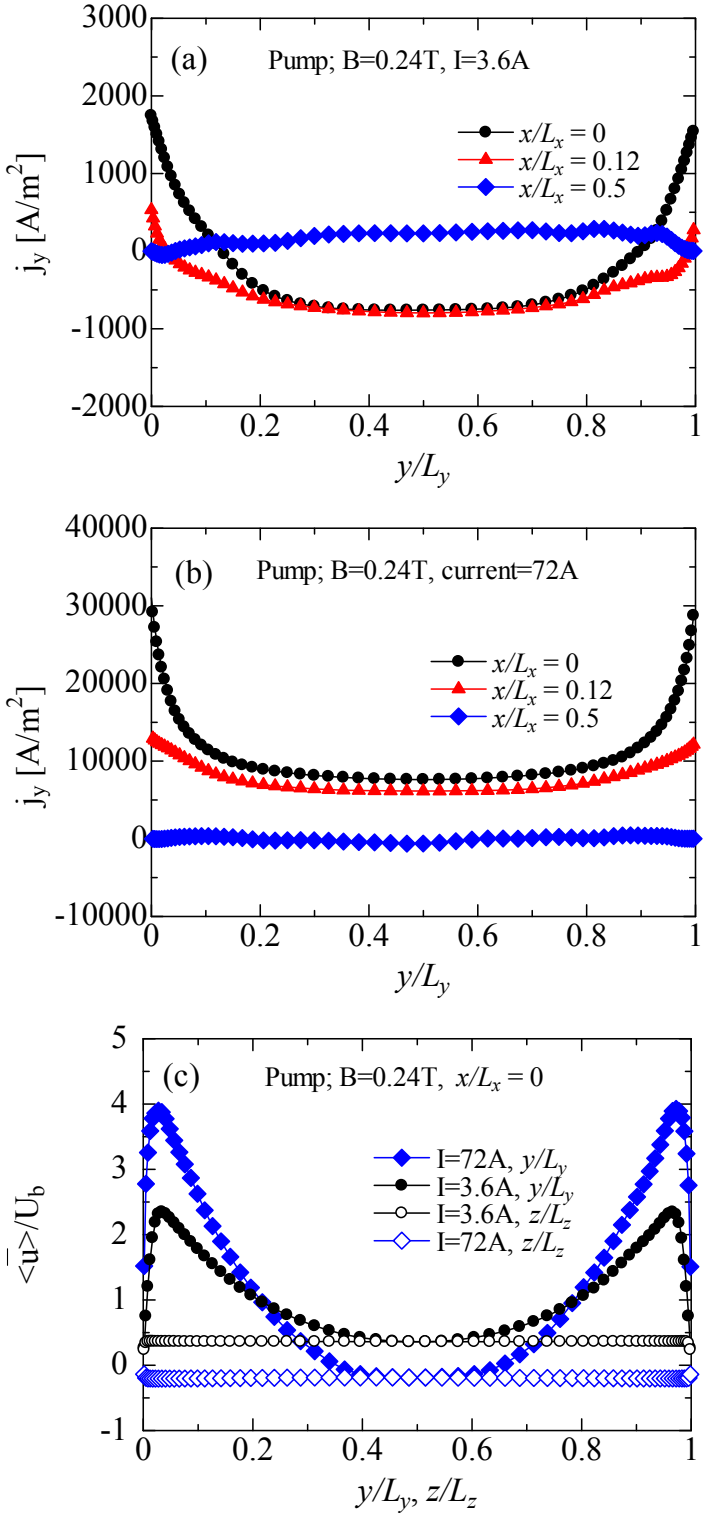

Fig. 4.21 Electric current density of pump circuit at $x/L_x = 0$, 0.12, 0.5 for external current of (a) 3.6 A, (b) 72 A, and (c) mean velocity at $x/L_x = 0$.

Figure 4.22 shows the overall isosurfaces of the second invariant Q = 0.04 of the velocity gradient tensor at external current of (a), (b) I = 3.6 A and (c), (d) I = 72 A under B_{z0} = 0.24 T. As is different from the open or short circuit, the flows are accelerated forward by downward Lorentz force in the electrodes region. In the downstream region of the duct, the strong sidewall jets shown in Fig. 4.21(c) promote the recurrence of turbulence immediately. Figure 4.22(d) shows the abrupt turbulent transition happens in the downstream region, while different from the gradual development shown in Fig. 4.22(b). Thus, eddies are curbed greatly in the electrodes area and then transform to fully turbulence. This fact can be attributed to the Lorentz force enlarged with increasing the external current. The large eddies align along the orientation of the applied magnetic field nearby the electrodes can have some similarity in various conditions. Thus, the cylinder effects originating from the Lorentz force in the center and the concentration of current near the electrodes are considered to promote these eddies.

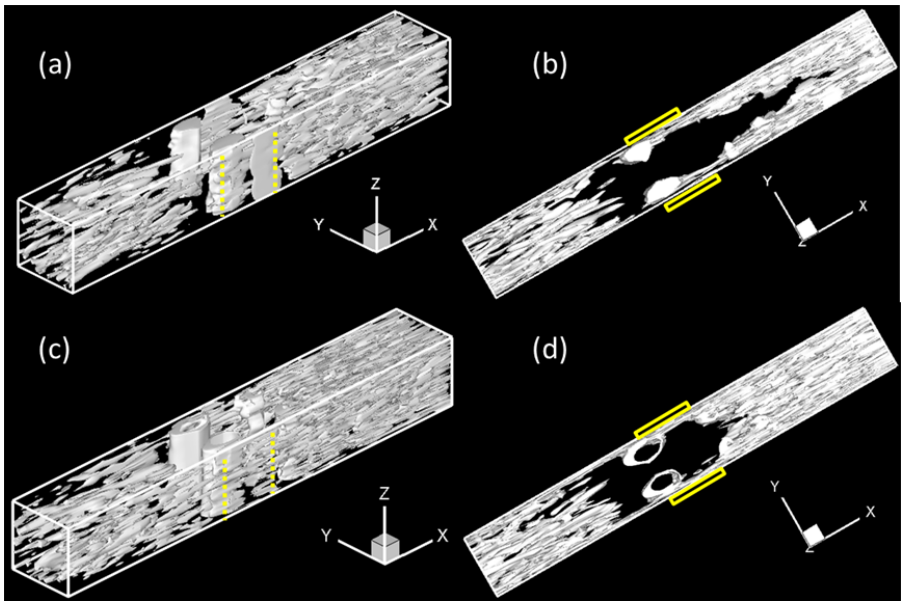

Fig. 4.22 Isosurfaces of the second invariant Q = 0.04 of the velocity gradient tensor under pump circuit.

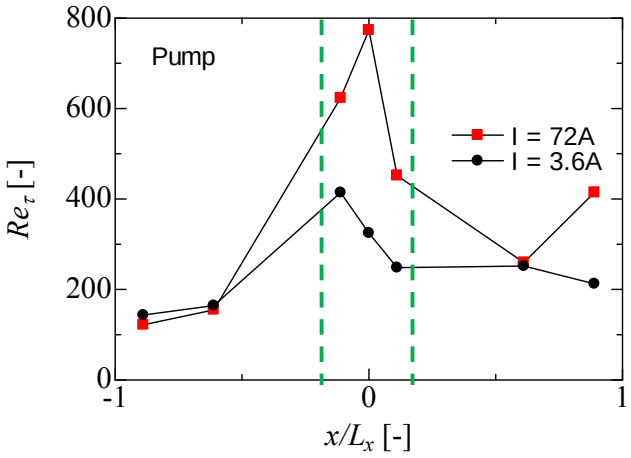

Fig. 4.23 Reynolds number based on the friction velocity at seven locations under pump with magnetic flux density of 0.24 T.

Figure 4.23 represents the Reynolds number based on the friction velocity at seven locations under pump with magnetic flux density of 0.24 T. As mentioned above, the average downward Lorentz force in the electrodes region no longer restrict the turbulence, which increases the Reynolds number as high as 800. Therefore, it is reasonable for the happen of abrupt turbulent transition in the downstream region.

As a supplement of pump case, the simulations at three strengthened magnetic flux densities (B_{z0} = 0.03 T, 0.12 T, 0.24 T) under I = 32 A are carried out. The reason to choose this value count on the demand of enough positive current to ensure the pump condition, while need much less calculation cost than I = 72 A on the other hand. Generally, the phenomena agree with the discussion above. To avoid repeating the same discussion, only the results for instances are listed below.

Figure 4.24 displays the instantaneous distribution of electric current density in the central *x*-*y* plane under pump at (a) B_{z0} = 0.03 T, (b) B_{z0} = 0.12 T, (c) B_{z0} = 0.24 T.

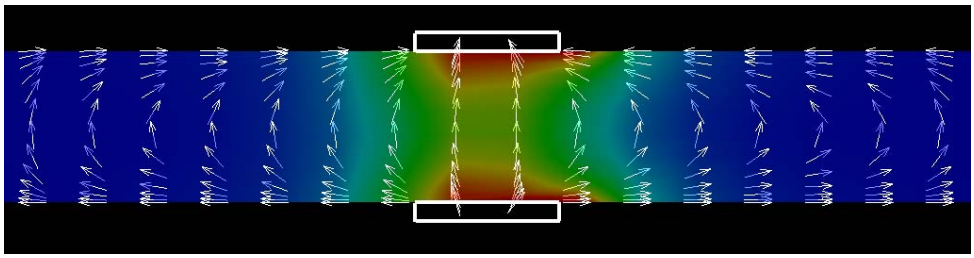

(a) B_{z0} = 0.03 T, I = 32 A.

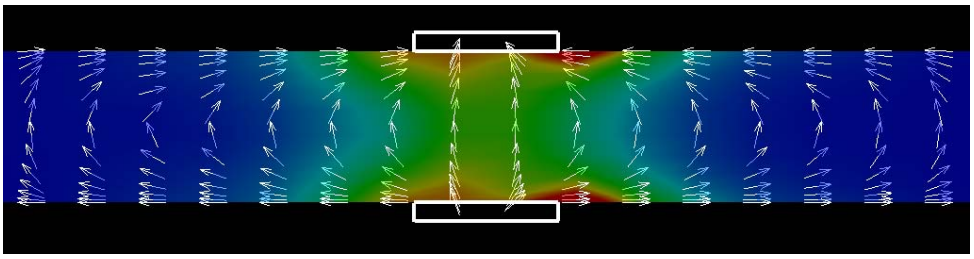

(b) B_{z0} = 0.12 T, I = 32 A.

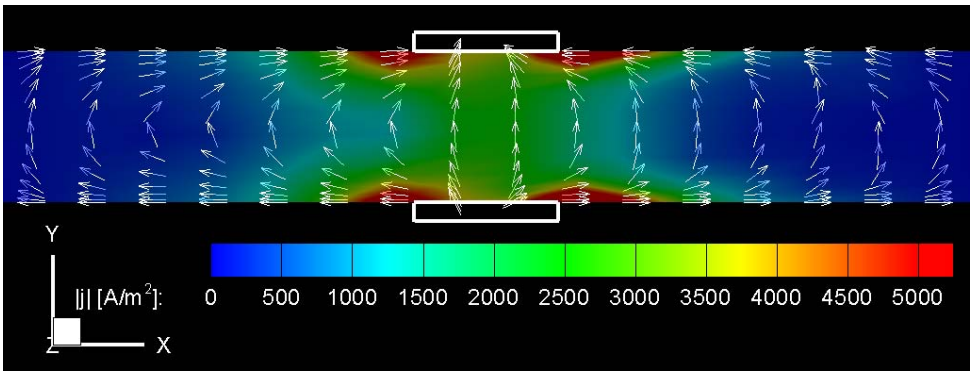

(c) B_{z0} = 0.24 T, I = 32 A.

Fig. 4.24 Instantaneous distribution of electric current density in the central *x*-*y* plane under pump at (a) B_{z0} = 0.03 T, (b) B_{z0} = 0.12 T, (c) B_{z0} = 0.24 T.

Figure 4.25 shows the instantaneous distribution of the Lorentz force in the central *x*-*y* plane under pump at (a) B_{z0} = 0.03 T, (b) B_{z0} = 0.12 T, (c) B_{z0} = 0.24 T.

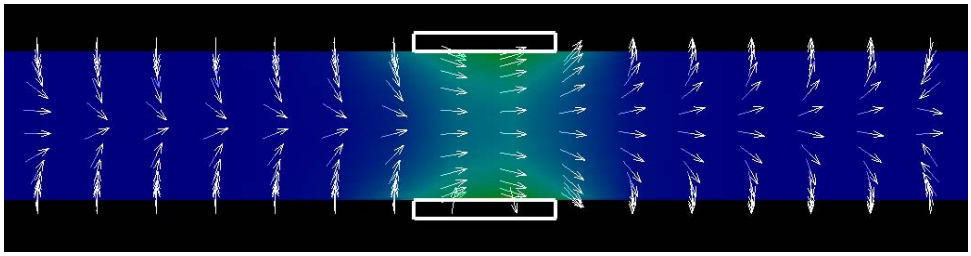

(a) B_{z0} = 0.03 T

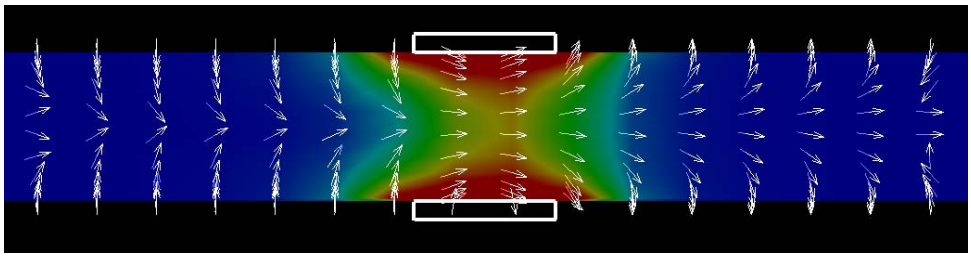

(b) B_{z0} = 0.12 T

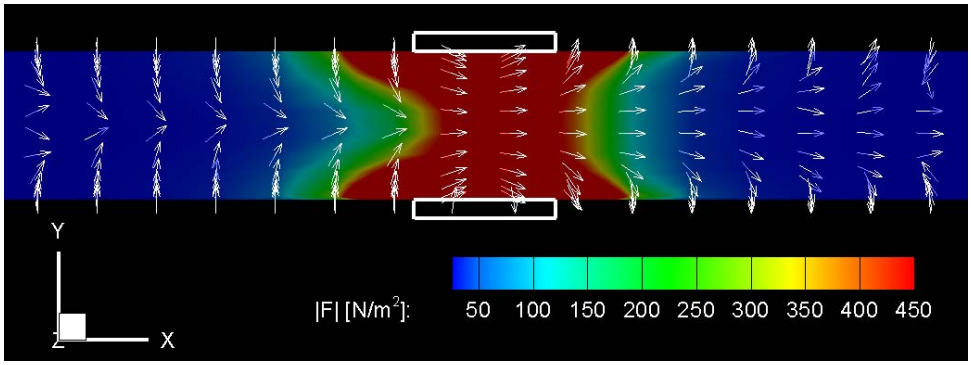

(c) B_{z0} = 0.24 T

Fig. 4.25 Instantaneous distribution of the Lorentz force in the central *x*-*y* plane under pump (I = 32 A) at (a) B_{z0} = 0.03 T, (b) B_{z0} = 0.12 T, (c) B_{z0} = 0.24 T.

Figure 4.26 illustrates the instantaneous distribution of velocity in the central *x*-*y* plane for all the cases of pump discussed above in this thesis.

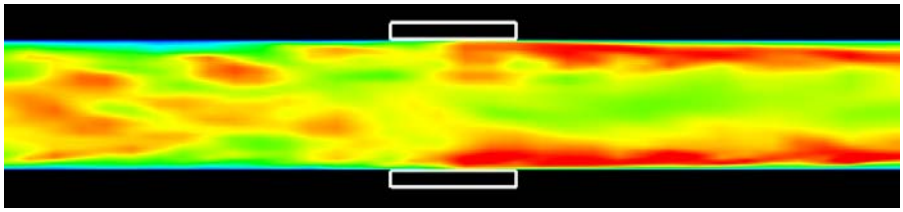

(a) B_{z0} = 0.03 T, I = 32 A.

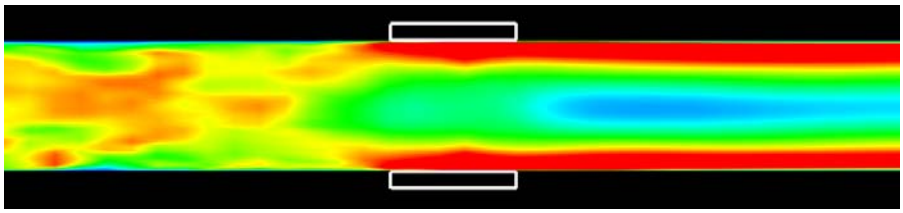

(b) B_{z0} = 0.12 T, I = 32 A.

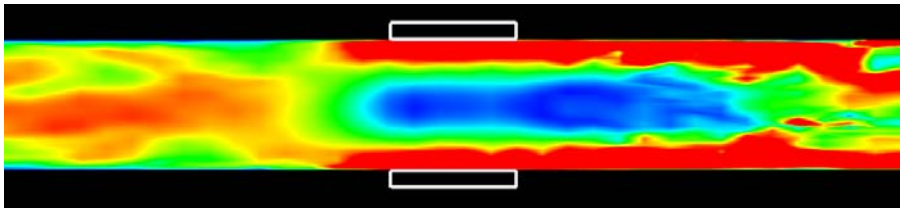

(c) B_{z0} = 0.24 T, I = 32 A.

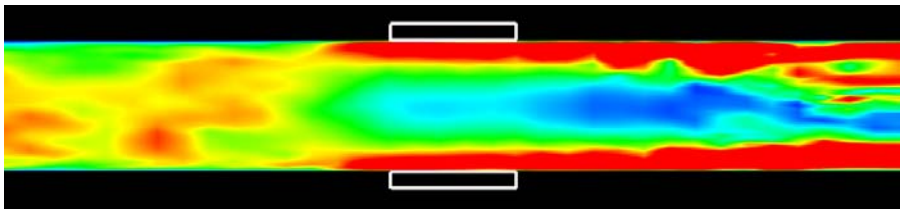

(d) B_{z0} = 0.24 T, I = 3.6 A.

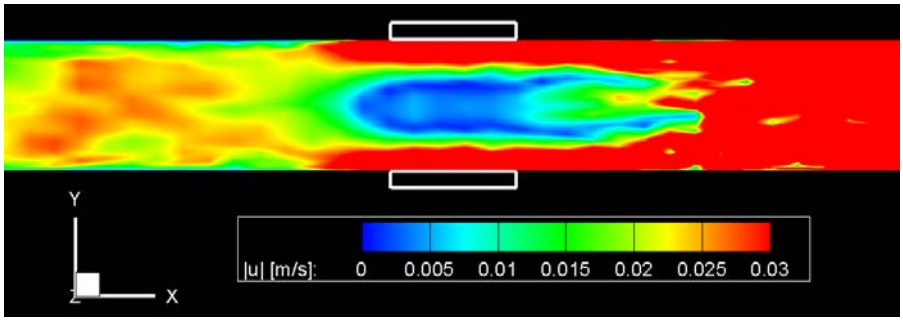

(e) B_{z0} = 0.24 T, I = 72 A.

Fig. 4.26 Instantaneous distribution of velocity in the central *x*-*y* plane under pump.

4.4 Summary

The turbulent phenomena in liquid metal MHD flows under three extreme load conditions (open-circuit, short-circuit, and the pump conditions) have been examined. Non-uniform magnetic flux densities under the maximum strength from B_{z0} = 0.03 T to B_{z0} = 0.24 T are applied successively. The influences of various load conditions and magnetic flux densities on the development of mean velocity profiles and three dimensional turbulence structures are observed. The conclusions are as follows.

(1) Under the open-circuit condition, with increasing the magnetic flux density an M-shaped velocity profile develops in the plane perpendicular to the magnetic field due to the large eddy currents. The eddies represented by the second invariant Q = 0.04 are curbed by the Lorentz force. At B_{z0} = 0.24 T, the sidewall jets promote the recurrence of turbulence in the downstream region.

(2) Under the short-circuit condition, the mean velocity decelerates markedly in the plane perpendicular to the magnetic field. Owing to the concentration of current near the electrodes, the reverse sidewall flows appear gradually as magnetic flux density increase. The strong Lorentz force suppresses the turbulent vortices overall.

(3) Under the pump condition, when the external current is not large enough, the mean velocity profile and the eddies present similar distributions like the open-circuit case. For a large applied current of I = 72 A under B_{z0} = 0.24 T, the strong Lorentz force (downward on average) enhances the M-shape velocity. The eddies are curbed in the electrodes area and turbulence appears abruptly again in the downstream region.

The findings in this chapter are useful for the observation and control of an opaque liquid metal in the MHD applications on a generator or accelerator.

Chapter 5 - **Conclusions**

5.1 Conclusions of this thesis

Numerical study of the performance and turbulent flows in a liquid metal MHD generator, which is expected to generate power with high efficiency through using the wave energy from natural, are conducted in this thesis.

Three major topics have been examined and discussed in details.

A) The responses of a liquid metal MHD power generation system to various external inputs of piston force were mainly examined in the presence of the shape loss.

B) The influence of working fluid characteristics on the MHD generator performance were analyzed to observe the electrical performance under various liquid metals as well as the finite electrical conductive electrodes.

C) The turbulent phenomena in a liquid metal MHD flows with the influence of non-uniform magnetic flux density and various load conditions were compared and discussed.

To summarize it overall, the present study mainly focuses on two important areas that (I) the electrical efficiency performance and (II) the MHD flows phenomena, which are the major concerns of the entire field of LMMHD, judging by the previous studies. In addition, the effects of three main aspects that (a) the externally applied magnetic flux densities, (b) physical properties of working fluids, and (c) the load conditions are examined and clarified successively. Moreover, the influences of (d) shape loss as well as (e) the finite electrical conductivity of electrodes are investigated and revealed individually for some topics.

The results have confirmed the feasibility of the wave energy LMMHD power generation system. The information of optimal electrical efficiency under different load conditions among various liquid metals should be useful for material selection. And the findings about the

transition of turbulence are considered useful for the observation and control of an opaque liquid metal in the MHD applications on a generator or accelerator.

To classify the conclusions separately according to the topics, there are as follows.

5.1.1 Conclusions on Response of a liquid metal MHD power generation system

In the first part of this thesis, the response of a wave energy LMMHD power generation system to various external inputs of piston forces (constant (step), square, sinusoidal, P-M waves) has been discussed. From the results, following remarks were obtained.

1. The electrical efficiency in the presence of the shape loss can be expressed as Eq. (2.18) for a constant force, and is characterized by a parameter S with the coefficient of shape loss λ' as well as ρ, σ and B. Although the electrical efficiency is reduced owing to the shape loss, the deterioration can be mitigated by using NaK with low density and high electrical conductivity and compensated by the increase in the applied magnetic flux density.

2. From the examination about the frequency response, the period of several seconds is suitable from a viewpoint of response of liquid metal and piston (float) motion, which can meet the real ocean wave with the period of the order of seconds and the amplitude of the order of meters.

3. The irregular force input based on the P-M wave gives no big difference with the regular forces when the effective value of the input is the same in effective value, which can provide a prospect for the utilization of a real ocean wave.

These remarks confirm the feasibility of the wave energy LMMHD power generation system and provide some initial examinations for the influence of each parameter on the performance.

5.1.2 Conclusions on Influence of Working Fluid Characteristics on the MHD Generator Performance

To further on, in the second part of this thesis, the influence of working fluid characteristics on the performance of an LMMHD generator has been investigated numerically for fixed flow conditions.

The similarities of both fluid phenomena and electrical performance among various liquid metals have been revealed by using a large eddy simulation, which ensures much more realistic and reliable estimations of performance than those not taking account of turbulent models. The results can be summarized as follow.

The fluid characteristic, that is the mean velocity profile, is determined by the interaction parameter when Re, B and σ_e are fixed. However, the electrical efficiency differs even with the same interaction parameter owing to the finite conductivity of the electrodes. This discrepancy will be eliminated if the ratio of the electrical conductivities of the liquid metal and the electrode is fixed. As a result, in real situations in which electrodes have finite electrical conductivity, working conditions with a large interaction parameter and a liquid metal with a relatively low electrical conductivity for decreasing σ_f/σ_e are expected to provide better performance.

Until now, the influence of the electrical conductivity of electrodes, which may include lead wires, on the electrical performance of an LMMHD generator has never been considered, as far as I know. It has been found in this study that the finite electrical conductivity affects not only the electrical efficiency, but also the choice of working fluid. This is one of the novel aspects of the present work.

The present findings should be useful for material selection and design optimization in the research and development of LMMHD power generators.

5.1.3 Conclusions on Turbulent Phenomena in a Liquid Metal MHD Flows

Finally, the turbulent phenomena in liquid metal MHD flows under three extreme load conditions (open-circuit, short-circuit, and the pump) have been observed in the third part of this thesis. The following conclusions can be drawn.

1. Under the open-circuit condition, with increasing the magnetic flux density an M-shaped velocity profile develops in the plane perpendicular to the magnetic field due to the large eddy currents. The eddies represented by the second invariant $Q = 0.04$ are curbed by the Lorentz force. At $B_{z0} = 0.24$ T, the sidewall jets promote the recurrence of turbulence in the downstream region.

2. Under the short-circuit condition, the mean velocity decelerates markedly in the plane perpendicular to the magnetic field. Owing to the concentration of current near the electrodes, the reverse sidewall flows appear gradually as magnetic flux density increase. The strong Lorentz force suppresses the turbulent vortices overall.

3. Under the pump condition, when the external current is not large enough, the mean velocity profile and the eddies present similar distributions like the open-circuit case. For a large applied current of $I = 72$ A under $B_{z0} = 0.24$ T, the strong Lorentz force (downward on average) enhances the M-shape velocity. The eddies are curbed in the electrodes area and turbulence appears abruptly again in the downstream region.

Generally, external applied magnetic flux density has a laminarization effect on the MHD flows, while the sidewall jets increase the Reynolds stress and Reynolds number that promote the transition of turbulence again. These findings in this work are useful for the observation and control of an opaque liquid metal in the MHD applications on a generator or accelerator.

5.1.4 A short discussion on the conclusions

To consider the conclusions in brief overall, the relations or differences between each chapter are as follows. Comparing to an overall analysis on the wave energy liquid metal MHD power generation system of chapter 2, chapters 3 and 4 examine the electrical performance and turbulence transition with a focus on the liquid metal MHD generator.

Although same liquid metals are compared in both chapters 2 and 3, the influences from the finite conductivity of the electrodes and the non-uniform magnetic flux densities are discussed in detail with a three dimensional simulation in chapter 3 only. The conclusion of using a liquid metal (mercury) with a relatively low electrical conductivity for electrical performance of chapter 3 contradicts the conclusion of chapter 2 that NaK with low density and high electrical conductivity should be selected under shape loss. Even though the examination considering both the shape loss and the influence of finite electrical conductive electrodes is not occurred at present, it is expected that when the applied magnetic flux density is high (for example at B = 2 T that the influences of shape loss can be neglected), mercury is preferred for the least loss owing to the finite electrical conductive electrodes. On the other hand, for a low applied magnetic flux density (for instance the B_{z0} = 0.24 T examined at chapter 3), the shape loss cause significant influence on the electrical efficiency (refer to Fig. 2.7), then NaK is supposed to be selected in this case.

As to the turbulence, since it is immediately suppressed in the power generation region, the influence of turbulence is small enough that almost causes no impact on the power generation performance [43]. In light of this background, the discussion of chapter 2 does not involve the turbulence content. Additionally, chapter 4 mainly discussed three load conditions (open-circuit, short-circuit, and pump) that it is hard to reflect these extreme conditions with the generation performance in chapter 2.

5.2 Issues in the future

Regardless of the regular wave types or irregular P-M wave type, the effective value of external forces is assumed to maintain a certain stable value and the motion of the floater is supposed to heave in one (vertical) direction in this thesis. The real conditions of ocean waves could be much more complex. Besides, the gravity effect of liquid metal, the friction loss between liquid metal and walls, and the end effect of MHD generator are all simplified or ignored at present. Obviously, a more quantitative and adequate treatment is needed for designing and evaluating a practical power generation system. Furthermore, the size of each component, and the configuration in the LMMHD power generation system should be optimized individually in accordance with the real situations in the installation site.

For the study of LMMHD power generator, in the present study, a relative small turbulence flow (friction Reynolds number of 180) was examined. It is a value usually used in numerical calculations of turbulence that needs reasonable cost from the aspects of computation time. In applications, various flow velocities, especially much faster ones are expected be produced to improve the electrical output. Since the performance of MHD power generator and the transition of turbulent MHD flows have been analyzed under different non-uniform magnetic flux densities and various load conditions, it is also interesting to investigate the effects from the flow itself. Thus, the study of the turbulent MHD flows with much larger friction Reynolds numbers is required.

Another crucial aspect is on the numerical simulation itself. Although the algorithms and turbulent models used in this thesis have been verified in previous studies, it is considered important to verify whether the same or similar phenomena happen under the conditions of the present work, by either the DNS approach or to develop a suitable model that is realizable by RANS.

Appendix A - Simulation of Random Sea Waves by the Pierson-Moskowitz Spectrum

This simulation is based on the Pierson-Moskowitz spectrum, which describes the statistical nature of sea waves [63], to produce random sea waves in time zone. The method is basically an inverse Fourier transform numerically [65] ~ [67].

$$\begin{aligned} x(t) &= \int_{-\infty}^{\infty} X(\omega) e^{i\omega t} d\omega \\ &= \int_{-\infty}^{\infty} \left| X(\omega) \right| e^{i(\omega t + \theta(\omega))} d\omega \\ &\quad where \quad 0 \le \theta(\omega) < 2\pi. \end{aligned} \tag{a.1}$$

Since the relation between Fourier components $X(\omega)$ and spectrum $S(\omega)$ is that $S(\omega) = 2\pi XX^*/\mathrm{T}$, then

$$\left| X(\omega) \right| = \sqrt{T \cdot S(\omega) / 2\pi}, \tag{a.2}$$

The $S(\omega)$, or the P-M spectrum here is a quantity already known. To produce $x(t)$ in a finite interval, the wavenumbers are defined as

$$\begin{aligned} 0 = \omega_0 < \omega_1 < \cdots < \omega_N = 2\pi / \Delta t, \\ \Delta\omega_k = \omega_k - \omega_{k-1}, \qquad \overline{\omega_k} = \frac{\omega_k + \omega_{k-1}}{2}. \end{aligned} \tag{a.3}$$

$$x(t) = \sum_{i=1}^{N} x_i(t) = \sum_{k=1}^{N} 2\sqrt{S(\overline{\omega_k})\Delta\omega_k}\, \cos(\overline{\omega_k} t + \theta_k). \tag{a.4}$$

where the phase θ_k is a random value from 0 to 2π.

Or using the frequency f and angle δ_i to express as

$$x(t) = \sum_{i=1}^{N} x_i(t) = \sum_{i=1}^{N} 2\sqrt{S(\overline{f_i})\Delta f}\, \cos(2\pi \overline{f_i} t + \delta_i). \tag{a.5}$$

$$\Delta f = \frac{1}{\Delta t}, \quad \overline{\omega_i} = 2\pi \overline{f_i}, \quad 0 \le \delta_i \le 2\pi, \quad i = 1, 2, \cdots, N. \tag{a.6}$$

Appendix B - Numerical Procedures of Three Dimensional Calculation

The numerical procedures of the three dimensional calculation of this thesis is based on the Simplified Marker and Cell (SMAC) method [73][74].

Definition of essential variables on the staggered grid

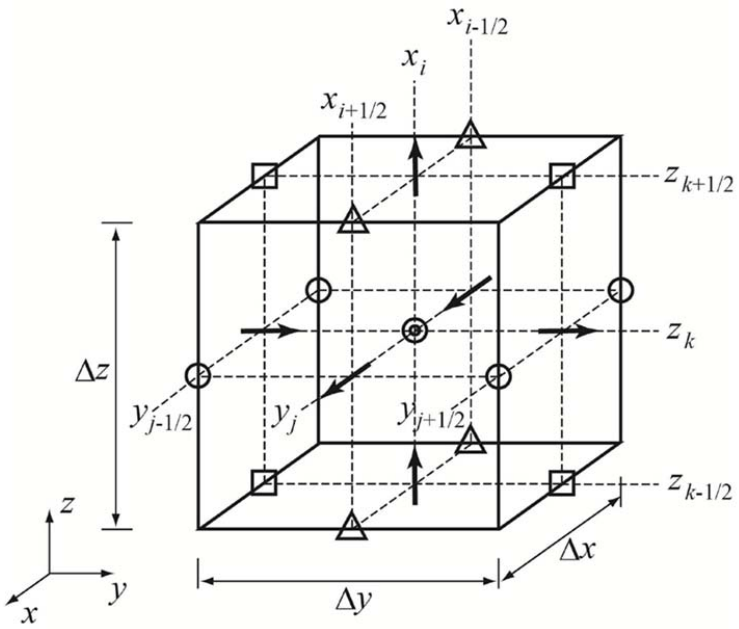

Velocity Electrical current density	u_x, j_x	u_y, j_y	u_z, j_z
Magnetic flux density	B_x	B_y	B_z
Pressure		P	

Fig. b.1 Definition of the velocity, electrical current density, magnetic flux density, and the pressure on the staggered grid.

Staggered grids (mesh) are used for all variables in three dimensional calculations of this thesis. Staggered grid means that instead of placing all variables on one grid, different variables are placed on different grids, which are shifted half a grid point as shown in Fig.b.1.

It illustrates that the variables are placed on a cube. The pressure P is placed in the middle of the cube (volume centered). The momentum vector field $\vec{u}$ (and electrical current density $\vec{j}$) is split up in three components, and each components u_x, u_y and u_z are placed in the middle of the corresponding side (face centered). This means that they are placed on a grid that is shifted half a grid point along the correspond dimension. Other variables like magnetic flux density $\vec{B}$, are placed on the edges (edge centered).

On this staggered grid, the operators use adjacent grid points instead of alternate grid points, which can eliminate the "decoupling problem" happens for placing all variables on an equidistant grid.

Note that here is only a schematic graph, the stretched grid adopted in the y and z directions and equally spaced grid in the x direction changes the appearance of the cube.

Coupling between velocity and pressure

The continuity equation Eq. (3.1) and the incompressible Navier-Stokes equations accompany with the Lorentz force Eq. (3.2) are rewritten as follows.

$$\frac{\partial u_x}{\partial x}+\frac{\partial u_y}{\partial y}+\frac{\partial u_z}{\partial z}=0 \tag{b.1}$$

$$\begin{aligned}\frac{\partial u_x}{\partial t}+\frac{\partial u_x^2}{\partial x}+\frac{\partial u_x u_y}{\partial y}+\frac{\partial u_x u_z}{\partial z} &= -\frac{1}{\rho}\frac{\partial P}{\partial x}+2\frac{\partial}{\partial x}\left(\nu\frac{\partial u_x}{\partial x}\right)\\ &+\frac{\partial}{\partial y}\left(\nu\left(\frac{\partial u_x}{\partial y}+\frac{\partial u_y}{\partial x}\right)\right)+\frac{\partial}{\partial z}\left(\nu\left(\frac{\partial u_x}{\partial z}+\frac{\partial u_z}{\partial x}\right)\right)+\frac{1}{\rho}\left(j_y B_z-j_z B_y\right)+F_x^{\,n},\end{aligned} \tag{b.2}$$

$$\frac{\partial u_y}{\partial t}+\frac{\partial u_y u_x}{\partial x}+\frac{\partial u_y^2}{\partial y}+\frac{\partial u_y u_z}{\partial z} = -\frac{1}{\rho}\frac{\partial P}{\partial y}+2\frac{\partial}{\partial y}\left(\nu\frac{\partial u_y}{\partial y}\right) + \frac{\partial}{\partial x}\left(\nu\left(\frac{\partial u_y}{\partial x}+\frac{\partial u_x}{\partial y}\right)\right)+\frac{\partial}{\partial z}\left(\nu\left(\frac{\partial u_y}{\partial z}+\frac{\partial u_z}{\partial y}\right)\right)+\frac{1}{\rho}\left(j_z B_x - j_x B_z\right)+F_y{}^n \ , \tag{b.3}$$

$$\frac{\partial u_z}{\partial t}+\frac{\partial u_z u_x}{\partial x}+\frac{\partial u_z u_y}{\partial y}+\frac{\partial u_z^2}{\partial z} = -\frac{1}{\rho}\frac{\partial P}{\partial z}+2\frac{\partial}{\partial z}\left(\nu\frac{\partial u_z}{\partial z}\right) + \frac{\partial}{\partial y}\left(\nu\left(\frac{\partial u_z}{\partial y}+\frac{\partial u_y}{\partial z}\right)\right)+\frac{\partial}{\partial x}\left(\nu\left(\frac{\partial u_z}{\partial x}+\frac{\partial u_x}{\partial z}\right)\right)+\frac{1}{\rho}\left(j_x B_y - j_y B_x\right)+F_z{}^n \ . \tag{b.4}$$

In this thesis, since the external magnetic flux density is only applied in the z direction, the B_x and B_y above are zero. Besides, for simplification the first order Euler method is used here to calculate the velocity of next time step as follows.

$$u_x^{n+1} = u_x^n + \Delta t\Big\{ \ -\frac{\partial (u_x{}^n)^2}{\partial x}-\frac{\partial u_x{}^n u_y{}^n}{\partial y}-\frac{\partial u_x{}^n u_z{}^n}{\partial z}-\frac{1}{\rho}\frac{\partial P^{n+1}}{\partial x}+2\frac{\partial}{\partial x}\left(\nu\frac{\partial u_x{}^n}{\partial x}\right) + \frac{\partial}{\partial y}\left(\nu\left(\frac{\partial u_x{}^n}{\partial y}+\frac{\partial u_y{}^n}{\partial x}\right)\right)+\frac{\partial}{\partial z}\left(\nu\left(\frac{\partial u_x{}^n}{\partial z}+\frac{\partial u_z{}^n}{\partial x}\right)\right)+\frac{1}{\rho}\left(j_y{}^n B_z{}^n\right)+F_x{}^n \ \Big\} \ , \tag{b.5}$$

$$u_y^{n+1} = u_y^n + \Delta t\Big\{ \ -\frac{\partial u_y{}^n u_x{}^n}{\partial x}-\frac{\partial (u_y{}^n)^2}{\partial y}-\frac{\partial u_y{}^n u_z{}^n}{\partial z}-\frac{1}{\rho}\frac{\partial P^{n+1}}{\partial y}+2\frac{\partial}{\partial y}\left(\nu\frac{\partial u_y{}^n}{\partial y}\right) + \frac{\partial}{\partial x}\left(\nu\left(\frac{\partial u_y{}^n}{\partial x}+\frac{\partial u_x{}^n}{\partial y}\right)\right)+\frac{\partial}{\partial z}\left(\nu\left(\frac{\partial u_y{}^n}{\partial z}+\frac{\partial u_z{}^n}{\partial y}\right)\right)+\frac{1}{\rho}\left(-j_x{}^n B_z{}^n\right)+F_y{}^n \ \Big\}, \tag{b.6}$$

$$u_z^{n+1} = u_z^n + \Delta t\Big\{ \ -\frac{\partial u_z{}^n u_x{}^n}{\partial x}-\frac{\partial u_z{}^n u_y{}^n}{\partial y}-\frac{\partial (u_z{}^n)^2}{\partial z}-\frac{1}{\rho}\frac{\partial P^{n+1}}{\partial z}+2\frac{\partial}{\partial z}\left(\nu\frac{\partial u_z{}^n}{\partial z}\right) + \frac{\partial}{\partial x}\left(\nu\left(\frac{\partial u_z{}^n}{\partial x}+\frac{\partial u_x{}^n}{\partial z}\right)\right)+\frac{\partial}{\partial y}\left(\nu\left(\frac{\partial u_z{}^n}{\partial y}+\frac{\partial u_y{}^n}{\partial z}\right)\right)+F_z{}^n \ \Big\}. \tag{b.7}$$

The SMAC method assumes pseudo pressures $\overrightarrow{p^*}$ ($\boldsymbol{i}$, t) (such as the latest computed pressures obtained according to the required boundary stress conditions) to calculate the intermediate velocity filed $\overrightarrow{u^*}$ ($\boldsymbol{i}$, t),

$$u_x^* = u_x^n + \Delta t\Big\{ \frac{\partial (u_x{}^n)^2}{\partial x} - \frac{\partial u_x{}^n u_y{}^n}{\partial y} - \frac{\partial u_x{}^n u_z{}^n}{\partial z} - \frac{1}{\rho}\frac{\partial P^*}{\partial x} + 2\frac{\partial}{\partial x}\left(\nu \frac{\partial u_x{}^n}{\partial x}\right) + \frac{\partial}{\partial y}\left(\nu\left(\frac{\partial u_x{}^n}{\partial y} + \frac{\partial u_y{}^n}{\partial x}\right)\right) + \frac{\partial}{\partial z}\left(\nu\left(\frac{\partial u_x{}^n}{\partial z} + \frac{\partial u_z{}^n}{\partial x}\right)\right) + \frac{1}{\rho}\left(j_y{}^n B_z{}^n\right) + F_x{}^n \Big\}, \tag{b.8}$$

$$u_y^* = u_y^n + \Delta t\Big\{ -\frac{\partial u_y{}^n u_x{}^n}{\partial x} - \frac{\partial (u_y{}^n)^2}{\partial y} - \frac{\partial u_y{}^n u_z{}^n}{\partial z} - \frac{1}{\rho}\frac{\partial P^*}{\partial y} + 2\frac{\partial}{\partial y}\left(\nu \frac{\partial u_y{}^n}{\partial y}\right) + \frac{\partial}{\partial x}\left(\nu\left(\frac{\partial u_y{}^n}{\partial x} + \frac{\partial u_x{}^n}{\partial y}\right)\right) + \frac{\partial}{\partial z}\left(\nu\left(\frac{\partial u_y{}^n}{\partial z} + \frac{\partial u_z{}^n}{\partial y}\right)\right) + \frac{1}{\rho}\left(-j_x{}^n B_z{}^n\right) + F_y{}^n \Big\}, \tag{b.9}$$

$$u_z^* = u_z^n + \Delta t\Big\{ -\frac{\partial u_z{}^n u_x{}^n}{\partial x} - \frac{\partial u_z{}^n u_y{}^n}{\partial y} - \frac{\partial (u_z{}^n)^2}{\partial z} - \frac{1}{\rho}\frac{\partial P^*}{\partial z} + 2\frac{\partial}{\partial z}\left(\nu \frac{\partial u_z{}^n}{\partial z}\right) + \frac{\partial}{\partial x}\left(\nu\left(\frac{\partial u_z{}^n}{\partial x} + \frac{\partial u_x{}^n}{\partial z}\right)\right) + \frac{\partial}{\partial y}\left(\nu\left(\frac{\partial u_z{}^n}{\partial y} + \frac{\partial u_y{}^n}{\partial z}\right)\right) + F_z{}^n \Big\}. \tag{b.10}$$

The relation between the pseudo/intermediate values and the exact values is

$$P^{n+1} = P^* + P', \tag{b.11}$$

$$u_i{}^{n+1} = u_i{}^* + u_i{}', \qquad i : x, y, z. \tag{b.12}$$

where A' represents the corrections or compensations of A (P and u_i) and u_i is the ith component (similarly hereafter) of the velocity vector.

Then subtract the (b.8), (b.9), (b.10) from (b.5), (b.6), (b.7), respectively. The following relation is obtained.

$$\frac{u_i{}'}{\Delta t} = -\frac{1}{\rho}\frac{\partial P_i'}{\partial x_i}, \qquad i : 1, 2, 3. \tag{b.13}$$

which equals to

$$\frac{1}{\Delta t}\frac{\partial u_i{}'}{\partial x_i} = -\frac{1}{\rho}\frac{\partial^2 P_i'}{\partial x_i{}^2}, \qquad i : 1, 2, 3. \tag{b.14}$$

Considering the continuity equation, we can assign (b.11) ~ (b.14) to (b.1) in getting

$$\sum \frac{\partial u_i'}{\partial x_i} = -\sum \frac{\partial u_i^*}{\partial x_i}, \tag{b.15}$$

which can calculate the correction *P*' as follow.

$$\sum \frac{\partial^2 P_i^{'}}{\partial x_i^{\,2}} = \frac{\rho}{\Delta t} \sum \frac{\partial u_i^*}{\partial x_i}, \qquad i : 1,2,3. \tag{b.16}$$

Finally, the Poisson equations of P' appears. Accordingly, the true pressure and velocity are obtainable. The last step involves moving the marker particles to the new positions for another loop.

Time-stepping procedure

The velocity is computed by an explicit discretized form of the momentum equations in this thesis. Therefore, the appropriate time-step size for every cycle is verified. It is based on the stability conditions as follows.

$$\Delta t < \frac{1}{2} \frac{\Delta x}{|u_{\max}|}, \tag{b.17}$$

$$\Delta t < \frac{\Delta x^2 \Delta y^2 \Delta z^2}{\Delta x^2 \Delta y^2 + \Delta x^2 \Delta z^2 + \Delta y^2 \Delta z^2} \frac{\mathrm{Re}}{2}. \tag{b.18}$$

where (b.17) requires that no particles should cross more than one cell boundary in a given time interval and (b.18) comes from the explicit discretization of the Navier-Stokes equations [75].

Procedure of Calculating Electric Potential

From the Maxwell's equations, the electric field can be displayed as

$$\vec{E} = -\nabla \phi - \frac{\partial \vec{A}}{\partial t}, \tag{b.19}$$

where the relations between the vector potential and the induced magnetic field are

$$\nabla \times \vec{A} = \vec{B}_i. \tag{b.20}$$

Besides, the Coulomb gauge below is adopted.

$$\nabla \cdot \vec{A} = 0. \tag{b.21}$$

By assigning (b.19) to the Ohm's law Eq. (3.5), the following equation is obtained,

$$\vec{j} = \sigma_f(-\nabla\phi - \frac{\partial\vec{A}}{\partial t} + \vec{u}\times\vec{B}). \tag{b.22}$$

To diverge the both sides simultaneously and use the law of conservation of electric charge,

$$\nabla\cdot\vec{j} = 0, \tag{b.23}$$

the Poisson equation for the electric potential are available as follow.

$$\nabla^2\phi = \nabla\cdot(\vec{u}\times\vec{B}). \tag{b.24}$$

Procedure of calculating induced magnetic field

By rotating the both sides of (b.20), we can get the following equation,

$$\nabla\times\nabla\times\vec{A} = \nabla\times\vec{B}_i. \tag{b.25}$$

The left side of equation (b.25) equals to

$$\nabla\times\nabla\times\vec{A} = -\nabla^2\vec{A} + \nabla(\nabla\cdot\vec{A}), \tag{b.26}$$

where the second term of the right side of equation (b.26) is 0 due to the Coulomb gauge (b.21). Thus,

$$\nabla\times\nabla\times\vec{A} = -\nabla^2\vec{A}. \tag{b.27}$$

On the other hand, from the Ampere's law below,

$$\nabla\times\vec{B}_i = \mu_0\vec{j}, \tag{b.28}$$

(b.25) can be expressed as

$$\nabla^2\vec{A} = -\mu_0\vec{j}. \tag{b.29}$$

Then the Poisson equations for the vector potentials are deduced. Consequently, the induced magnetic field can be calculated.

Flowchart of the numerical procedure

After describing the procedure for each critical part, the overall numerical procedures of the three dimensional calculation is drawn in Fig. b.2.

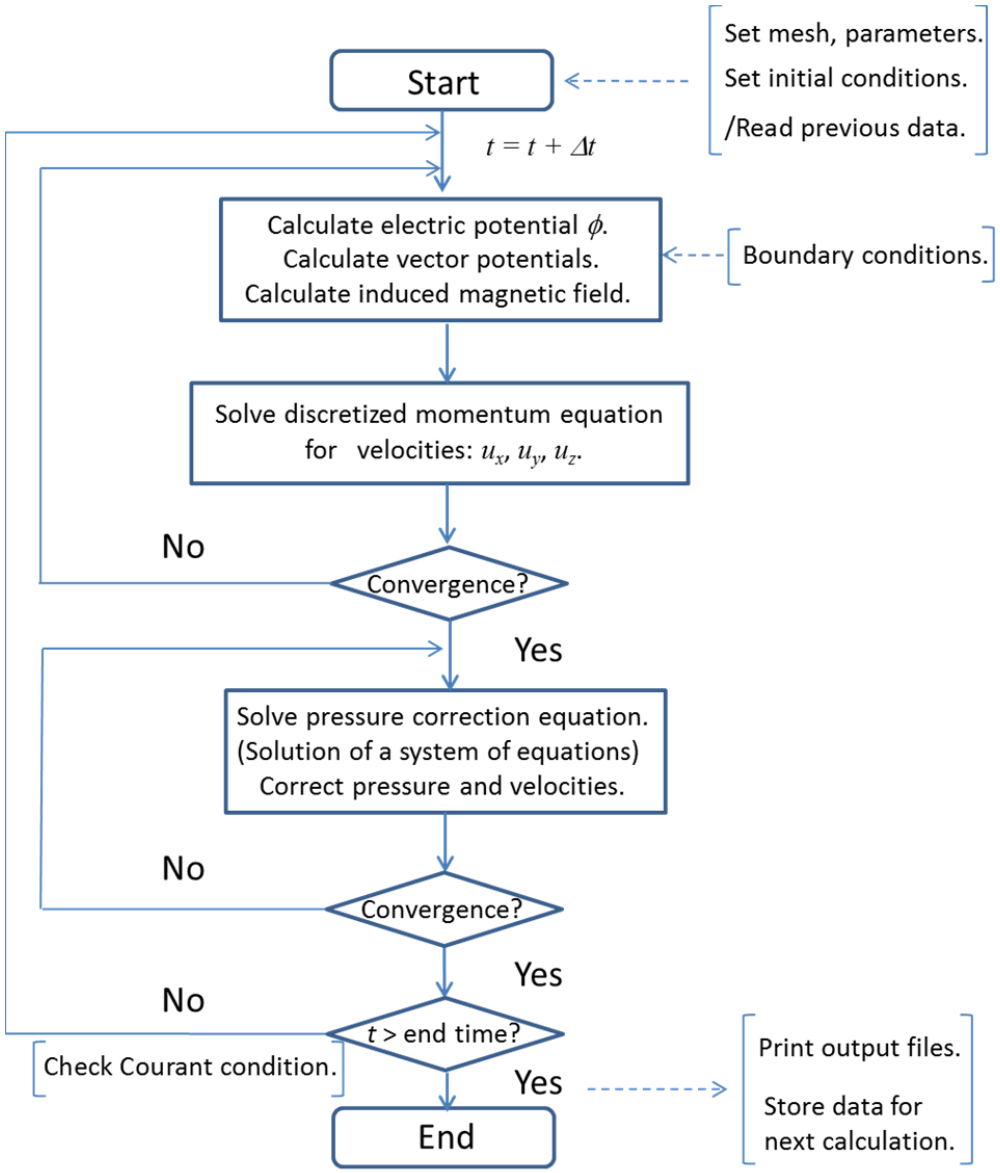

Fig b.2 Flow chart for the numerical procedures of the three dimensional calculation based on the Simplified Marker and Cell (SMAC) method.

Bi-CGSTAB method

The Poisson equations above (the correction of pressure, the electric potential, and the vector potentials) can be solved using methods such as the successive over relaxation (SOR) or the Bi-Conjugate Gradients Stabilized (Bi-CGSTAB) method. This thesis uses the latter one for its fast and smoothly converging feature. For details refer to Reference [76].

Appendix C - Derivation of Equation (3.12)

A volume integral to both sides of the Navier-Stokes equations multiplied by u_i is conducted as follows,

$$\int \left(u_i \cdot (\frac{\partial u_i}{\partial t} + u \cdot \nabla u_i) \right) dV = \int \left(u_i \cdot (\frac{1}{\rho} j \times B - \frac{1}{\rho} \frac{\partial p}{\partial x} + \nu \nabla^2 u_i + F_i) \right) dV. \tag{c.1}$$

When the following relations (c2) ~ (c4) are assigned to (c1),

$$(j \times B) \cdot u = j_y B_z u_x - j_x B_z u_y, \tag{c.2}$$

$$j_x = \sigma(-\nabla_x \varphi + u_y B_z), \tag{c.3}$$

$$j_y = \sigma(-\nabla_y \varphi - u_x B_z). \tag{c.4}$$

(c5) shown below can be obtained in steady state.

$$\begin{aligned} 0 &= \frac{\partial}{\partial t} \int \left(\frac{\rho u^2}{2} \right) dV \\ &= -\int u_x \frac{\partial p}{\partial x} dV + \int \rho u_x F_x dV \\ &\quad + \int (-\frac{j_y^2}{\sigma} - j_y \nabla_y \varphi - \frac{j_x^2}{\sigma} - j_x \nabla_x \varphi) dV + \int \rho u_x \nu \nabla^2 u_x dV. \end{aligned} \tag{c.5}$$

where F_x is the external force to keep a constant mass flow rate.

After normalizing (c5) by the following relations (from (c6) to (c14)) through the characteristic length D and the bulk velocity U_b,

$$u_x^* = \frac{u_x}{U_b}, \tag{c.6}$$

$$x^* = \frac{x}{D}, \tag{c.7}$$

$$y^* = \frac{y}{D}, \tag{c.8}$$

$$p^* = \frac{p}{\rho U_b{}^2}, \tag{c.9}$$

$$F_x^* = \frac{DF_x}{U_b{}^2}, \tag{c.10}$$

$$j_x^* = \frac{j_x}{\sigma U_b B}, \tag{c.11}$$

$$j_y^* = \frac{j_y}{\sigma U_b B}, \tag{c.12}$$

$$\nabla_x^* \varphi^* = \frac{\nabla_x \varphi}{U_b B}, \tag{c.13}$$

$$\nabla_y^* \varphi^* = \frac{\nabla_y \varphi}{U_b B}. \tag{c.14}$$

(c15) (equals to Equation (3.12)) is derived.

$$\begin{aligned} -N(j_y^{*2} + j_y^* \nabla_y^* \varphi^* + j_x^{*2} + j_x^* \nabla_x^* \varphi^*) \\ - u_x^* \frac{\partial P^*}{\partial x^*} + \frac{1}{\mathrm{Re}} u_x^* \nabla^{*2} u_x^* + u_x^* F_x^* = 0. \end{aligned} \tag{c.15}$$

where the Reynolds number Re and the interaction parameter N are defined by

$$\mathrm{Re} = \frac{U_b D}{\nu_m}, \tag{c.16}$$

$$N = \frac{\sigma_f B^2 D}{\rho U} = \frac{\sigma_f}{\mu} \frac{B^2 D^2}{\mathrm{Re}}. \tag{c.17}$$

Appendix D - Derivation of Equation (3.15)

Electrical efficiency defined as the ratio of P_{output} to P_{input} is shown as follow (refer to Eq. (3.12)),

$$\begin{aligned} P_{input} &= -\int u_x^* \frac{\partial p^*}{\partial x^*} dV + \int u_x^* F_x^* dV \\ &= \int N(j_y^{*2} + j_y^* \nabla_y^* \varphi^* + j_x^{*2} + j_x^* \nabla_x^* \varphi^*) dV - \int \frac{1}{\mathrm{Re}} u_x^* \nabla^{*2} u_x^* dV, \end{aligned} \tag{d.1}$$

$$P_{output} = \int N(j_y^* \nabla_y^* \varphi^* + j_x^* \nabla_x^* \varphi^*) dV - \int N j_e^{*2} dV, \tag{d.2}$$

$$\eta = \frac{P_{output}}{P_{input}}, \tag{d.3}$$

where j_e^{*2} is the normalized Joule heating in the electrodes and is assumed as follow,

$$\int N j_e^{*2} dV = \frac{\sigma_f}{\sigma_e} G \int N j_y^{*2} dV. \tag{d.4}$$

By using (d1) ~ (d4) and the following relations: (d5) ~ (d9), (d10) (= Equation (3.15)) is derived.

$$K = \frac{-\nabla_y^* \varphi^*}{u_x^* B^*}, \tag{d.5}$$

$$k_x = \frac{-\nabla_x^* \varphi^*}{u_x^* B^*}, \tag{d.6}$$

$$a = \frac{u_y^*}{u_x^*}, \tag{d.7}$$

$$j_y^* = -(1-K) u_x^* B^*, \tag{d.8}$$

$$j_x^* = (K_x + a) u_x^* B^*, \tag{d.9}$$

$$\eta = \frac{K(1-K) - \dfrac{\sigma_f}{\sigma_e} G(1-K)^2 - k_x(k_x + a)}{K(1-K) + (1-K)^2 + a(k_x + a) - \dfrac{1}{\mathrm{Re}\, N} \dfrac{\int u_x^* \nabla^{*2} u_x^* dV}{\int u_x^{*2} B^{*2} dV}}. \qquad \text{(d.10)}$$

Appendix E - Turbulent Models

Large eddy simulation (LES) resolves large scales (GS: grid scale, or resolvable scale) of the flow field solution allowing better fidelity than alternative approaches such as Reynolds-averaged Navier-Stokes (RANS) methods. Meanwhile, it models small (smaller than the size of low-pass filter, the so called subgrid scale (SGS)) scales of the solution (and also the expensive ones in computation [82]), rather than resolving them as direct numerical simulation (DNS) does. It makes the computational cost for practical engineering systems with complex geometry or flow configurations attainable.

In this section, the Smagorinsky model (one of the most familiar SGS models) and the coherent structure Smagorinsky model (CSM) are briefly introduced. For further details, refer to Refs. [83] ~ [85].

The Smagorinsky model (SM) based on an eddy viscosity is

$$\nu_e = (Cs\Delta)^2 \left(2\overline{S}_{ij}\overline{S}_{ij}\right)^{\frac{1}{2}} = (Cs\Delta)^2 \left\{ \frac{\partial \overline{u}_i}{\partial x_j}\left(\frac{\partial \overline{u}_i}{\partial x_j} + \frac{\partial \overline{u}_j}{\partial x_i} \right) \right\}^{\frac{1}{2}}, \tag{e.1}$$

where Cs is the conventional Smagorinsky constant. S_{ij} is the velocity-strain tensor (defined in (e5)). Δ is the filter width given by

$$\Delta = \sqrt[3]{\Delta x \Delta y \Delta z}. \tag{e.2}$$

The merits of the SM are that the model parameter is locally determined and numerical simulations can be stably carried out (because of the positive model parameter). A couple of demerits consist of (a) the Smagorinsky constant must be changed depending on the flow field. For instance, Cs = 0.2 for homogeneous turbulences while Cs = 0.1 for channel turbulent flows [86]; (b) an explicit wall-damping function is required near walls; (c) the laminarization cannot be reproduced [85].

The model parameter in CSM is extracted by the second invariant Q in a GS flow field, which is given by

$$Q = \frac{1}{2}(\bar{W}_{ij}\bar{W}_{ij} - \bar{S}_{ij}\bar{S}_{ij}) = -\frac{1}{2}\frac{\partial \bar{u}_j}{\partial x_i}\frac{\partial \bar{u}_i}{\partial x_j} \ , \tag{e.3}$$

with

$$\bar{W}_{ij} = -\frac{1}{2}\left(\frac{\partial \bar{u}_j}{\partial x_i} - \frac{\partial \bar{u}_i}{\partial x_j}\right) , \tag{e.4}$$

$$\bar{S}_{ij} = -\frac{1}{2}\left(\frac{\partial \bar{u}_j}{\partial x_i} + \frac{\partial \bar{u}_i}{\partial x_j}\right), \tag{e.5}$$

where $\bar{W}_{ij}$ and $\bar{S}_{ij}$ are the vorticity tensor and the velocity-strain tensor in a GS flow field, respectively. The model parameter C is calculated as follows.

$$C = C_{CSM}\left|F_{CS}\right|^{3/2} F_{\Omega}, \tag{e.6}$$

with

$$C_{CSM} = \frac{1}{22}, \tag{e.7}$$

$$F_{CS} = \frac{Q}{E}, \tag{e.8}$$

$$E = \frac{1}{2}(\bar{W}_{ij}\bar{W}_{ij} + \bar{S}_{ij}\bar{S}_{ij}) = -\frac{1}{2}\left(\frac{\partial \bar{u}_j}{\partial x_i}\right)^2 , \tag{e.9}$$

$$F_{\Omega} = 1 - F_{CS}. \tag{e.10}$$

where *Fcs* is the coherent structure function defined as the second invariant normalized by the magnitude of a velocity gradient tensor E. F_{Ω} is the energy-decay suppression function.

Generally, the model parameter is locally determined, and it is always positive and has a small variance. Besides, wall-damping function is no longer required near walls. Moreover, it has been verified applicable not only to shear turbulences but also to laminar flows [41][42].

Additionally, the validity of using the CSM for MHD flows under uniform and non-uniform magnetic field has been verified [47][48]. R. Chaudhary *et al.* conducted Direct Numerical Simulations (DNS) of magnetic field effects on turbulent flow in a square duct [47]. The effects of a uniform magnetic field on the turbulent flow at a nominal Reynolds number of 5500 were described in detail and compared with Kobayashi's Large Eddy Simulation (LES) results, which had used the Coherent Structure Smagorinsky Model (CSM) [42]. Similar results (For instance, the distribution of mean axial velocities and the velocity fluctuations) were verified and the coincidence approved the validity of the CSM for turbulent flows considering magnetohydrodynamic (MHD) effects. Besides, O. Andreev *et al.* presented an experimental study of a liquid metal flow in a rectangular channel under the influence of a non-uniform magnetic field [34]. The experimentally measured M-shaped form velocity profile had been compared with the M-shaped mean velocity profile observed by Kobayashi *et al.* at the study of turbulent duct flows in a liquid metal MHD power generator using the CSM in LES [48]. A good agreement was obtained and the validity of LES method for the M-shaped MHD flows under a non-uniform magnetic field was considered reasonable.

In chapters 3 and 4 of this thesis, various liquid metals are used and the load conditions change, although there is no direct relative database to refer, major conditions like externally applied magnetic flux densities and Reynolds numbers are kept same to Ref. [48]. The validity of using LES with CSM in this research is considered countable to start from the typical conditions of Re_τ =180.

References

[1] J. T. Houghton. “Climate change 1995: The science of climate change: contribution of working group I to the second assessment report of the Intergovernmental Panel on Climate Change”, **Vol. 2**, *Cambridge University Press*, 1996.

[2] National Research Council. “America’s Climate Choices: Panel on Advancing the Science of Climate Change; Advancing the Science of Climate Change”, Washington, D.C.: *The National Academies Press*, 2010.

[3] F. António. “Wave energy utilization: A review of the technologies”, *Renewable and sustainable energy reviews*, **Vol.14 No.3**, pp. 899-918, 2010.

[4] P. Takahashi and A. Trenka. “Ocean thermal energy conversion: its promise as a total resource system”, *Energy*, **Vol.17 No.7**, pp. 657-668, 1992.

[5] J. Brooke. “Wave energy conversion”, *Elsevier*, 2003.

[6] C. João. “Ocean wave energy”, UK: *Springer Series in Green Energy and Technology*, 2008.

[7] R. David. “Energy from the Waves”, *Elsevier*, 2012.

[8] M. E. McCormick. “Ocean wave energy conversion”, *Courier Dover Publications*, 2013.

[9] D. Mollison. “Wave climate and the wave power resource”, *Hydrodynamic of Ocean Wave-Energy Utilization*, pp. 133-156, Berlin. *Springer*, 1986.

[10] D. MacKay. “Sustainable Energy-without the hot air”, *UIT Cambridge*, 2008.

[11] P. Robin and R. M. Fujita. “Renewable energy from the ocean”, *Marine Policy*, **Vol.26 No.6**, pp. 471-479, 2002.

[12] K. Bønke and N. Ambli. “Prototype wave power stations in Norway”, Proceedings of International Symposium on Utilization of Ocean Waves—*Wave to Energy Conversion*. pp. 34-45, 1986.

[13] H. Ohneda, S. Igarashi, O. Shinbo, S. Sekihara, K. Suzuki, H. Kubota, *et al.* “Construction procedure of a wave power extracting caisson breakwater”, Tokyo: *Proceedings of 3rd Symposium on Ocean Energy Utilization*, pp. 171-179, 1991.

[14] T. Heath, T. Whittaker, and C. Boake. “The design, construction and operation of the LIMPET wave energy converter (Islay, Scotland)”, In: *Proceedings of 4th European Wave Energy Conference*; pp. 49-55, 2000.

[15] J. Kofoed, P. Frigaard, E. Friis-Madsen, and H. Sørensen. “Prototype testing of the wave energy converter Wave Dragon”, *Renewable Energy*, **Vol.31**, pp. 181-189, 2006.

[16] R. Waters, M. Stalberg, O. Danielsson, O. Svensson, S. Gustafsson, E. Stromstedt, *et al.* “Experimental results from sea trials of an offshore wave energy system”, *Applied Physics Letters*, **Vol.90**, No.3, 2007.

[17] Y. Peng, Z. Lin, L. Zhao, C. Sha, R. Li, Y. Xu, B. Liu J. Li, and J. Jia. “Analysis of Liquid Metal MHD Wave Energy Direct Conversion System”, *Proceedings of the Eighteenth International Offshore and Polar Engineering Conference*, pp. 388-392, 2008.

[18] A. Clément, P. McCullen, *et al.* “Wave energy in Europe: current status and perspectives”, *Renewable and sustainable energy reviews*, **Vol.6 No.5**, pp. 405-431, 2002.

[19] S. Hilbert. “Introduction to ocean engineering”, *McGraw-Hill Companies*, pp. 8-9, 1975.

[20] New Energy and Industrial Technology Development Organization. “Renewable energy technology white paper”, *Morikita Publishing*, 2014. (in Japanese)

[21] M. Mueller. “Electrical generators for direct drive wave energy converters”, *IEE Proc Generation Trans Distrib*, **Vol.149**, pp. 446-456, 2002.

[22] K. Rhinefrank, E. Agamloh, A. von Jouanne, A. Wallace, J. Prudell, K. Kimble, *et al.* "Novel ocean energy permanent magnet linear generator buoy", *Renewable Energy*, **Vol.31**, pp. 1279-1298, 2006.
[23] O. Danielsson, K. Thorburn, and M. Leijon. "Direct drive linear generators", *Ocean wave energy*. Berlin: *Springer*; pp. 220-241, 2008.
[24] J. Hartmann. "Hg-dynamics I. Theory of the laminar flow an electrically conductive liquid in a homogeneous magnetic field", *Math. Fys. Medd*. **Vol.15 No.6**, 1937.
[25] J. Hartmann and F. Lazarus. "Hg-dynamics II. Experimental investigations on the flow of Mercury in a homogeneous magnetic field", *Math. Fys. Medd*. **Vol.15 No.7**, 1937.
[26] H. Branover. "Liquid metal MHD", *Proceedings of the Ninth International Conference on Magnetohydrodynamic Power Generation*, **Vol. 5**, pp.1735-1749 1986.
[27] R. J. Rosa. "Magnetohydrodynamic Energy Conversion", *McGraw-Hill*, New York 1968.
[28] G. W. Sutton and A. W. Carlson. "End effects in inviscid flow in a magnetohydrodynamic channel", *Journal of Fluid Mechanics*, **Vol.11 No.1**, pp. 121-132, 1961.
[29] G. W. Sutton, H. Hurwitz, and H. Poritsky. "Electrical and pressure losses in a magnetohydrodynamic channel due to end current loops", *American Institute of Electrical Engineers*, Part I: Transactions of the Communication and Electronics, **Vol.80 No.6**, pp. 687-695, 1962.
[30] D.G.Elliott. "Direct Current Liquid-Metal Magnetohydrodynamic Power Generator", *AIAA Journal*, **Vol.4 No.4**, pp.627-634, 1966.
[31] P.S. Lykoudis and E.C.Brouillette. "Magneto-Fluid-Mechanic Channel Flow. II. Theory", *The Physics of Fluids*, **Vol.10 No.5**, 1967.
[32] E. Brouillette and P. Lykoudis. "Magneto-Fluid-Mechanic Channel Flow. I. Experiment", *The Physics of Fluids*, **Vol.10 No.5**, 1967.
[33] C. Reed and P. S. Lykoudis. "The effect of a transverse magnetic field on shear turbulence", *Journal of Fluid Mechanics*, **Vol.89 No.1**, pp. 147-171, 1978.
[34] O. Andreev, Y. Kolesnikov, and A. Thess. "Experimental study of liquid metal channel flow under the influence of a nonuniform magnetic field", *Phys. Fluids*, **Vol.18**, 2006.
[35] M. Kinet, B. Knaepen, and S. Molokov. "Instabilities and transition in magnetohydrodynamic flows in ducts with electrically conducting walls", *Physical review letters*, **Vol.103 No.15**, 2009.
[36] K. Kitamura and M. Hirata. "Turbulent heat and momentum transfer for electrically conducting fluid flowing in two-dimensional channel under transverse magnetic field", *Sixth International Heat Transfer Conference*. **Vol. 3**, 1978.
[37] O. Widlund, S. Zahrai, and F. H. Bark. "Development of a Reynolds stress closure for modeling of homogeneous MHD turbulence", *Physics of Fluids*, **Vol.10 No.8**, pp.1987-1996, 1998.
[38] S. Smolentsev, M. Abdou, N. Morley, A. Ying, and T. Kunugi. "Application of the 'K-ε' model to open channel flows in a magnetic field", *Int. J. Eng. Sci.*, **Vol.40**, pp. 693-711, 2002.
[39] Y. Shimomura. "Large eddy simulation of magnetohydrodynamic turbulent channel flows under a uniform magnetic field", *Physics of Fluids* A: Fluid Dynamics (1989-1993) **Vol. 3 No.12**, pp. 3098-3106, 1991.
[40] B. Knaepen and P. Moin. "Large-eddy simulation of conductive flows at low magnetic Reynolds number", *Physics of Fluids*, **Vol.16 No.5**, pp. 1255-1261, 2004.
[41] H. Kobayashi. "Large eddy simulation of magnetohydrodynamic turbulent channel flows

with local subgrid-scale model based on coherent structures", *Physics of Fluids*, **Vol.18 No.4**, 2006.
[42] H. Kobayashi. "Large eddy simulation of magnetohydrodynamic turbulent duct flows", *Physics of Fluids*, **Vol.20 No.1**, 2008.
[43] H. Shionoya. "Numerical study on Turbulent Phenomena and Power Generation Characteristics in a Liquid Metal MHD Generator", Master thesis of Tokyo Institute of Technology, pp. 28-29, 2012. (in Japanese)
[44] R. Moser, J. Kim, and N. Mansour. "Direct numerical simulation of turbulent channel flow up to Re_τ =590", Phys. Fluids **Vol.11 No.943**, 1999.
[45] D. Lee and H. Choi. "Magnetohydrodynamic turbulent flow in a channel at low magnetic Reynolds number", *Journal of Fluid Mechanics*, **Vol.439**, pp. 367-394, 2001.
[46] S. Satake, K. Tomoaki, and S. Smolentsev. "Direct numerical simulations of turbulent pipe flow in a transverse magnetic field", *Journal of Turbulence*, **Vol.3 No.20**, pp. 1-12, 2002.
[47] R. Chaudhary, S. P. Vanka, and B. G. Thomas. "Direct numerical simulations of magnetic field effects on turbulent flow in a square duct", Phys. Fluids **Vol. 22**, 2010
[48] H. Kobayashi, H. Shionoya, and Y. Okuno. "Turbulent duct flows in a liquid metal magnetohydrodynamic power generator", *J. Fluid Mechanics*, **Vol.713**, pp.243-270, 2012.
[49] T. Maeda, K. Shimizu, Y. Hasegawa, K. Kakizaki, H. Yamasaki, and Y. Okuno. "The fundamental characteristics of liquid metal MHD engine generator", *Journal of the Japan Society of Applied Electromagnetics*, **Vol.11 No.4**, pp. 249-255, 2003. (In Japanese)
[50] C. Haaland and W.D. Deeds. "Shingle Channel Double-duct Liquid Metal Electrical Generator Using a Magnetohydrodynamic Device", *United States Patent*, Patent No.5923104, 1999.
[51] S. Satake, T. Fujino, M. Ishikawa, and T. Maeda. "Experimental study of proof of principle of liquid metal MHD generation", *In Proceedings of New Energy Technology Symposium*, B-1-4, 2008. (In Japanese)
[52] K. Yamada, T. Maeda, Y. Hasegawa, and Y. Okuno. "Two-dimensional numerical simulation on performance of liquid metal MHD generator", *T. IEE Japan B* **Vol.124**, pp. 971-976. 2004. (In Japanese)
[53] K. Yamada, T. Maeda, Y. Hasegawa, and Y. Okuno. "Three-dimensional numerical simulation on performance of liquid metal MHD generator", *T. IEE Japan B* **Vol.125**, pp. 141-146. 2005. (In Japanese)
[54] L. Zhao, Y. Peng, C. Sha, R. Li, Y. Xu, B. Liu, and J. Li. "Effect of Liquid Metal Characteristics on Performance of LMMHD Wave Energy Conversion System", *Proceedings of the Nineteenth International Offshore and Polar Engineering Conference*, **Vol.1**, pp.308-311, 2009.
[55] L. Zhao, Y. Peng, and C. Sha. "End effect of liquid metal magnetohydrodynamic generator in wave energy direct conversion system", *Sustainable Power Generation and Supply*, 2009.
[56] J. Li, Y. Peng, B. Liu, C. Sha, L. Zhao, Y. Xu, R. Li, and X. Li. "Preliminary experimental study on LMMHD wave energy conversion system", *Proceedings of Twentieth International Offshore and Polar Engineering Conference*, pp. 907-910, 2010.
[57] B. Liu, Y. Peng, L. Zhao, J. Li, R. Li, Y. Xu, and C. Sha. "Hydrodynamic Modelling of Heaving Buoy Wave Energy Conversion System with Liquid Metal Magnetohydrodynamic Generator", *Proceedings of the Twenty-first International Offshore and Polar Engineering Conference*, **Vol.1**, pp. 695-700, 2011.

[58] M. Petrick, G. Fabris, E. Fischer, and C. Johnson. “Experimental two-phase liquid-metal magnetohydrodynamic generator program”, *ARGONNE NATIONAL LAB IL ENGINEERING DIV*, 1979.
[59] G. Fabris, E. Kwack, K. Harstad, and L. Back. “Two-phase flow bubbly mixing for liquid metal magnetohydrodynamic energy conversion”, *Proceedings of the 25th Intersociety Energy Conversion Engineering Conference*, **Vol. 2**, pp. 486-493, 1990.
[60] P. Satyamurthy, N. Dixit, T. Thiyagarajan, N. Venkatramani, A. Quraishi, and A. Mushtaq. “Two-fluid model studies for high density two-phase liquid metal vertical flows”, *International journal of multiphase flow*, **Vol. 24 No.5**, pp. 721-737, 1998.
[61] P. A. Davidson. “An Introduction to Magnetohydrodynamics”, *Cambridge University Press*, 2001.
[62] Japan Society of Civil Engineers. “Hydraulic formula collection”, *Water management committee* 2000. (in Japanese)
[63] W. Pierson and L. Moscowitz. “A proposed spectral form for fully developed wind seas based on the similarity theory of SA Kitaigorodskii”, *Journal of Geophysical Research*, **Vol.69 No.24**, pp. 5181-5190, 1964.
[64] R. H. Stewart. “Introduction to physical oceanography”, *Texas A & M University*, 2004.
[65] M. L. Higgins. “The statistical analysis of a random, moving surface”, Philosophical Transactions of the Royal Society of London, *Mathematical and Physical Sciences*, **Vol.966 No.249**, pp. 321-387, 1957.
[66] M. Hino. “Spectral Analysis”, *Asakura press*, pp. 142-143, 2004. (in Japanese)
[67] Y. Goda. “Random Seas and Design of Maritime Structures”, *World Scientific*, pp. 249-252, 2010.
[68] S. Verardi, J. Cardoso, and M. Costa. “Three-dimensional finite element analysis of MHD duct flow by the penalty function formulation”, *IEEE Transactions on Magnetics*, **Vol.37 No.5**, pp.3384-3387, 2001.
[69] P. Bhuyan and K. Goswami. “Effect of magnetic field on MHD pressure drop inside a rectangular conducting duct”, *IEEE Transactions on Plasma Science*, **Vol.36 No.4,** pp.1955-1959, 2008.
[70] E. Votyakov, Y. Kolesnikov, O. Andreev, E. Zienicke, and A. Thess. “Structure of the wake of a magnetic obstacle”, *Physical review letters*, **Vol.98 No.14**, 2007.
[71] E. Votyakov, E. Zienicke, and Y. Kolesnikov. “Constrained flow around a magnetic obstacle”, *Journal of Fluid Mechanics*, **Vol.610 No.1**, pp.131-156, 2008.
[72] R. Moreau. “Magnetohydrodynamics”, *Springer*, 1991.
[73] F. Harlow and J. Welch. “Numerical calculation of time-dependent viscous incompressible flow of fluid with a free surface”, *Phys Fluids*, pp. 2182-2189, 1965.
[74] A. Amsden and F. Harlow. “The SMAC method: a numerical technique for calculating incompressible fluid flows”, Technical Report LA-4370, *Los Alamos National Laboratory*, 1970.
[75] S. McKee, M. Tome, V. Ferreira, J. Cuminato, and N. Mangiavacchi. “Review the MAC method”, Computers & Fluids, **Vol. 37**, pp. 907-930, 2008.
[76] H. A. Van der Vorst. “Bi-CGSTAB: A fast and smoothly converging variant of Bi-CG for the solution of nonsymmetric linear systems”, *SIAM Journal on scientific and Statistical Computing*, **Vol.3 No.2**, pp. 631-644, 1992.
[77] H. Tennekes and J. L. Lumley. “A first course in turbulence”, *The MIT Press*, 2001.

[78] K. Fujiwara, T. Nakata, and H. Ohashi. “Improvement of convergence characteristic of ICCG method for the A-ϕ method using edge elements”, *IEEE Transactions on Magnetics*, **Vol.32 No.3**, pp. 804-807, 1996.
[79] T. Iwashita, T. Mifune, S. Moriguchi, and M. Shimasaki. “Physical Meaning of the Advantage of A-phi Method in Convergence”, *IEEE Transactions on Magnetics*, **Vol.45 No.3**, pp. 1424-1427, 2009.
[80] S. Satake, T. Kunugi, K. Takase, and Y. Ose. “Direct numerical simulation of turbulent channel flow under a uniform magnetic field for large-scale structures at high Reynolds number”, *Physics of Fluids*, **Vol.18 No.12**, 2006.
[81] T. Boeck, D. Krasnov, and E. Zienicke. “Numerical study of turbulent magnetohydrodynamic channel flow”, *Journal of Fluid Mechanics*, **Vol.572**, pp. 179-188, 2007.
[82] S. B. Pope. “Turbulent Flows”, *Cambridge University Press*, 2000.
[83] J. Smagorinsky. “General circulation experiments with the primitive equations. I. The basic experiment”, *Monthly Weather Review*, **Vol.91 No.3**, pp. 99-164, 1963.
[84] J. W. Deardorff. “A numerical study of three-dimensional turbulent channel flow at large Reynolds numbers. Journal of Fluid Mechanics”, **Vol.41 No.2**, pp. 453-480, 1970.
[85] H. Kobayashi. “The subgrid-scale models based on coherent structures for rotating homogeneous turbulence and turbulent channel flow”, *Physics of Fluids*, **Vol.17 No.4**, 2005.
[86] T. Kajishima. “Numerical Simulation of Turbulent Flows”, *Yokendo Press*, 2014. (in Japanese)

Acknowledgements

I would like to express my gratitude to the following people, without whose help this work would never attained its current state.

First, I would like to thank Prof. Yoshihiro Okuno, for providing me with the opportunity to research at his laboratory. Prof. Okuno is surely a helpful and diligent thesis advisor, especially at difficult times. I have learned the rigorous attitude toward research activities and the diligence to be an early bird even in the weekend from him.

Second, I am also deeply grateful to Prof. Hiromichi Kobayashi of Keio University, for teaching me the computational techniques on supercomputer and knowledge of Hydromechanics from zero. His considerable insights on turbulence have supported my entire doctoral courses. I believe he is the most patient and tolerant teacher I have ever met.

Then, I would like to thank Prof. Tetsuji Okamura, Prof. Tetsuya Suekane, and Assistant Prof. Tomoyuki Murakami for their fruitful advice on my research in MHD group meetings. I also want to thank Prof. Feng Xiao and Prof. Takao Nagasaki for their precious questions on my work during my interim presentation in Sep. 2013.

Still, I am grateful to the members in MHD group of Tokyo Institute of Technology, especially to my precious colleagues Mr. Hiroki Shionoya, for the energetic discussion on my researches. And I give my appreciation to Dr. Kumiko Ogaki and Engineering Official Mr. Hiroshi Takahashi, for their helpful activities in our group.

Finally, I would like to express endless appreciation to my family for their considerate support, not only during the period of doctoral courses, but also the whole life.